Spring 2007

The Observation, Modeling, and Retrieval of Bio-Optical Properties for Coastal Waters of the Southern Chesapeake Bay

Xiaoju Pan
Old Dominion University

THE OBSERVATION, MODELING, AND RETRIEVAL OF BIO-OPTICAL PROPERTIES FOR COASTAL WATERS OF THE SOUTHERN CHESAPEAKE BAY

by

Xiaoju Pan
B.S. July 1996, Xiamen University, China
M.S. July 2000, Institute of Oceanography, the Chinese Academy of Sciences

A Dissertation Submitted to the Faculty of
Old Dominion University in Partial Fulfillment of the
Requirement for the Degree of

DOCTOR OF PHILOSOPHY

OCEANOGRAPHY

OLD DOMINION UNIVERSITY
May 2007

Approved by:

Richard C. Zimmerman (Director)

Larry P. Atkinson (Member)

Margaret R. Mulholland (Member)

Zhonghai Jin (Member)

Mark Havey (Member)

ABSTRACT

THE OBSERVATION, MODELING, AND RETRIEVAL OF BIO-OPTICAL PROPERTIES FOR COASTAL WATERS OF THE SOUTHERN CHESAPEAKE BAY

Xiaoju Pan
Old Dominion University, 2007
Director: Dr. Richard C. Zimmerman

The primary purpose of this study was to develop an inverse method to retrieve the inherent optical properties (IOPs) and biogeochemical parameters (e.g. chlorophyll *a* concentration and salinity) appropriate to monitor the water quality and biogeochemical processes from remote sensing of the coastal waters in the southern Chesapeake Bay and coastal Mid-Atlantic Bight region (MAB) dominated by Case 2 waters. For this purpose, knowledge of the relationship between remote sensing reflectance (R_{rs}) and IOPs and the effect from bottom reflectance on R_{rs}, is required.

A substantial investigation of IOPs has been conducted for the coastal waters of the southern Chesapeake Bay. Although phytoplankton are the dominant contributors to IOPs of oceanic Case 1 waters, colored dissolved organic matter (CDOM) derived from non-phytoplankton sources and sedimentary particles also play very important roles in coastal Case 2 waters. Strongly influenced by riverine discharge, the shallow coastal waters of the southern Chesapeake Bay provide challenges and opportunities to develop regionally specific IOP retrieval methods from remotely sensed ocean color imagery.

A semi-analytical radiative transfer model (PZ06_E_d), based on the analysis of the simulated results of an exact radiative transfer model, *Hydrolight*® [*Mobley*, 1994], was developed to estimate the vertical distribution of downwelling plane irradiance [$E_d(z)$]

from IOPs and sky conditions (e.g. cloud coverage and solar zenith angle). Compared to the significant overestimation of the simple *Gordon* [1989] model for particle-rich environments, PZ06_E_d agreed with *Hydrolight*® with < 6% of the root-mean-square (RMS) error. Field observations from the coastal waters of the southern Chesapeake Bay validated the predictions of PZ06_E_d with RMS error from 10% to 14%. The SeaWiFS imagery of the diffuse attenuation coefficient (K_d) estimated from PZ06_E_d is significantly improved from the *Mueller* [2000] model and displays obviously the coastal processes in the lower MAB, including the riverine outflow from the Chesapeake Bay and the mixing of the Gulf Stream with the local waters.

The quadratic model (e.g. GSM01) describing R_{rs} and IOPs has been widely used in bio-optics to retrieve inherent optical properties (IOPs). In this study, the derived coefficients (l_1 and l_2) by *Gordon et al.* [1988] were re-evaluated from *Hydrolight*® simulations and incorporated into a semi-analytical radiative transfer model (PZ06_R_{rs}) that included bottom effects for optically shallow waters. Compared with *Hydrolight*® simulations and field observations in the Chesapeake Light Tower (CLT), R_{rs} calculated from PZ06_R_{rs} typically agreed within 5% and about 7% to 13% of RMS, respectively. *Hydrolight*® simulations and field observations also confirmed that PZ06_R_{rs} improved the retrieval of biogeochemical-related parameters, including [Chl], $a_{dg}(443)$, and $b_{bp}(443)$, compared to global ocean color algorithms (e.g. OC3M) and semi-analytic models without considering the bottom effects (e.g. GSM01-CLT).

Finally, the relatively successful inverse modeling provides a promising method to study ecosystem-level biogeochemical and physical parameters from remote sensing for coastal waters of southern Chesapeake Bay and even lower MAB.

Thanks to my wife and my parents, for their endless love and support.

ACKNOWLEDGMENTS

First of all, I would like to thank Dr. Richard Zimmerman, my dissertation advisor, for his generous support for cruises, travels, and meetings, his encouragement to train me as an independent scientist, and his great patience in reading and commenting on my papers. I am also very thankful for the comments and contributions from the committee members: Drs. Larry Atkinson, Margaret Mulholland, Zhonghai Jin, and Mark Havey, and their patience to read the dissertation. I also thank my colleagues, David Ruble, Dr. Victoria Hill, Dr. Jian Wang, Dr. Zhiping Mei, Margaret Stoughton, Jasmine Cousins, and Ilaria Nardello, for their help with field sampling, data processing, lab works, and their comments on the paper draft. Special thanks to David Ruble for his highly trained skills for field works and data processing. I am grateful to my wife, Yanzhu Guo, and my parents for their endless love and strong support in the past years. I am grateful to many people in CCPO and OEAS without whom the endeavor would have been much harder. I also thank the crew of R/V Fay Slover for their skillful operations during the local cruises in the lower Chesapeake Bay. Ken Rutledge and his colleagues also helped to collect water samples from the Chesapeake Light Tower (CLT). Dr. Stephane Maritorena kindly provided the IDL code for GSM01 model. This research was supported by the National Aeronautics and Space Administration (NASA) contract NNG04GN77G. This study is also dedicated to the memory of Dr. Glenn Cota, my original advisor of graduate studies.

TABLE OF CONTENTS

LIST OF TABLES

LIST OF FIGURES

Figure Page

CHAPTER 1

INTRODUCTION

Since the launch of the Coastal Zone Color Scanner (CZCS) in 1978, satellites such as Sea-viewing Wide-Field-of-view Sensor (SeaWiFS), MODerate-resolution Imaging Spectrometer (MODIS), and Global Imager (GLI), have revolutionized our ability to exploit ocean color in the study of water quality and biogeochemical processes [*IOCCG*, 1999, 2000]. Compared to the traditional shipboard investigations, space-borne remote sensing provides synoptic data and excellent spatial coverage, even for remote sites (e.g. the Arctic) [*IOCCG*, 1999, 2000; *Kirk*, 1994; *Martin*, 2004; *Robinson*, 2004]. This technology, however, is limited by accuracy level of the retrieved products and poor knowledge of the derived in-water properties [*IOCCG*, 1999, 2000; *Kirk*, 1994; *Martin*, 2004]. [1]

Instead of recording the in-water properties directly, space-borne sensors estimate spectral radiometric quantities, such as total upward radiance [$L_t(\lambda)$] and downwelling plane irradiance [$E_d(\lambda)$] (notations used in this study are also shown on Table 1.1; for simplicity, the wavelength symbol, λ, will be omitted), from which important biogeochemical properties (e.g. chlorophyll *a* concentration and suspended particulate matter concentration) can be retrieved through empirical or semi-analytic (SA) models [*Albert and Gege*, 2006; *Garver and Siegel*, 1997; *Gordon*, 1989; *Gordon et al.*, 1988; *IOCCG*, 1999, 2000; *Kirk*, 1994; *Lee et al.*, 1998, 1999; *Maritonera et al.*, 2002; *Martin*, 2004; *Mobley*, 1994; *O'Reilly et al.*, 1998, 2000; *Robinson*, 2004; *Siegel et al.*, 2000].

This dissertation follows the style of Journal of Geophysical Research (Ocean).

Downwelling plane irradiance (E_d) is derived simply from direct solar beam and diffuse sky radiation [*Martin*, 2004; *Mobley*, 1994; *Robinson*, 2004]. Total upward radiance (L_t), however, consists of water-leaving radiance (L_w), in addition to the atmospheric components contributed from Rayleigh scattering (L_r), aerosol scattering (L_a), Rayleigh-aerosol interaction (L_{ra}), Sun glint (L_g), and white caps from ocean waves (L_{wc}) [*Gordon*, 1997; *Gordon and Wang*, 1994a, 1994b; *Martin*, 2004; *Robinson*, 2004; *Siegel et al.*, 2000; *Wang*, 1999, 2006; *Wang and Bailey*, 2001; *Wang et al.*, 2001]:

$$L_t = L_r + L_a + L_{ra} + tL_{wc} + tL_g + tL_w \tag{1.1}$$

where t represents the atmospheric diffuse transmittance factor accounting for the radiance propagation from the sea surface to the sensors. Except for L_w, the other terms in the right side of Eq. (1.1) represent atmospheric contamination of the oceanic signal from aerosol scattering that produces over 90% of L_t at the top of the atmosphere (TOA) [*Martin*, 2004; *Robinson*, 2004]. The processes of atmospheric correction by theoretical and statistical estimates are not the focus of this study, but can be found in many sources [*Gordon*, 1997, 1999, 2003, 2005; *Gordon and Wang*, 1994a, 1994b; *Siegel et al.*, 2000; *Wang*, 1999, 2006; *Wang and Bailey*, 2001; *Wang et al.*, 2001] or NASA Ocean Color website (http://oceancolor.gsfc.nasa.gov/VALIDATION/atm.html).

The relationship between remotely sensed ocean color and water quality is complicated by a number of issues, including the fact that L_w represents < 10% of L_t observed from space. A beam of light propagating through the water is altered by absorption (a) and scattering (b) from four components: water molecules, phytoplankton, colored dissolved organic matter (CDOM), and suspended non-pigmented particles [*Mobley*, 1994]. Knowledge of these inherent optical properties (IOPs) forms the basis

for understanding the geometric and spectral distribution of light within the water column and its impact on L_w. Except for pure water, whose absorption (a_w) and scattering (b_w) spectra are well defined functions of temperature and salinity [*Pope and Fry*, 1997; *Smith and Baker*, 1981], the absorption and scattering from phytoplankton, CDOM, and non-pigmented particles are highly variable in time and space, especially in coastal waters where they often result from riverine discharge and sedimentary resuspension [*Babin et al.*, 2003a, 2003b; *Bricaud et al.*, 1995, 1998; *DeGrandpre et al.*, 1996; *Gordon and Morel*, 1983; *Harding et al.*, 2005; *Johnson et al.*, 2001; *Kirk*, 1994; *Kowalczuk*, 1999; *Mobley*, 1994; *O'Reilly and Zetlin*, 1998; *Rochelle-Newall and Fisher*, 2002]. There are two kinds of scattering: density fluctuation scattering and particle scattering [*Kirk*, 1994]. In general, CDOM does not occur in high enough concentration to affect the density fluctuation of water and is too small to contribute to particle scattering.

This study focused on the relationships between ocean color and the optical properties of coastal waters of the southern Chesapeake Bay. Unlike oceanic Case 1 waters in which phytoplankton and their degradation products, in addition to pure water, are primarily responsible for light absorption and scattering, this coastal area is characterized by Case 2 waters in which terrestrially derived and/or resuspended CDOM and sediment typically have stronger effects on absorption and scattering than phytoplankton [*Babin et al.*, 2003a, 2003b; *Boss et al.*, 2001a, 2001b, 2004; *Bricaud et al.*, 1995, 1998; *Carder et al.*, 1989; *Gordon and Morel*, 1983; *Harding et al.*, 2005; *IOCCG*, 2000; *Johnson et al.*, 2001; *Kirk*, 1994; *Kowalczuk*, 1999; *Loisel and Morel*, 1998; *Mobley*, 1994; *Magnuson et al.*, 2004; *Rochelle-Newall and Fisher*, 2002]. Therefore, the first purpose of this study was to investigate the inherent optical properties

(IOPs) and develop regionally specific algorithms to retrieve IOPs from ocean color for this coastal region (Chapter 2).

The Case 2 environments characterized by estuarine and coastal waters represent only 8% of ocean surface, but they support more than 60% of human population, produce ~ 90% of world fish catch, and receive 75 to 90% of global suspended river load [*IOCCG*, 2000; *Martin*, 2004]. The Chesapeake Bay, the largest estuary in the United States, is over 190 miles long and 15 miles wide (average), and drains a heavily populated region of ~ 16 million people living in the states of New York, Pennsylvania, Delaware, Maryland, Virginia, and West Virginia, and also the District of Columbia (http://www.chesapeakebay.net). The Chesapeake Bay is also one of the most productive and diverse estuaries in the world, supporting over 2700 species of plants and animals (http://www.cbl.umces.edu/Education/BayInfo.html). However, estuaries like the Chesapeake Bay are also vulnerable to human activity, including resource extraction (e.g. fishing) nutrient and sediment loading from agriculture development, and natural disasters (e.g. hurricanes and global warming) [*Bush*, 2000; *Harding*, 1994; *Martin*, 2004; *Robinson*, 2004]. The creation of tools that improve the ability of remote sensing technology to monitor the water quality and biogeochemical processes throughout the Chesapeake Bay and its nearby continental margin will help protect and improve human life and environmental sustainability, and help provide insights into long-term global change [*Martin*, 2004; *Robinson*, 2004].

Unlike oceanic Case 1 waters in which empirical and semi-analytic (SA) models have proven relatively successful in retrieving the biogeochemical parameters (e.g. concentrations of chlorophyll, CDOM, and sediments), the remote sensing algorithms are

much less reliable in Case 2 waters [*Garver and Siegel*, 1997; *Harding et al.*, 2005; *IOCCG*, 2000; *Lee et al.*, 1998, 1999; *Magnuson et al.*, 2004; *Maritorena et al.*, 2002; *O'Reilly et al.*, 1998, 2000]. In addition to complex IOP conditions, many coastal regions also contain important optically shallow areas that support benthic vegetation, reef building organisms, and other habitat features. Compared to optically deep waters (which are, in practice, defined as those sites in which < 10% of surface E_d reaches the bottom and thus makes an insignificant contribution to L_w), optically shallow waters are these in which bottom reflectance has a significant effect on L_w [*Dierssen et al.*, 2003; *IOCCG*, 2000; *Mobley*, 1994; *Voss et al.*, 2003; *Wittlinger*, 2002; *Zimmerman*, 2003]. If the effect of bottom reflectance is not accounted for in optically shallow environments, the retrievals of IOPs and biogeochemical parameters by the empirical or semi-analytic models can be seriously overestimated. Figure 1.1 shows an example of the spatial distribution of chlorophyll *a* concentration ([Chl]) derived from OC4V4 global ocean color algorithm [*O'Reilly et al.*, 1998, 2000] from SeaWiFS imagery for tropical waters, in which the seagrass meadows and reef-like structures are mis-interpreted as high phytoplankton chlorophyll concentration by very high bottom reflectance (R_b) from carbonate sediments. Thus, the second purpose of this study was to develop relatively simple radiative transfer approaches that would be valid for both oceanic Case 1 waters and complex Case 2 waters, as well as optically shallow environments that can be inverted to retrieve the important IOPs and biogeochemical parameters from remotely sensed ocean color (Chapters 3 and 4).

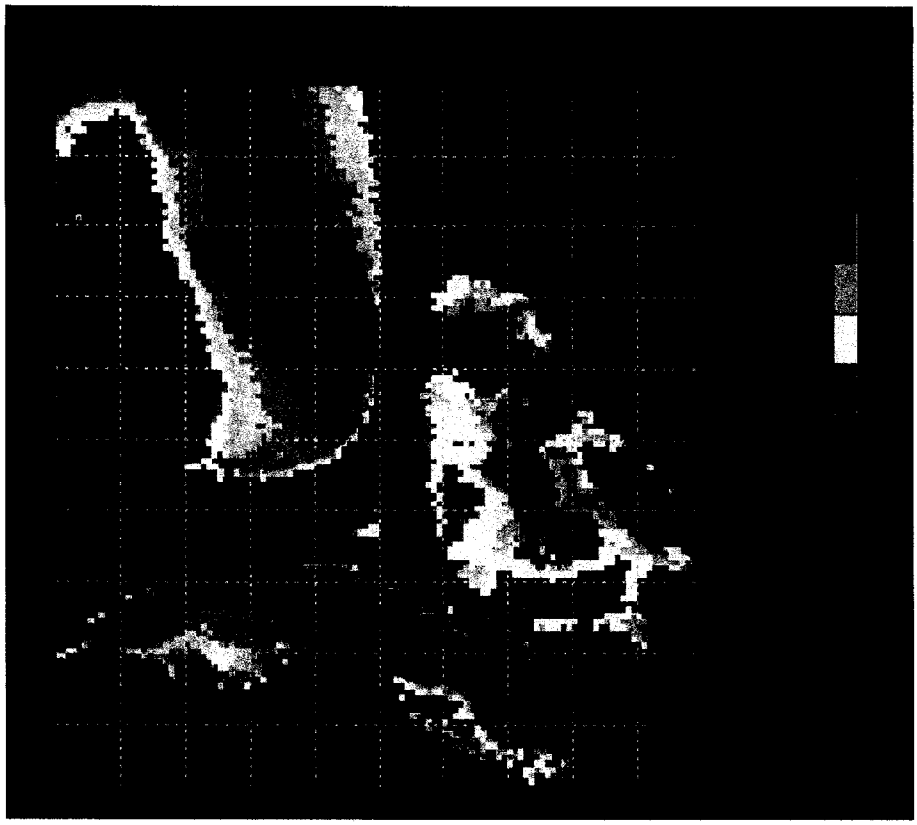

Figure 1.1. SeaWiFS spatial distribution of [Chl] for tropical waters. This monthly (January 2006) average image using the OC4V4 algorithm for the tropical waters surrounding Florida, the Bahamas, and Cuba was obtained from NASA Goddard Space Flight Center (GSFC) based on the GES-DISC Interactive Online Visualization and ANalysis Infrastructure (Giovanni; http://reason.gsfc.nasa.gov/OPS/Giovanni).

Although exact radiative transfer models (RTMs), that calculate the fate of photons traveling through natural waters using statistical model (e.g. Monte Carlo simulations) or employ mathematically sophisticated invariant imbedding techniques based on the Racciti matrix equation (e.g. *Hydrolight*®; *Mobley*, 1994) to provide exact solutions of radiative transfer equations, are powerful for forward modeling to predict the above and submarine light field including remote sensing reflectance (R_{rs}) and diffuse attenuation coefficient (K_d) from IOPs, they can not be inverted to determine IOPs from

R_{rs} and L_w [*Kirk*, 1994; *Mobley*, 1994]. One approach to overcome this deficiency has been to build complete look-up-tables (LUTs) that relate the parameters such as R_{rs} and K_d to IOPs and atmospheric parameters (e.g. solar zenith angle, wind speed, and cloud coverage) [*Lee et al.*, 2005; *Liu et al.*, 2002; *Mobley et al.*, 2005]. This approach, however, is not without its drawbacks. The tables are extremely tedious to compile, but more importantly, they are vulnerable to the non-unique solutions. Radiative transfer approaches, based on the analysis of the results of *Hydrolight*® [*Mobley*, 1994] simulations and adopting two-flow model and asymptotic theory, provide more approximate solutions that are less exact than the analytical approach of the exact RTMs, but they are amenable to inversion to solve for water quality parameters (e.g. [Chl] and IOPs). The problem is to develop radiative transfer approaches that are sufficiently accurate and robust, yet remain amenable to inversion.

Chapter 2 discusses the variation of IOPs and the bio-optical algorithms for the coastal waters of the southern Chesapeake Bay. The application of these regionally specific relationships to retrieve satellite remote sensing products was also assessed. Chapter 3 discusses a radiative transfer approach (PZ06_E_d) that predicts the vertical distribution of downwelling plane irradiance [$E_d(z)$] from IOPs and atmospheric conditions, which is important to estimate E_d reaching the sea-floor and being reflected to contribute to L_w and R_{rs}. Chapter 4 discusses another radiative transfer approach (PZ06_R_{rs}) that predicts R_{rs} from IOPs in both optically deep and shallow water conditions, and assesses its inversion ability to retrieve important water quality and biogeochemical parameters. Finally, a conclusion and future work adoptable from this study are presented in Chapter 5.

Table 1.1. Definitions, symbols, and units of notations used in this study

Definitions	Symbols	Units
Radiometric quantities		
Plane irradiance	E	W m^{-2} nm^{-1}
downwelling plane irradiance	E_d	W m^{-2} nm^{-1}
upwelling plane irradiance	E_u	W m^{-2} nm^{-1}
fraction of directly solar beam	f_{direct}	dimensionless
Upwelling radiance	L_u	W m^{-2} nm^{-1} sr^{-1}
water-leaving radiance	L_w	W m^{-2} nm^{-1} sr^{-1}
upwelling radiance from bottom reflectance	L_{ub}	W m^{-2} nm^{-1} sr^{-1}
Totally upward radiance leaving from the water	L_t	W m^{-2} nm^{-1} sr^{-1}
Sky radiance	L_{sky}	W m^{-2} nm^{-1} sr^{-1}
Rayleigh scattering	L_r	W m^{-2} nm^{-1} sr^{-1}
aerosol scattering	L_a	W m^{-2} nm^{-1} sr^{-1}
Rayleigh-aerosol interaction	L_{ra}	W m^{-2} nm^{-1} sr^{-1}
sun glint	L_g	W m^{-2} nm^{-1} sr^{-1}
white capping effect	L_{wc}	W m^{-2} nm^{-1} sr^{-1}
fraction of L_{sky}/L_t	ρ	dimensionless
Inherent Optical Properties (IOPs)		
Absorption coefficient	a	m^{-1}
water	a_w	m^{-1}
phytoplankton	a_{ph}	m^{-1}
colored dissolved organic matter (CDOM)	a_g	m^{-1}
non-pigmented particles	a_d	m^{-1}
particles	a_p	m^{-1}
CDOM + particle	a_{pg}	m^{-1}
CDOM + non-pigmented particles	a_{dg}	m^{-1}
chlorophyll-specific phytoplankton absorption	a_{ph}^*	m^2 mg^{-1}
Scattering coefficient	b	m^{-1}
water	b_w	m^{-1}
particles	b_p	m^{-1}
Backscattering coefficient	b_b	m^{-1}
water	b_{bw}	m^{-1}
particles	b_{bp}	m^{-1}
Beam attenuation coefficient	c	m^{-1}
Beam optical depth (= cz)	ξ	dimensionless
Single scattering albedo (b/c)	ω_0	dimensionless
Apparent Optical Properties (AOPs)		
Average cosine	$\bar{\mu}$	dimensionless
downwelling plane irradiance	$\bar{\mu}_d$	dimensionless
upwelling plane irradiance	$\bar{\mu}_u$	dimensionless
incident solar light below the surface	$\bar{\mu}_w$	dimensionless

Table 1.1. continued.

Definitions	Symbols	Units
Irradiance reflectance	R	dimensionless
bottom reflectance	R_b	dimensionless
Remote sensing reflectance	R_{rs}	sr^{-1}
Diffuse attenuation coefficient	K	m^{-1}
downwelling plane irradiance	K_d	m^{-1}
upwelling plane irradiance	K_u	m^{-1}
upwelling radiance	K_{Lu}	m^{-1}
Transmittance factor across from water to air	T	dimensionless
Atmospheric diffuse transmittance factor	t	dimensionless
Bidirectional function	Q	sr
Fundamental quantities		
Chlorophyll *a* concentration	[Chl]	$mg\ m^{-3}$
Wavelength in vacuum	λ	nm
Water depth	z	m
maximum water depth	H	m
asymptotic depth	∞	m
Zenith angle	θ	degree
solar zenith angle in air	θ_s	degree
solar zenith angle below the surface	θ_w	degree
sensor zenith angle in air	θ_v	degree
sensor zenith angle below the surface	$\theta_{v'}$	degree
Regression coefficients		
Coefficient concerned with $K_{diffuse}$	A_0, A_1	dimensionless
Coefficient concerned with P	B_0, B_1	dimensionless
Coefficient concerned with $K_d(\infty)$	D_0, D_1	dimensionless
Coefficient concerned with $f_{diffuse}$	g_0, g_1	dimensionless
Quadratic equation for R_{rs} vs. $b_b/(a + b_b)$	l_1, l_2	sr^{-1}
Exponential slope describing vertical change of K_d	P	dimensionless
Exponential decay factor	S	nm^{-1}
CDOM	S_s	nm^{-1}
non-pigmented particles	S_d	nm^{-1}
CDOM + non-pigmented particles	S_{dg}	nm^{-1}
Power slope describing scattering or backscattering	γ	dimensionless

CHAPTER 2

INHERENT OPTICAL PROPERTIES FOR COASTAL WATERS OF THE SOUTHERN CHESAPEAKE BAY

2.1. Background

The knowledge of in-water inherent optical properties (IOPs) is essential for making biogeochemical inferences from ocean color [*Garver and Siegel*, 1997; *Gordon et al*, 1988; *Kirk*, 1994; *Lee et al.*, 1998, 1999; *Maritorena et al.*, 2002; *Martin*, 2004; *Mobley*, 1994; *Morel and Maritorena*, 2001; *Reynolds et al.*, 2001; *Robinson*, 2004]. The relevant IOPs include absorption (a) and scattering (b) from four basic components: pure water, pigmented phytoplankton, non-pigmented particles, and colored dissolved organic matter (CDOM) [*Mobley*, 1994]. IOPs co-vary with chlorophyll *a* concentration ([Chl]) strongly in oceanic Case 1 waters, but relatively weakly in Case 2 waters due to strong contributions of CDOM and sedimentary particles from riverine discharge and/or sedimentary resuspension [*Babin et al.*, 2003a, 2003b; *Boss et al.*, 2001a, 2001b, 2003; *Bricaud et al.*, 1995, 1998; *Carder et al.*, 1989; *Gordon and Morel*, 1983; *Gould et al.*, 1999; *Harding et al.*, 2005; *IOCCG*, 2000; *Johnson et al.*, 2001; *Kirk*, 1994; *Kowalczuk*, 1999; *Loisel and Morel*, 1998; *Magnuson et al.*, 2004; *Mobley*, 1994; *Morel and Maritorena*, 2001; *Rochelle-Newall and Fisher*, 2002].

The IOPs of Case 2 waters are poorly documented compared to the data sets for Case 1 waters. We do not know, for example, how differences in the taxonomic composition of phytoplankton populations contribute to the observed difference in phytoplankton absorption between Case 1 and Case 2 waters, or among different regions

characterized by Case 2 waters. Also we do not know whether the general exponential trends for absorption by CDOM or non-pigmented particles derived from Case 1 waters are valid in Case 2 waters. Further, the general decay trends for scattering and backscattering have not been extensively investigated in Case 2 environments, and the backscattering ratio (b_b/b) has been largely neglected. A predictive understanding of these relationships will be critical to the development of reliable algorithms for Case 2 waters, and for understanding the optical bases for regional and temporal differences.

Clearly, a global understanding of the optical properties of Case 2 waters cannot be achieved from a single regional study. However, the development of robust regional algorithms will be required before a global synthesis can be attempted. The Chesapeake Bay represents the largest estuary in North America, and its riverine discharge impacts the coastal environment of the entire Middle Atlantic Bight (MAB) [*Mann and Lazier*, 1996; *O'Reilly and Zetlin*, 1998]. Consequently, understanding the optical properties of the coastal region of the southern Chesapeake Bay is important to exploit remote sensing tools in the analysis of coastal waters. The main objective of this chapter was to develop regional algorithms appropriate to retrieve biogeochemical characteristics of the southern Chesapeake Bay from remotely sensed imagery.

2.2. Methods

2.2.1 Study region and experience cruises

Bio-optical observations were conducted along Virginia/North Carolina coast and the southern Chesapeake Bay (Figure 2.1). The shallow waters of this largest estuary in North America are characterized by periodic freshwater outflow plumes and strong

sedimentary resuspension [*Acker et al.*, 2005; *Harding*, 1994; *Johnson et al.*, 2001; *O'Reilly and Zetlin*, 1998]. The volume of riverine outflow from Chesapeake Bay sets up a seaward surface flow and a landward subsurface flow that accounts for much of the inter-annual salinity variation in the Middle Atlantic Bight [*Acker et al.*, 2005; *Boucourt*, 1981; *Harding*, 1994; *Johnson*, 2001; *Mann and Lazier*, 1996; *O'Reilly and Zetlin*, 1998; *Rennie et al.*, 1999]. Historical records confirmed that the Chesapeake Bay outflow plume frequently extends beyond the Chesapeake Light Tower (CLT, Figure 2.1) during wet seasons (e.g. February and September) but rarely in dry seasons (e.g. July and August) [*Arnone and Gallacher*, 1996; *Austin*, 2002]. The forces of freshwater run-off and semidiurnal tidal mixing combine with shallow bathymetric features to create a primary frontal zone from inside the estuary along the Chesapeake Channel to Cape Henry and along the coastal margins of Virginia and North Carolina [*Acker et al.*, 2005; *Chang and Dickey*, 2001; *Chang et al.*, 2002; *Harding*, 1994; *Harding et al.*, 2005; *Mann and Lazier*, 1996; *Sletten et al.*, 1999]. Thus, water types (Case 1 vs. Case 2) vary in their degree of freshwater domination depending upon season (wet vs. dry) and proximity to the rivers that drain into the Bay [*Acker et al.*, 2005; *Chang and Dickey*, 2001; *Chang et al.*, 2002]. The resulting complex environment presents significant challenges to understand optical observations that span both Case 1 and Case 2 water types.

Four surveys were included in this study (Table 2.1 and Fig. 2.1): (1) Chesapeake Outflow Plume Experiment during September 15th - 26th, 1996 (COPE-1), including 71 main stations (complete optical characterization and multi-depth water sampling) along the northern and southern Transects and 153 surface stations (surface water sampling only); (2) time-series observations at the Chesapeake Light Tower (CLT); (3)

Chesapeake Bay Mouth Surveys (CBMS); (4) CLT Transects along the southern transect (CLT-T) from Cape Henry to ~6.5 km east of the CLT. Of the 71 main optical stations occupied during COPE-1, three eastern-most stations (Station 69: 74.973 W, 35.729 N; Station 70: 74.718 W, 35.411 N; and Station 71: 75.000 W, 36.030 N) were located in Case 1 waters near the Gulf Stream (Fig. 2.1). The bottom depths of this study area were usually less than 20 m, and the mean depth around CLT was ~ 11 m.

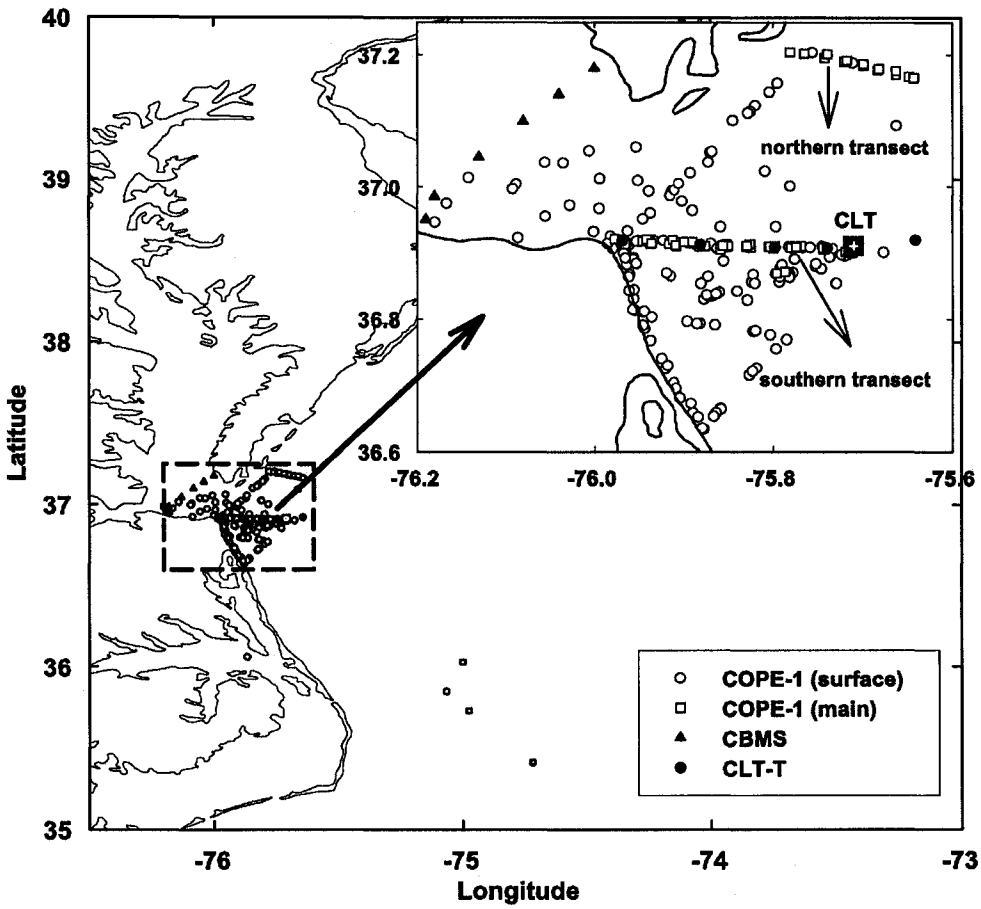

Figure 2.1. Locations of all sampled stations.

Table 2.1. Survey descriptions

Survey	Period	Station #	Measurements*
Chesapeake Outflow Plume Experiment (COPE-1)	09/1996	71 (main) & 153 (surface)	a, b, c, b_b, [Chl], salinity
Chesapeake Light Tower Time-series (CLT)	02/2000 – 09/2005	77 (surface)	a, b_b, [Chl], salinity, R_{rs}
Chesapeake Bay Mouth Survey (CBMS)	09/2004 – 05/2005	20	a, [Chl], salinity
Chesapeake Light Tower Transect (CLT-T)	04/2005 – 09/2005	15	a, b, c, b_b, [Chl], K_d, salinity

* list only those measurements analyzed in this study.

Water temperature and salinity data were obtained from 267 CTD records during COPE-1, 27 records during CLT surveys, and 15 records from CLT-T. The monthly freshwater discharge record of the Susquehanna River measured at U. S. Geological Survey (USGS) Conowingo Station (http://waterdata.usgs.gov/nwis/discharge), which accounts for ~ 60% of total freshwater inputs into Chesapeake Bay, was used as a proxy for the total fresh water discharge into the Chesapeake Bay [*O'Reilly and Zeltin*, 1998].

2.2.2. Discrete measurements of [Chl] and absorption

Water was collected at two or three depths (surface and bottom, plus an intermediate depth) using Niskin bottles and/or plastic buckets. Particles were collected by filtering 100 to 400 ml of seawater through 25mm Whatman® GF/F filters. Chlorophyll *a* and phaeopigment concentrations were determined fluorometrically from the particle samples extracted in 90% acetone at -20°C for ~24 hours [*Parsons et al.*, 1984].

Determining and processing of spectral absorption followed the recommendations of NASA's ocean optics protocols [*Mitchell et al.*, 2002, and references therein]. The

pure water absorption spectrum [$a_w(\lambda)$] of *Pope and Fry* [1997] was used for all calculations performed here. Absorption of total particles [$a_p(\lambda)$] and non-pigmented particles [$a_d(\lambda)$] was determined by the filter pad technique, before and after methanol extraction, using a Shimadzu UV2401 scanning spectrophotometer fitted with an integrating sphere or a UV160 scanning spectrophotometer using an opal glass diffuser [*Kishino et al.*, 1985; *Mitchell et al., 2002*]. Phytoplankton absorption [$a_{ph}(\lambda)$] was calculated as [$a_p(\lambda) - a_d(\lambda)$]. CDOM absorption [$a_g(\lambda)$] was determined in a 10 cm quartz cuvette referenced to a Milli-Q pure water blank after water samples had been filtered through a 0.2 μm Nucleopore® membrane. Null corrections were made by subtracting the means at 790 to 800 nm and 690 to 700 nm for particulate and CDOM absorbance, respectively. Chlorophyll-specific phytoplankton absorption [$a_{ph}^*(\lambda)$] was calculated by normalizing $a_{ph}(\lambda)$ to [Chl]. The total absorption [$a(\lambda)$] was calculated as [$a_p(\lambda) + a_g(\lambda) + a_w(\lambda)$].

Non-pigmented particulate and CDOM absorption spectra typically obey an exponential decay function [*Babin et al.*, 2003b; *Kirk*, 1994; *Mobley*, 1994; *Rochelle-Newall and Fisher*, 2002] of the form:

$$a_x(\lambda) = a_x(\lambda_0) \times \exp[-S_x(\lambda - \lambda_0)] \quad (2.1)$$

where x represents CDOM (g), non-pigment particles (d), or their sum (dg). The exponential decay factor (S) was derived from non-linear regression. The reference wavelength (λ_0) was set to 442 nm in this case. S_g and S_{dg} were calculated between 350-500 nm to eliminate the influence of noise at longer wavelengths, while S_d was calculated over specific wavelength regions (350-400, 480-620, plus 710-750 nm) to avoid errors

associated with incomplete pigment extraction prior to the measurement of absorption spectra [*Babin et al.*, 2003b]. The calculation of S_{dg} did not exclude the pigment band (400 – 480 nm) due to the limited wavelength number and the general CDOM domination in this range.

2.2.3. Continuous Vertical profiles for scattering and backscattering

In-water profiles of total absorption [$a(\lambda)$] and total attenuation coefficient [$c(\lambda)$] were made with a WETLabs *ac*-9 submersible spectrophotometer at nine wavelengths (412, 440, 488, 510, 555, 630, 650, 676, and 715 nm) at the main optical stations during COPE-1 and at all CLT-T stations. Temperature and salinity correction was applied to the *ac*-9 data and the absorption was corrected for scattering effect [*Pegau et al.*, 2003; *Zanveld et al.*; 1994]. The scattering coefficient of pure seawater [$b_w(\lambda)$] was taken from *Smith and Baker* [1981]. The total scattering coefficient [$b(\lambda)$] was determined by [$c(\lambda) - a(\lambda)$], and the particulate scattering coefficient [$b_p(\lambda)$] was determined as the difference [$b(\lambda) - b_w(\lambda)$].

The total backscattering coefficient [$b_b(\lambda)$] was determined from a bbc-4 Maffione sensor at four wavelengths (440, 510, 590, and 665 nm) during COPE-1 and a HOBI Labs HydroScat-6 backscattering meter (HS-6) at six wavelengths (442, 490, 510, 555, 676 and 852 nm) at CLT and CLT-T stations by following manufacturers' protocols [*Zaneveld et al.*, 2003; http://www.hobilabs.com/]. The backscattering coefficient of pure seawater [$b_{bw}(\lambda)$] was assumed to be isotopic, and therefore half of $b_w(\lambda)$. The particulate backscattering coefficient [$b_{bp}(\lambda)$] was determined as the difference [$b_b(\lambda) - b_{bw}(\lambda)$].

Measurements from continuous vertical profiles were binned to 1 m intervals. The linear and non-linear regressions were evaluated from TableCurve 2D v5.01 software (SYSTAT Software Inc.).

2.2.4. SeaWiFS imagery

SeaWiFS images of the lower Middle Atlantic Bight (MAB) (longitude ranging from 79° W to 73° W, and latitude ranging from 34° N to 40° N degrees) were obtained from NASA Goddard Space Flight Center (GSFC) through the Ocean Color Web (http://oceancolor.gsfc.nasa.gov/). A relatively clear day (June 2nd, 2003) was selected for the detailed processing. The SeaWiFS Data Analysis System software (SeaDAS v4.7) was used to process the Level-1A image ('S2003153165817.L1A_MLAC.x.hdf') to Level-2 and Level-3 mapped images, including the following products: water-leaving radiance (L_w), remote sensing reflectance (R_{rs}), [Chl] calculated from the OC4V4 algorithm (chl_oc4) [*O'Reilly et al.*, 1998, 2000], and diffuse attenuation coefficient at 490 nm (K_{490}_Muller) [*Muller*, 2000]. A semi-analytic (SA) inverse model, called GSM01 [*Garver and Siegel*, 1997; *Maritorena et al.*, 2002], based on the quadratic relationship between R_{rs} and the ratio of $b_b/(a+b_b)$, was modified with the regionally specific IOP relationships (GSM01 was then renamed as GSM01-CLT and detailed in Chapter 4) to retrieve the direct products including [Chl], $a_{dg}(443)$, and $b_{bp}(443)$ for SeaWiFS Level-3 mapped image. Other products, such as $a_g(443)$, the average diffuse attenuation coefficient of the downwelling irradiance at 490 nm from surface down to one beam optical depth ($\xi = cz$) [$K_d(490)$], and salinity, were also retrieved, as discussed in next section and Chapter 3.

2.3. Results and discussion

2.3.1. Experimental conditions

The Chesapeake Bay undergoes a seasonal cycle of freshwater discharge that peaks in winter-spring, with occasional sub-peaks in summer-fall (Fig. 2.2). Freshwater discharge plays a critical role in setting up the physical and biological environments of the southern Chesapeake Bay coastal waters [*Acker et al.*, 2005; *Arnone and Gallacher*, 1996; *Austin*, 2002; *Harding et al.*, 2005; *Johnson et al.*, 2001; *Magnuson et al.*, 2004; *Mann and Lazier*, 1996]. The monthly discharge rate for this selected image (June 2nd, 2003) is only about 1/3 of that at winter-spring season (Fig. 2.2) and, therefore, represents a dry season example.

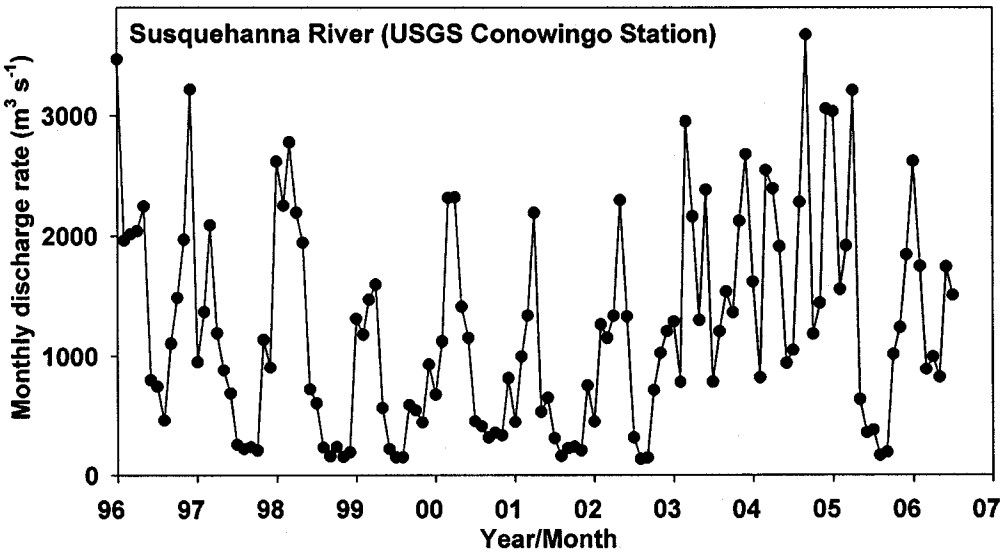

Figure 2.2. Monthly freshwater discharge rate of Susquehanna River. Data were recorded at USGS's Conowingo (Maryland) Station during 1996 – 2006. Annual winter-spring peaks and occasional summer-fall sub-peaks were evident. Data points after September 2005 are provisional and subject to revision as of the accession on August 3, 2006.

2.3.2. Absorption

Phytoplankton absorption—Phytoplankton absorption at 442 nm [$a_{ph}(442)$] was significantly ($r^2 = 0.71$, $P < 0.001$) related to [Chl] by a power function (Fig. 2.3) similar to that of *Bricaud et al.* [1995, 1998]:

$$a_{ph}(442) = 0.053 \times [Chl]^{0.707} \tag{2.2}$$

However, the observations of $a_{ph}(442)$ in this study region were significantly higher ($t_{2,579} = 15.5$, $P < 0.001$) than those predicted from *Bricaud et al.* [1998] for Case 1 waters, especially at higher phytoplankton concentration condition (Fig. 2.3). Higher $a_{ph}(442)$ values can be explained by the difference in taxonomic composition and/or package effects between phytoplankton populations of Case 1 and Case 2 waters [*Babin et al.*, 2003b; *Bricaud et al.*, 1995, 1998; *Trees et al.*, 2000]. The dominant phytoplankton in lower Chesapeake Bay are typically cyanophyceans and chlorophyceans in March, with diatoms increasing in abundance during the summer and fall [*Marshall*, 1981].

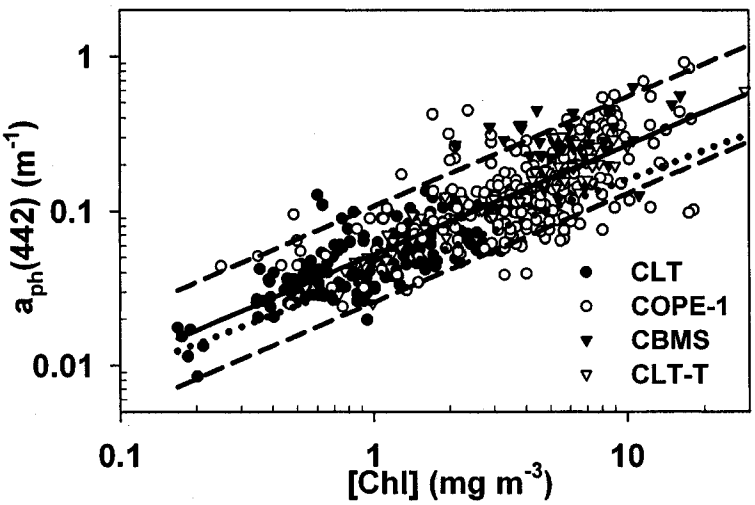

Figure 2.3. Relationship between phytoplankton absorption and [Chl]. Solid line: log-transformed linear regression; dashed lines: prediction intervals of 90% confidence; dotted line: *Bricaud et al.* [1998] prediction.

The chlorophyll-specific phytoplankton absorption at 676 nm [$a_{ph}^{*}(676)$] decreased significantly ($r^2 = 0.78$, $P < 0.001$) with [Chl]:

$$a_{ph}^{*}(676) = 0.0216 \times [Chl]^{-0.172} \quad (2.3)$$

Equation (2.3) may be useful to show pigment package effect, a consequence of the fact that in the natural waters pigment molecules are not uniformly distributed but contained within discrete packages (e.g. chloroplasts, cells, and cell colonies), which causes a flattening of phytoplankton absorption peak due to self-shading wherever pigments are localized within cell membranes [*Duysens*, 1956; *Kirk*, 1994]. *Bricaud et al.* [1995] suggested that the package effect should increase from oligotrophic waters dominated by small-cell organisms to eutrophic waters dominated by large-cell species (Fig. 2.4). *O'Reilly and Zetlin* [1998] also reported that high chlorophyll areas were often dominated by large cells (net plankton) accounting 40% to 80% of [Chl] in near-shore areas of the Middle Atlantic Bight. The data set in this study showed that the package effect for the coastal waters of the Chesapeake Bay was medium strong with the mean effect close to *Bricaud et al.* [1995] model for [Chl] = 1.0 mg m^{-3} (Fig. 2.4).

The predictability of the spectral phytoplankton absorption [$a_{ph}(\lambda)$] from [Chl] is important for semi-analytic inverse models (e.g. GSM01). Instead of expressing $a_{ph}(\lambda)$ as individual power functions similar to Eq. (2.2), or as $a_{ph}^{*}(\lambda) \times [Chl]$, a linear regression between $a_{ph}(\lambda)$ and $a_{ph}(442)$ was applied [*Barnard et al.*, 1998] and expressed $a_{ph}(\lambda)$ as: $a_{ph}(\lambda) = a_{ph}(442) \times \frac{a_{ph}(\lambda)}{a_{ph}(442)}$. The linear regression between $a_{ph}(\lambda)$ and $a_{ph}(442)$ was significant ($r^2 > 0.9$ for 400 to 690 nm), and the spectrum of regression slopes [$a_{ph}(\lambda)/a_{ph}(442)$] were shown on Fig. 2.5.

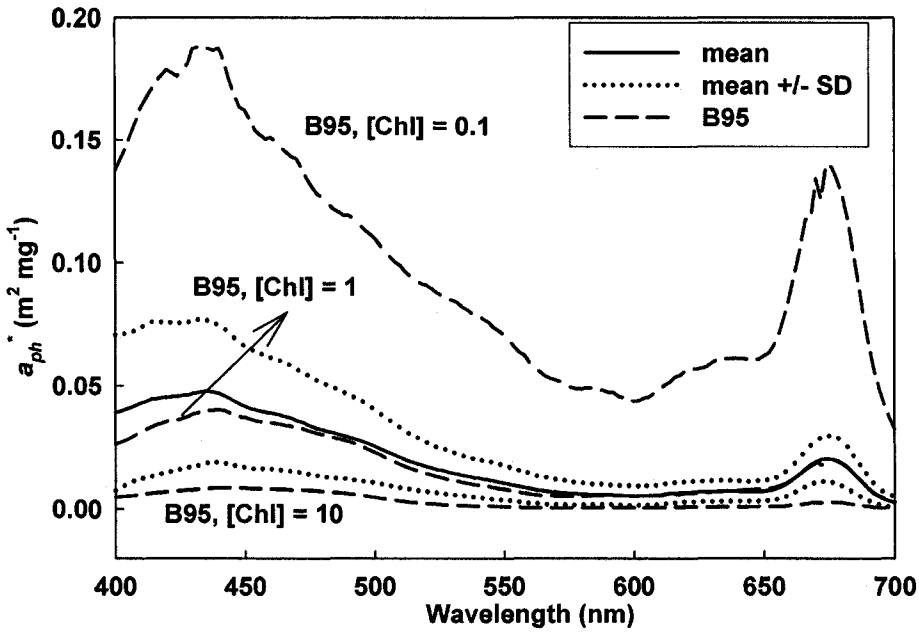

Figure 2.4. Mean spectrum of chlorophyll-specific phytoplankton absorption (a_{ph}^*). Solid line: mean spectrum; dotted lines: the upper and lower limits of one standard deviation (SD) away from the mean spectrum; dashed lines: predictions from *Bricaud et al.* [1995] (B95) for [Chl] = 0.1, 1, and 10 mg m^{-3}.

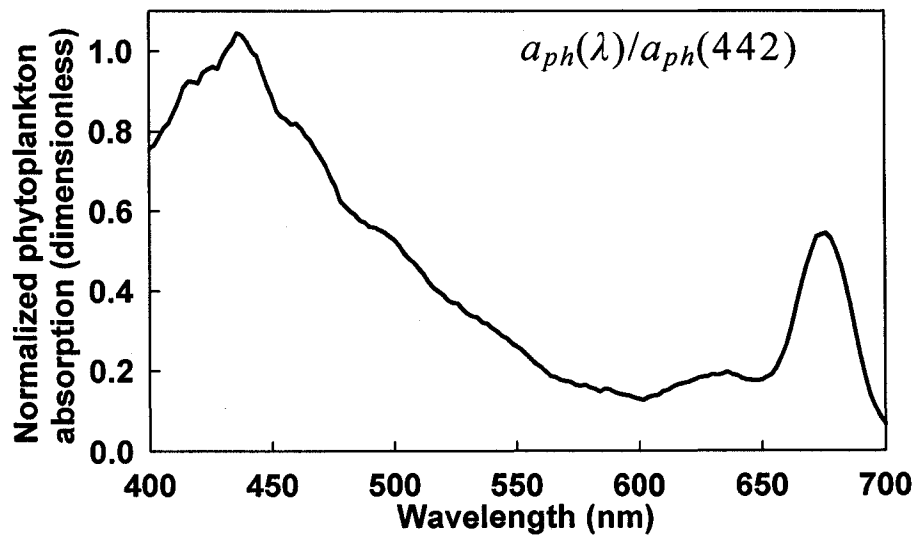

Figure 2.5. Spectrum of normalized phytoplankton absorption to 442 nm.

Absorption by CDOM and non-pigmented particles—The exponential decay factor (S) in Eq. (2.1) is very useful in predicting $a_g(\lambda)$ and $a_d(\lambda)$ from R_{rs} [*Mobley*, 1994; *Garver and Siegel*, 1997; *Maritorena et al.*, 2002]. The coefficients of determination for Eq. (2.1) in this dataset were very high (most $r^2 > 0.95$). The mean ± SE of decay factors of $a_g(\lambda)$, $a_n(\lambda)$, and $a_{dg}(\lambda)$ were $S_g = 0.0169 \pm 0.0001$ ($n = 625$), $S_d = 0.0101 \pm 0.0001$ ($n = 593$), and $S_{dg} = 0.0151 \pm 0.0001$ ($n = 570$) nm^{-1}, respectively. The values were 4% and 18% lower ($t_{2, 625} = 8.0$, $P < 0.001$, and $t_{2, 592} = 38.8$, $P < 0.001$) for S_g and S_d, respectively, than the means reported by *Babin et al.* [2003b] for European coasts of the Wadden, Adriatic, Mediterranean, Baltic, and North Seas with $S_g = 0.0176 \pm 0.0001$ and $S_d = 0.0123 \pm 0.0001$. The S_{dg} value was 27% lower than the slope (0.0206) typically used in GSM01 [*Martitorene et al.*, 2002]. These differences highlight the potential need to develop regional algorithms for coastal environments. For example, the application of the standard GSM01 value of 0.0206 for S_{dg} yields an 18% increase in the value of $a_{dg}(412)$ calculated from $a_{dg}(442)$ than from this regionally specific mean value of 0.0151, which usually causes higher $b_{bp}(442)$ retrieved from GSM01 than the observations in the lower Chesapeake Bay in the same beam attenuation coefficient (c) level.

Fraction of absorption by components—In coastal waters, CDOM often dominates the absorption spectrum, particularly at short wavelengths (i.e. <500 nm). In this study, CDOM absorption (a_g) represented about 66% of total absorption without water ($a_{gp} = a_{ph} + a_d + a_g$) at 400 nm and decreased to about 48% at 556 nm (Table 2.2) as particulate (phytoplankton and non-pigmented particles) absorption became more important at longer wavelengths. The fraction of $a_d(\lambda)$ and $a_{ph}(\lambda)$ varied from 18% to 24% and 16% to 28% between 400 and 556 nm, respectively (Table 2.2). If we define Case 1

waters as those where $a_{ph}(442)$ represents most (> 60%) of $a_{gp}(442)$ [*IOCCG*, 2000], almost all of the data used here became classified as Case 2 water (Figure 2.6).

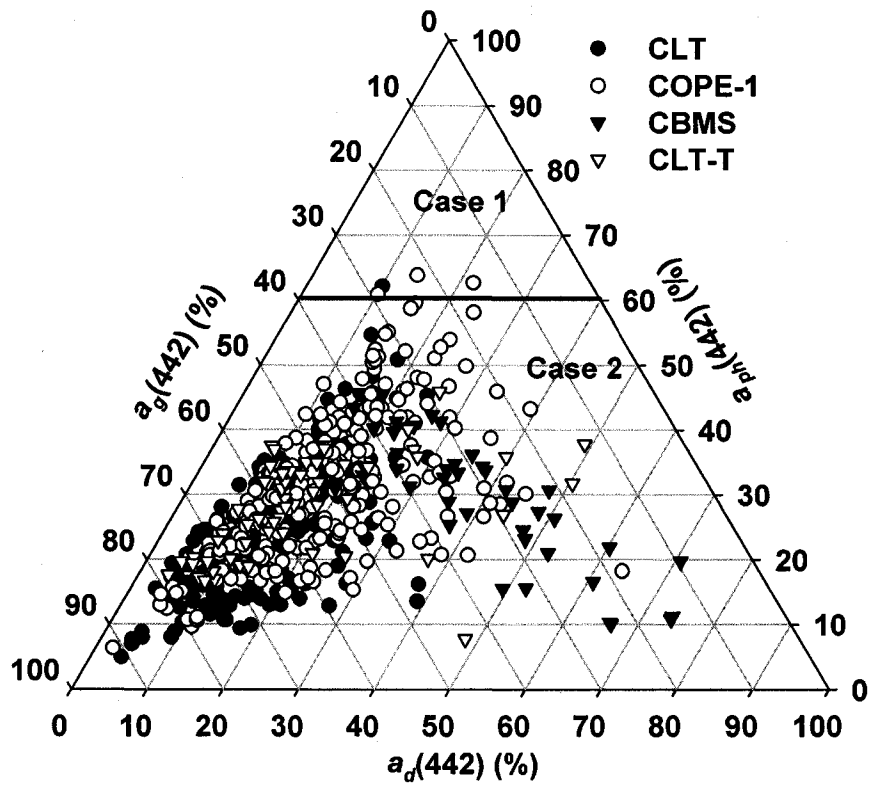

Figure 2.6. Relative percentage of absorption. The considered absorption included non-pigmented particles (a_d), phytoplankton (a_{ph}), and CDOM (a_g) at 442 nm. Case 1 water is defined as the upper part of the triangle where $a_{ph}(442)\% > 60\%$ of $a_{gp}(442)$. The bottom part of the triangle represents Case 2 water.

Table 2.2. Relative percentages of absorption. The considered absorption included non-pigmented particles (a_d), phytoplankton (a_{ph}), and CDOM (a_g). Total data points n = 509. Standard errors (SE) are in parentheses

IOPs	Wavelength (nm)					
(m^{-1})	400	412	442	490	510	556
a_{ph}	15.9 (0.3)	19.9 (0.4)	28.8 (0.5)	33.3 (0.6)	32.4 (0.6)	28.2 (0.7)
a_d	17.9 (0.5)	18.3 (0.5)	18.1 (0.5)	18.7 (0.5)	20.3 (0.5)	24.3 (0.7)
a_g	66.2 (0.7)	61.8 (0.7)	53.2 (0.7)	48.0 (0.8)	47.3 (0.8)	47.5 (0.9)

2.3.3. Scattering and Backscattering

Although accurate knowledge of scattering (b) and backscattering (b_b) is required to apply radiative transfer theory to natural waters [*Mobley*, 1994], they are seldom measured directly. At present, total scattering (b) is usually calculated as $b = c - a$, while backscattering (b_b) is estimated from measurements at a single oblique angle (e.g. 120°) by assuming a constant scattering phase function [*Zaneveld et al.*, 2003, and references therein]. These measurements are difficult and highly dependent on nature of the particles, especially in highly variable coastal waters.

Scattering and backscattering spectra are typically expressed as a power function [*Gordon and Morel*, 1983; *Mobley*, 1994]:

$$b_y(\lambda) = b_y(\lambda_0) \times (\frac{\lambda}{\lambda_0})^{-\gamma} \tag{2.4}$$

where γ is a derived coefficient describing the wavelength-dependence of scattering or backscattering, and the referenced wavelength (λ_0) is individually defined as 510 nm in this study. The log-transformed least-square linear regression of the data set in this study yielded a mean $\gamma \pm$ SE of 0.503 ± 0.008 (n = 995) for particulate scattering (b_p) and 0.929 ± 0.008 (n = 846) for backscattering (b_{bp}). These γ values were both significantly different ($t_{2,\ 994}$ = 66.9, P < 0.001, and $t_{2,\ 845}$ = 8.68, P < 0.001 for scattering and backscattering, respectively) from the typically assigned value of 1, but well within the range from 0 to 4 for wide classes of marine particles [*Gordon and Morel*, 1983; *Gould et al.*, 1999; *Kirk*, 1994; *Mobley*, 1994; *Stramski and Mobley*, 1997]. The difference of γ values for b_p and b_{bp} implies that the particulate backscattering ratio (b_{bp}/b_p) varies with wavelength, which increases the difficulty for the measuring and modeling scattering and

backscattering. However, the Rayleigh-like effects, which are defined as the increase of scattering caused by the fluctuations in molecular density (e.g. various ions including Cl^- and Na^+, and CDOM), will increase the difficulty to separate absorption by CDOM and other molecules from scattering in field measurements [*Kirk*, 1994; *Mobley*, 1994; *Morel et al.*, 2002].

The scattering and backscattering coefficients were less correlated to [Chl] (e.g. $r^2 = 0.38$, $P < 0.001$ for b_p, and $r^2 = 0.42$, $P < 0.001$ for b_{bp} at 510 nm) in this coastal region, indicating that non-phytoplankton particles, either from freshwater discharge or from sedimentary resuspension, contribute more to scattering than algal cells. Such weak relationships are commonly found in typical Case 2 waters [*Gordon and Morel*, 1983]. *Babin et al.* [2003a] applied Mie theory to calculate b_p from the apparent density of particles. For such calculations, the correct selections of the slope of the Junge-type size distribution and refractive index of particles, in addition to the assumption of the ideal spherical particle shape, were required [*Babin et al.*, 2003a; *Mobley*, 1994; *Morel et al.*, 2002]. Although the Laser In-Situ Scattering and Transmissometry (LISST) instruments (Sequoia, Inc.) and other laser-based tools may help to resolve these issues, they have not been commonly investigated in bio-optics [*Mueller et al.*, 2002]. The analyses of the data set in this study found that particulate scattering and backscattering were significantly ($r^2 = 0.65$ and 0.74, and both $P < 0.001$) related to a_d (Fig. 2.7):

$$b_p(510) = 17.13 \times [a_d(510)]^{0.763} \tag{2.5}$$

$$b_{bp}(510) = 0.509 \times [a_d(510)]^{1.007} \tag{2.6}$$

Inversion of Eqs. (2.5) and (2.6) provides a potential method to calculate $a_d(\lambda)$ from remote sensing from which $b_{bp}(\lambda)$ can be retrieved (e.g. from GSM01-CLT). For

example, $a_d(443)$ can be significantly (r^2 = 0.70, P < 0.001) expressed as a power function of $b_{bp}(443)$ (Fig. 2.8):

$$a_d(443) = 1.533 \times [b_{bp}(443)]^{0.782} \quad (2.7)$$

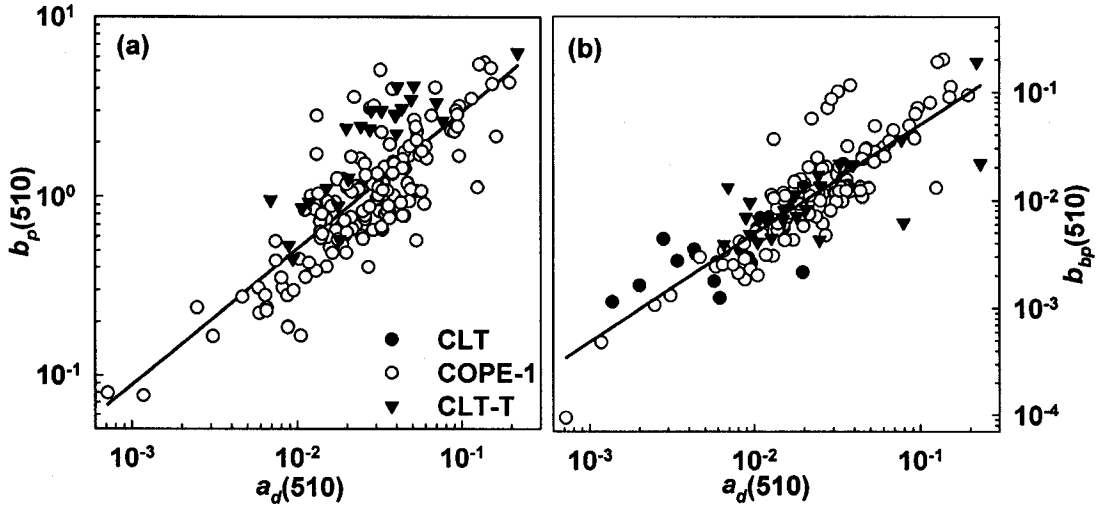

Figure 2.7. Variations of particulate scattering and backscattering with non-pigmented particulate absorption. (a) Particulate scattering (b_p). (b) Backscattering (b_{bp}). The data were log-transformed and the selected wavelength was 510 nm.

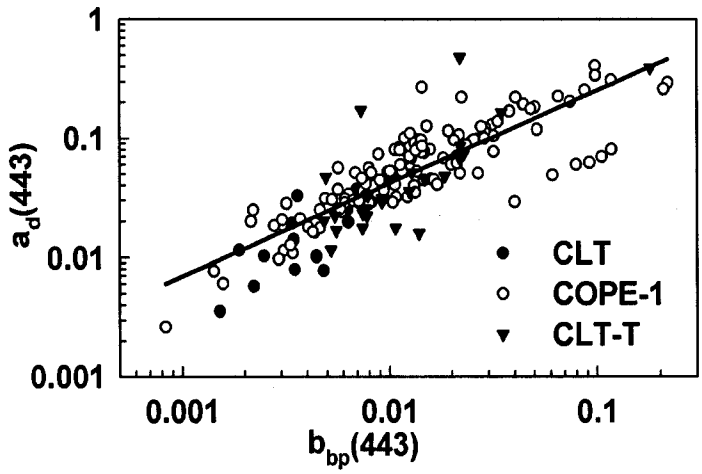

Figure 2.8. Variation of non-pigmented particulate absorption with particulate backscattering. The data were log-transformed and the selected wavelength was 443 nm.

In addition to another direct product of GSM01-CLT, $a_{dg}(\lambda)$, the remotely sensed retrieval of $a_g(\lambda)$ is possible by subtracting $a_d(\lambda)$ estimated from $b_{bp}(\lambda)$ similar as Eq. (2.7). The salinity distribution in a riverine-dominant coastal region is often thought to be mixed conservatively between outflowing freshwater and the local oceanic water [*Austin*, 2002], which often causes a linear relationship between CDOM absorption and salinity (*Kowalczuk*, 1999; *Rochell-Newall and Fisher*, 2002). The validity of this relationship may allow us to monitor the salinity gradient in this southern Chesapeake Bay coastal region from remote sensing.

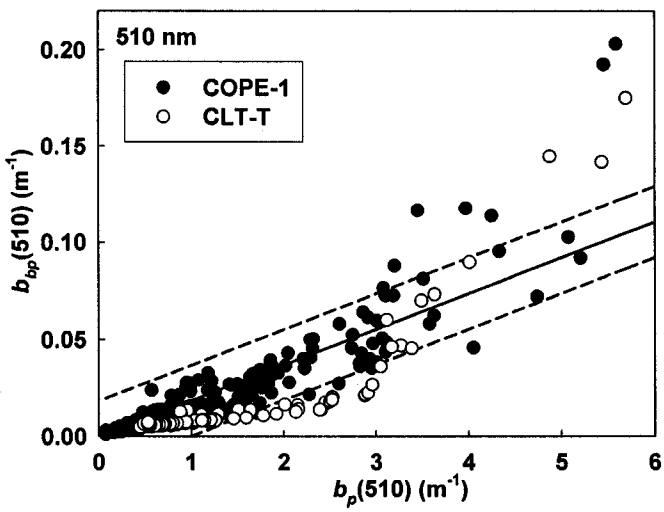

Figure 2.9. Particulate backscattering ratio to scattering at 510 nm. Solid line: the regression slope = 0.0184; dashed lines: prediction intervals of 90% confidence.

The particulate backscattering ratio (b_{bp}/b_p) at 510 nm had the regression mean ± SE (n = 674) of 0.0184 ± 0.0003 (Fig. 2.9), which was very close to *Petzold*'s [1972] value of 0.01833 [*Mobley*, 1994]. There are two groups of particles: phytoplankton and non-pigmented particles. Due to the complicated conditions of coastal waters, the size and concentration of both particle sources vary seasonally and spatially in this coastal

region. For example, riverine outflow tends to increase the phytoplankton number and cell size, while increase the concentration of non-pigmented particles from sedimentary resuspension in combining with wind forcing and tidal mixing [*Harding et al.*, 2005; *O'Reilly and Zetlin*, 1998]. Consequently, the average size of the particles in this coastal region is highly variable with b_{bp}/b_p ranging from 0.005 (phytoplankton-dominant-like environment) to 0.030 (mineral-particle-dominant-like environment) [*Babin et al.*, 2003a; *Ulloa et al.*, 1994].

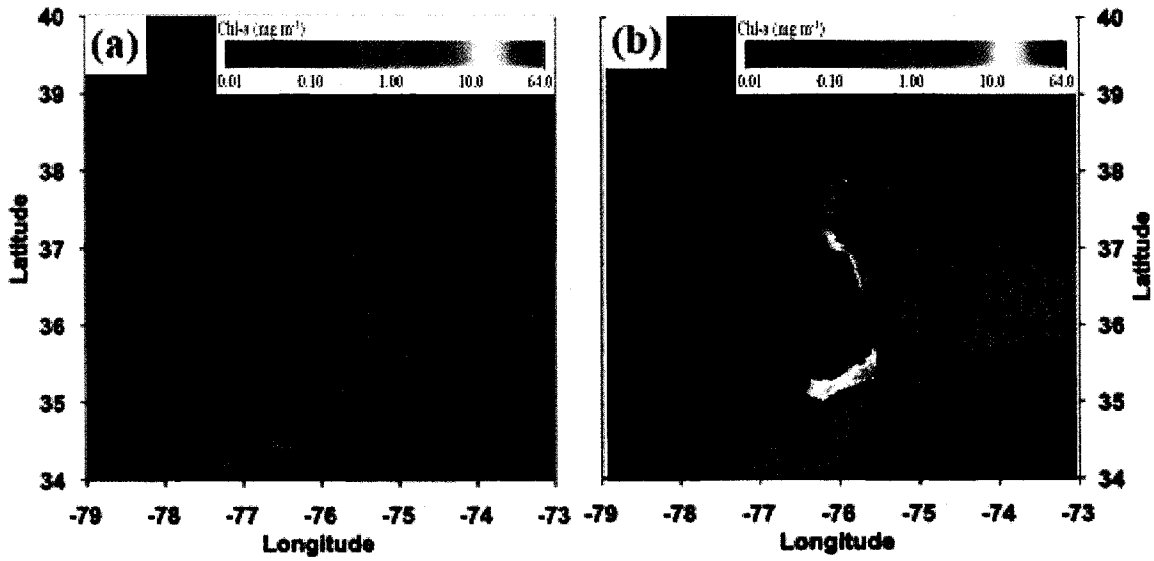

Figure 2.10. SeaWiFS spatial distribution of [Chl]. The data were derived from (a) GSM01-CLT, and (b) OC4V4 algorithm, for lower Middle Atlantic Bight region. The selected date is June 2nd, 2003. Circle symbol: the Chesapeake Light Tower (CLT).

2.3.4. Remote sensing monitoring from SeaWiFS

Compared to the global OC4V4 [Chl] algorithm [*O'Reilly et al.*, 1998, 2000], which often significantly overestimates [Chl] in coastal waters, locally parameterized GSM01-CLT model clearly shows the effect of riverine discharge on the phytoplankton

distribution (Fig. 2.10). As nutrient-rich riverine water flows out of the Bay mouth, the Coriolis effect directs the stream southward along the Virginia/Carolina coast to mix with local oceanic water and causes the upwelling of oceanic water [*Mann & Lazier*, 1996]. The resulting phytoplankton bloom is clearly shown from [Chl] distribution retrieved from GSM01-CLT, especially along the Virginia coast south of the Chesapeake Bay mouth (Fig. 2.10a). The riverine outflow effect is controlled by freshwater discharge rate in upper Chesapeake Bay, which is often low in summer (Fig. 2.2). From the historical record, riverine outflow seldom reaches the Chesapeake Light Tower (CLT) in summer dry season [*Arnone and Gallacher*, 1996]. The GSM01-CLT retrieved [Chl] agrees with this assumption and the imagery of this selected summer date (June 2nd, 2003) clearly shows the front of the estuarine zone and the Atlantic Ocean at the site near the CLT (Fig. 2.10a). The retrieved [Chl] from GSM01-CLT is also reasonable and comparable to the field observations, for example, the field transect conducted on May 18th, 2005 from near Cape Henry to east of the CLT showed the surface [Chl] decreasing from 5.0 to < 1.0 mg m^{-3}. In contrast, [Chl] estimates derived from OC4V4 (Fig. 2.10b) were considerably high and extended further offshore. The GSM01-CLT retrieval suggests that [Chl] in the oceanic waters for this date was limited to 0.5 mg m^{-3} (Fig. 2.10a).

Unlike phytoplankton, whose concentrations are controlled by nutrients, grazing, and light, suspended particle concentrations (as expressed by b_{bp}) are typically controlled by riverine outflow and other physical factors like wind forcing and tidal mixing. Figure 2.11a shows the front of the particle-rich estuarine zone, the particle-poor open Gulf Stream, and mixing in the continental margin between them. The absorption of CDOM plus non-pigmented particles (a_{dg}; Fig. 2.11b), one of three direct products retrieved from

GSM01-CLT, provides similar information as [Chl] and b_{bp}. After subtracting the absorption of non-pigmented particles (a_d) estimated from b_{bp} by the inverse form of Eq. (2.7), the CDOM absorption (a_g; Fig. 2.11c) was derived. Since riverine discharge is the major contributor to CDOM in coastal waters [*Kowalczuk*, 1999; *Rochelle-Newall and Fisher*, 2002], the distribution of a_g also shows the spatial gradient of the freshwater outflow plume from the Bay mouth. Again, the Gulf Stream is recognized to cause the significant decrease of a_g by mixing with the local water (Fig. 2.11c).

Rather than calculating salinity from empirical equations based on band ratios of L_w or R_{rs} [Binding and Bowers, 2003], salinity was derived from a linear relationship with CDOM absorption (a_g). The salinity limits of the freshwater and the oceanic waters was set to 0.0 psu and 36.5 psu, respectively. Since CDOM absorption (a_g) of the oceanic waters is much lower (e.g. < 5%) than that of freshwater water (Fig. 2.11c), , salinity can be expressed as:

$$salinity \approx 36.5 - 36.5 \frac{a_g(443)}{[a_g(443)]_{freshwater}} \tag{2.8}$$

The $a_g(443)$ value of freshwater [$a_g(443)_{freshwater}$] was assumed to the maximum value framed within the longitude from 76.5° W to 76° W and latitude from 37° N to 37.5° N. The derived salinity distribution also appears reasonable. Due to low freshwater discharge rate in the summer, salinity near the mouth was about 20 psu (Fig. 2.11d). Field observations by the Center for Coastal Physical Oceanography, Old Dominion University (http://www.ccpo.odu.edu/~mwott/baymouth/cheshome.html) on June 2003, from which salinity ranged from ~ 18 psu to ~ 24 psu, agree with Fig. 2.11d. The salinity gradient is also obvious from Fig. 2.11d, from which freshwater outflows the Bay mouth and is

mixed with the local Atlantic Ocean and the Gulf Stream. However, the remotely sensed salinity distribution is based on the accurate estimation of CDOM absorption of the freshwater that starts to mix with the local salty waters, which varies daily with the discharge rate and nutrient load from the upper Bay. Thus, selecting the initial a_g for the freshwater remains a challenge. Moreover, the inverse form of Eq. (2.7) does not incorporate CDOM photooxidation, which also may reduce CDOM absorption (a_g) along the salinity gradient. In practice, an accurate image of salinity distribution may be resolved by deploying a series of buoys equipped with CTD and instruments to measure spectral absorption along the salinity gradient line (e.g. from Cape Henry to CLT), from which daily empirical relationships (either linear or non-linear) between salinity and a_g can be applied to remotely sensed imagery.

The retrieved products described above depend on good performance and high capability of the semi-analytic model for various water conditions. However, there are at least two limitations on the application of GSM01 or the modified GSM01-CLT model for coastal waters. First, semi-analytic models like GSM01 require R_{rs} in all wavebands to be retrieved equally accurately, or the products like IOPs and [Chl] retrieved from the inverse modeling via a least-square matching can not work well. Coastal conditions, such as strong CDOM absorption in blue bands, higher concentration of atmospheric aerosols, and non-zero water-leaving radiance (L_w) in infrared bands, often restrict the accurate estimation of R_{rs} from above-water sensors, especially for short wavelengths like 412 and 443 nm. Second, the model needs to be tuned to a regional data set, which, of course, often restricts its application to other regions. For example, the IOP relationships in this study were derived from the data set mostly from the Bay mouth region. When applied

them to upper or middle Bay regions, GSM01-CLT often fails (Figs. 10 and 11). On the other hand, the regionally tuned GSM01 model from the data set observed inside the Bay works for the retrievals of the waters inside the Chesapeake Bay [*Harding et al.*, 2005; *Magnuson et al.*, 2004].

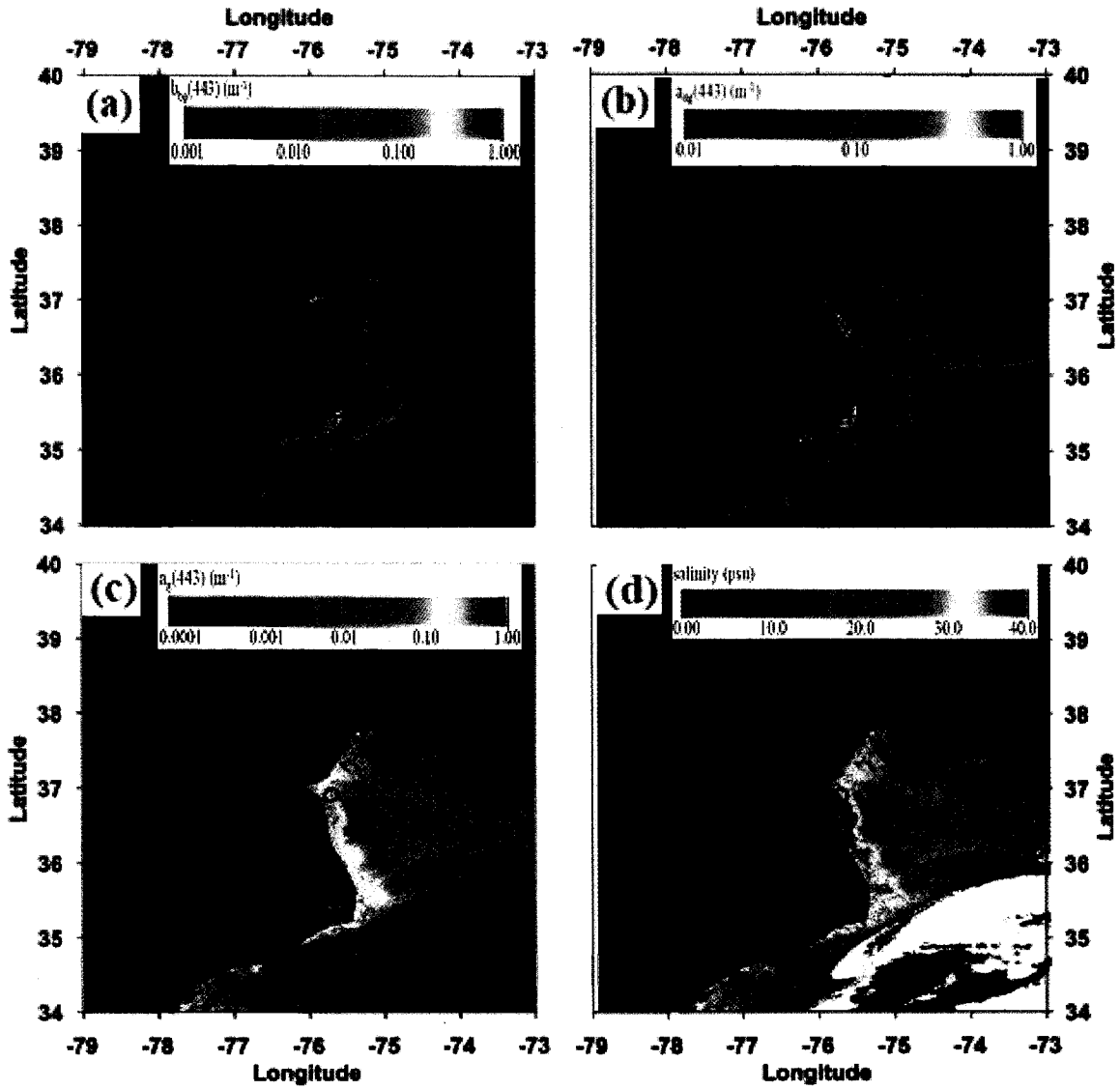

Figure 2.11. SeaWiFS spatial distribution of oceanic parameters for lower Middle Atlantic Bight region. (a) $b_{bp}(443)$]. (b) $a_{dg}(443)$. (c) $a_g(443)$. (d) Salinity. The $b_{bp}(443)$ and $a_{dg}(443)$ data were direct products of GSM01-CLT, while $a_g(443)$ was from $a_{dg}(443)$ by subtracting $a_d(443)$ from Eq. (2.7), and salinity was estimated from Eq. (2.8). The selected date is June 2nd, 2003. Circle symbol: the Chesapeake Light Tower (CLT).

In summary, these analyses of absorption, scattering, and backscattering provided the basis for the required knowledge to inversely retrieve the IOPs and biogeochemical parameters from remote sensing. However, shallow topography of the southern Chesapeake Bay coastal region means that many sites are optically shallow in which bottom reflectance contributes significantly to the water-leaving radiance. The following two chapters will discuss modeling approaches to estimate the vertical distribution of downwelling plane irradiance (E_d) and eventually the remote sensing reflectance (R_{rs}).

CHAPTER 3

MODELING THE VERTICAL DISTRIBUTION OF DOWNWELLING PLANE IRRADIANCE IN OPTICALLY DEEP WATERS

3.1. Background

According to the Lambert-Beer Law, downwelling plane irradiance [$E_d(z)$] decreases exponentially with depth (z):

$$E_d(z) = E_d(0^-)\exp[-\overline{K}_d(z) \times z] \tag{3.1}$$

Typically, $\overline{K}_d(z)$ is defined as the average value of the diffuse attenuation coefficient [$K_d(z)$] from the surface down to depth z. Thus, the relationship between $E_d(z)$ and $K_d(z)$ is critical to study above- and in-water variations in the solar radiative field caused by optical properties of the water and to retrieve bio-optical properties from measurements (including remote sensing) of the radiation field [*Gordon*, 1989; *Kirk*, 1991, 1994; *Mobley*, 1994]. Exact radiative transfer models (RTMs), such as *Hydrolight*® [*Mobley*, 1994], that provide "exact" solution of the radiative transfer equations, are extremely useful in calculating the submarine light field for a given set of inherent optical properties (IOPs). They can not, however, be inverted directly to retrieve important biogeochemical properties, such as the concentrations of chlorophyll *a* ([Chl]), suspended particulate matter, and colored dissolved organic matter (CDOM). Look-up tables (LUTs) generated by compiling the output of multiple simulations over a range of input values have been used to retrieve IOPs from above-water radiance measurements [*Lee et al.*, 2005; *Liu et al.*, 2004; *Mobley et al.*, 2005], but they are vulnerable to the production of non-unique

solutions from the selections of multiple combinations of [Chl], IOPs, and/or solar zenith angle (θ_s).

Although measuring $K_d(z)$ is relatively simple, the relationship between $K_d(z)$ and the IOPs is much more complicated. $K_d(z)$ is an apparent optical property (AOP) which is influenced by the angular structure of the submarine light field (e.g. the incident solar direction) in addition to the characteristics of the medium [*Kirk*, 1994; *Mobley*, 1994]. The development of a simple, robust relationship between K_d and the IOPs of absorption (a), scattering (b), and/or backscattering (b_b) has been a "holy grail" of environmental bio-optics [*Gordon*, 1989; *Kirk*, 1994; *Mobley*, 1994]. The simplest form, provided by *Gordon* [1989] and valid only for limited sky and oceanic conditions (e.g. medium solar zenith angle and absorption-dominant water), is often presented as:

$$K_d = 1.0395 \frac{a + b_b}{\bar{\mu}_w} \tag{3.2}$$

Here, $\bar{\mu}_w$ is defined as the average cosine of the incident angle of direct solar beam just below the surface (θ_w) after accounting for refraction from the solar zenith angle (θ_s) by Snell's Law [*Kirk*, 1994; *Mobley*, 1994]:

$$\sin(\theta_w) = \frac{\sin(\theta_s)}{1.34} \tag{3.3}$$

Kirk [1991, 1994] derived a slightly more complicated relationship from a series of Monte Carlo simulations:

$$K_d = \frac{(a^2 + Gab)^{0.5}}{\bar{\mu}_w} \tag{3.4}$$

Here, G is a coefficient related to $\overline{\mu}_w$ and the shape of scattering phase function. Unfortunately, constraining the latter is so complicated as to make G extremely difficult to parameterize, especially when the sun is not directly overhead. Neither the *Gordon* [1989] nor the *Kirk* [1991] models account for the fact that scattering typically causes K_d to increase asymptotically with depth in most natural waters, which often causes them to overestimate $E_d(z)$ [*Mobley*, 1994].

More recently, *Mobley* [1994] summarize a two-flow model and presented a tantalizingly simple relationship between $K_d(z)$ and the IOPs:

$$K_d(z) = \frac{a + b_b}{\overline{\mu}_d(z)} - R(z)\frac{b_b}{\overline{\mu}_u(z)} \tag{3.5}$$

Here, $\overline{\mu}_d(z)$ and $\overline{\mu}_u(z)$ represent the average cosines of downward and upward plane irradiances at depth (z) respectively, and $R(z)$ [$= E_u(z)/E_d(z)$] is the plane irradiance reflectance at depth (z). The IOPs are assumed to be vertically homogeneous for simplicity. Since $R(z)$ is typically small in optically deep water, the second term $[R(z)\frac{b_b}{\overline{\mu}_u(z)}]$ is often ignored, leading to the common expression:

$$K_d(z) \approx \frac{a + b_b}{\overline{\mu}_d(z)} \tag{3.6}$$

Unfortunately, estimating $\overline{\mu}_d(z)$ is more difficult than $\overline{\mu}_w$ because it includes the angular distribution of sky radiance as diffracted by air-borne molecules and aerosols and water-borne molecules and particles, in addition to the direct solar beam. It is also explicitly variable with depth (z). This simple relationship offers a potential solution to relate the

vertical variation of $K_d(z)$ and $E_d(z)$ to the IOPs, but the vertical distribution of $\overline{\mu}_d(z)$ and the method to estimate it are not well established.

An asymptotic closure theory has been developed that describes the angular distribution of plane irradiance as a function of depth (z) [*Bannister*, 1992; *Berwald et al.*, 1995; *Lee et al.*, 2005; *Liu et al.*, 2004; *McCormick*, 1995; *Zaneveld*, 1989]. Based on this theory, the vertical distribution of $K_d(z)$ at relatively high solar position (e.g. $\theta_s = 0°$) can be expressed as:

$$K_d(\theta_s = 0°, z) = K_d(\infty) + [K_d(\theta_s = 0°, 0) - K_d(\infty)]\exp(-Pcz) \quad (3.7)$$

Here, the exponential slope (P) represents the vertical decay rate of $K_d(\theta_s=0°, z)$ towards its asymptotic value in infinitely deep water [$K_d(\infty)$] along with the beam optical depth ($\xi = cz$). However, *Hydrolight*® simulations showed that this asymptotic closure model becomes invalid when solar elevation is low (e.g. $\theta_s > 40°$). A more complicated model, such as a five-parameter asymptotic closure model expressed as the sum of two exponential functions [*McCormick*, 1995], can describe $K_d(z)$ more accurately, but explaining the derived parameters and estimating them from the IOPs and θ_s are extremely difficult.

This chapter developed a semi-analytic radiative transfer approach (named as PZ06_E_d) based on the analysis of *Hydrolight*® simulations, along with two-flow modeling and asymptotic closure theory to provide approximate solutions of $K_d(z)$ and $E_d(z)$ for various in-water and above-water conditions. The calculations were verified against *Hydrolight*® simulations and validated against field observations from the southern Chesapeake Bay. PZ06_E_d was also compared to the much simpler *Gordon* [1989] model, which has been widely applied to bio-optics in Case 1 situations.

3.2. Theory

Since the absolute value of $E_d(0^+)$ need not be specified (in fact, ocean color remote sensing is concerned with its relative value, e.g. remote sensing reflectance), it is considered known throughout the whole study. Therefore, the objective of this model will focus on the vertical distribution of the ratio of $E_d(z)/E_d(0^-)$, where $E_d(0^-)$ is assumed to obey a constant transmission factor across the air-sea interface as [*Harding et al.*, 2005]:

$$E_d(0^-) = 0.98E_d(0^+) \tag{3.8}$$

Equation (3.8) will not consider variation in air-sea transmission caused by surface waves and atmospheric cloud cover. This model is implicitly spectral although the symbolic term λ has been omitted from the equations for simplicity.

The incident downwelling plane irradiance (E_d) entering the water column is composed of two sources: the direct solar beam [$(E_d)_{\text{direct}}$] and the diffuse sky irradiance [$(E_d)_{\text{diffuse}}$] [*Gordon*, 1989; *Kirk*, 1994; *Mobley*, 1994]:

$$E_d = (E_d)_{direct} + (E_d)_{diffuse} \tag{3.9}$$

If the fraction of the direct solar beam is defined as f_{direct}, then the fraction of diffuse sky irradiance becomes $(1 - f_{direct})$.

The direct solar beam, $(E_d)_{\text{direct}}$, originating from the solar zenith angle (θ_s) is diffracted to θ_w by Snell's Law as it crosses the air-water interface [*Mobley*, 1994]. As with the *Gordon* [1989] model, the diffuse attenuation coefficient from the direct solar beam, $[K_d(z)]_{\text{direct}}$, is assumed to vary inversely with $\overline{\mu}_w$ as:

$$[K_d(z)]_{direct} \approx \frac{[K_d(\theta_w = 0°, z)]_{direct}}{\overline{\mu}_w} \tag{3.10}$$

Here, $[K_d(\theta_w=0°,z)]_{direct}$ represents the diffuse attenuation coefficient of $(E_d)_{direct}$ when the sun is directly overhead ($\theta_w = 0°$, $\cos\theta_w = 1$, $\overline{\mu}_w = 1$), and closely approximates ($a + b_b$) at the surface (see Eq. 3.6). $[K_d(\theta_w=0°,z)]_{direct}$ increases with depth as the direct solar beam is scattered by water molecules and suspended particles. Application of the asymptotic theory shown in Eq. (3.7) to describe the vertical distribution of $[K_d(\theta_w=0°,z)]_{direct}$ through integration, along with Eq. (3.10), creates the average diffuse attenuation coefficient from direct solar beam:

$$[\overline{K}_d(z)]_{direct} \approx \frac{1}{\overline{\mu}_w}\{K_d(\infty) + \frac{[a+b_b-K_d(\infty)]}{Pcz}[1-\exp(-Pcz)]\} \quad (3.11)$$

Thus, the relative vertical distribution of $(E_d)_{direct}$ is calculated as:

$$\frac{[E_d(z)]_{direct}}{E_d(0^-)} \approx f_{direct}\exp\{-\frac{K_d(\infty)\times z}{\overline{\mu}_w} - \frac{[a+b_b-K_d(\infty)]}{\overline{\mu}_w Pc}[1-\exp(-Pcz)]\} \quad (3.12)$$

The average cosine of the diffuse sky downwelling irradiance above the water, $[\overline{\mu}_d(0^+)]_{diffuse}$, is highly variable from 0.25 when the sun is nearly horizontal ($\theta_s = 89°$) to 0.54 when the sun is directly overhead ($\theta_s = 0°$) (Fig. 3.1). Snell's Law, however, constrains that the value below the water, $[\overline{\mu}_d(0^-)]_{diffuse}$, to 0.69 when $\theta_s = 89°$ and 0.78 when $\theta_s = 0°$ (Fig. 3.1). Exact radiative transfer modeling has shown that the asymptotic value of the average cosine of downwelling irradiance [$\overline{\mu}_d(\infty)$] in natural waters is relatively constant at about 0.7 [*Kirk*, 1994; *Mobley*, 1994]. Thus, the vertical variation of $[\overline{\mu}_d(z)]_{diffuse}$ is relatively small from ~ 0.78 to ~ 0.7, which in turn implies that the vertical variation of K_d for diffuse sky irradiance is also small, regardless the solar zenith angle (θ_s). Thus, it is reasonable to make the diffuse attenuation coefficient for diffuse

sky irradiance (K_{diffuse}) independent of depth and solar zenith angle (θ_s) when describing the vertical distribution of $[E_d(z)]_{\text{diffuse}}$:

$$\frac{[E_d(z)]_{diffuse}}{E_d(0^-)} = (1 - f_{direct})\exp(-K_{diffuse} z) \tag{3.13}$$

Combining Eqs (3.12) and (3.13) provides the basis to calculate the relative vertical distribution of $E_d(z)$:

$$\frac{E_d(z)}{E_d(0^-)} \approx f_{direct}\exp\{-\frac{K_d(\infty)\times z}{\overline{\mu}_w} - \frac{[a+b_b-K_d(\infty)]}{\overline{\mu}_w Pc}[1-\exp(-Pcz)]\} + (1-f_{direct})\exp(-K_{diffuse} z) \tag{3.14}$$

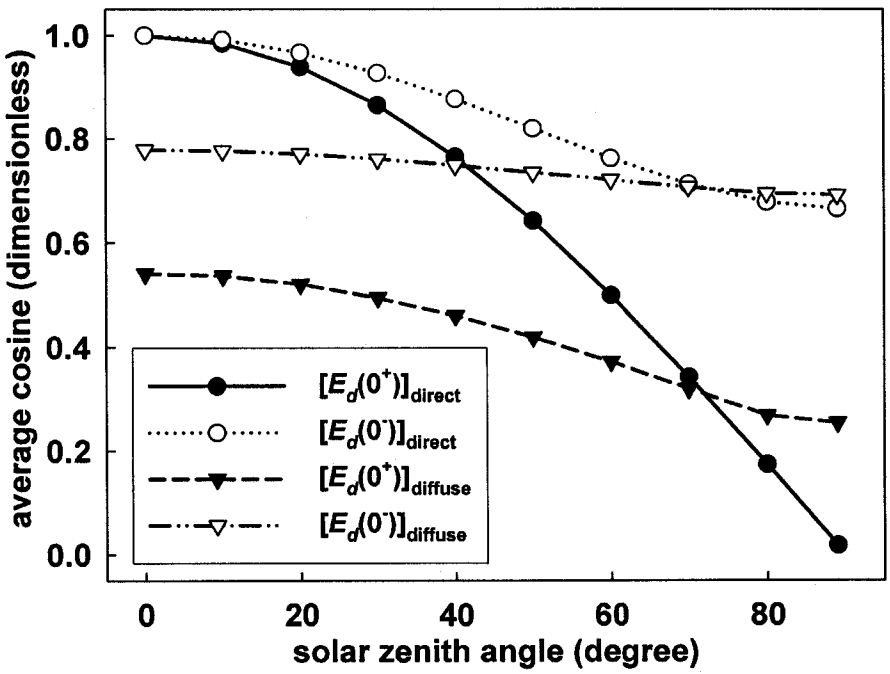

Figure 3.1. Variations of the average cosines of downwelling irradiance along with the solar zenith angle. $[E_d(0^+)]_{direct}$ and $[E_d(0^-)]_{direct}$: direct solar beam above and below the surface; $[E_d(0^+)]_{diffuse}$ and $[E_d(0^-)]_{diffuse}$: diffuse sky irradiance above and below the surface. Calculations were based on *Hydrolight*® simulations for clear sky.

The complete analysis of the vertical distribution of $E_d(z)$ from two-flow model theory requires the assessment of the contribution of upwelling irradiance [$E_u(z)$] to $E_d(z)$, which obviously increases the complexity of Eq. (3.14). Instead of adding second-order terms from $E_u(z)$ on $E_d(z)$, simulation results from the exact radiative transfer model (*Hydrolight*®), which have included the contribution from upwelling irradiance, were analyzed to generate an approximate model hereafter identified as PZ06_E_d.

3.3. Application

3.3.1. *Hydrolight*® simulations

Provided with the knowledge of IOPs (a, b, b_b, and c) and θ_s (also $\overline{\mu}_w$), the unparameterized variables in Eq.(3.14) include f_{direct}, $K_d(\infty)$, P, and $K_{diffuse}$. *Hydrolight*® v4.2 was used here to derive the relationships between these parameters and measurable or derivable water and atmospheric properties (e.g. a, b, c, b_b, θ_s, cloud coverage, and so on). The default models and the input parameters used to calculate the atmospheric and water conditions are provided in Table 3.1. Values for the unparameterized variables in Eq. (3.14) were derived from *Hydrolight*® simulation results using single scattering albedos ($\omega_0 = b/c$) ranging from 0.1 to 0.9 in 0.1 intervals and various scattering phase functions including *Petzold*'s [1972] average (b_b/b = 0.01833) and the Fournier-Forand function (b_b/b = 0.005 to 0.5) [*Mobley et al.*, 2002].

A special set of runs were calculated with θ_s = 89° (near horizontally), under which $(E_d)_{\text{direct}}$ approached zero. Thus, K_{diffuse}, which is almost independent of depth and θ_s, was directly calculated from the simulated results of $E_d(z)$ at θ_s = 89° by the non-linear least square match method of TableCurve 2D v5.01 (SYSTAT Software Inc.). The water

column beneath the euphotic zone, defined as $E_d(z) < 1\%$ of $E_d(0^-)$, was not considered in these simulations.

Table 3.1. Default models and the inputs for *Hydrolight*® runs

Quality	Range or Models
Atmospheric conditions	
Sky model (RADTRAN)	*Gregg and Carder* [1990] and *Harrison and Coombes* [1988]
Atmospheric pressure	1.013×10^5 Pa
Horizontal visibility	15 km
Relative humidity	80%
Precipitable water content	2.5 cm
Total ozone concentration	300 Dobson
Wind speed (WS)	5 m s^{-1}
Solar zenith angle (θ_s)	0, 10, 20, 30, 40, 50, 60, 70, 89°
Wavelength (λ)	350 – 700 nm in 5 nm intervals
Air-mass type	Marine
Cloud coverage	0, 5, 10, 15, 20, 25, 30, 40, 60, 80, 100%
Water conditions (vertically homogeneous)	
(1). Single scattering albedo (ω_0)	0.1 – 0.9, in 0.1 intervals
Backscattering ratio (b_b/b)	0.005, 0.01, 0.014, 0.01833, 0.02, 0.025, 0.03, 0.035, 0.04, 0.045, 0.05, 0.06, 0.08, 0.1, 0.15, 0.2, 0.3, 0.4, 0.5
Scattering phase function	*Petzold* [1972] and Fourier-Forand function [*Mobley et al.*, 2002]
(2) *Hydrolight*® default classic Case 1 IOP model	
Water absorption (a_w)	*Pope and Fry* [1997]
[Chl]	0, 0.01, 0.03, 0.1, 0.3, 1, 3, 10 mg m^{-3}
Particulate absorption (a_p)	*Prieur and Sathyendranath* [1981]
CDOM absorption (a_g)	*Morel and Gentili* [1991]
Scattering by pure seawater (b_w)	*Smith and Baker* [1981]
Particulate scattering (b_p)	*Gordon and Morel* [1983]
Backscattering ratio (b_{bp}/b_p)	0.01833
Scattering phase function	*Petzold* [1972]

Parameterizations of f_{direct} and $K_d(\infty)$ were calculated directly by *Hydrolight*®. $K_d(\infty)$ depends only on water IOPs, while f_{direct} varies only with the above conditions (here θ_s and cloud coverage). $[E_d(z)]_{\text{direct}}$ was calculated from Eq. (3.14) by subtracting the fraction of the diffuse source. The exponential slope (P) was calculated from Eq.

(3.11) by non-linear least square method from TableCurve 2D v5.01 (SYSTAT Software Inc.).

PZ06_E_d was also compared to *Hydrolight*® simulations and the *Gordon* [1989] model using typical Case 1 IOP conditions (Table 3.1). Fidelity to *Hydrolight*® simulations of PZ06_E_d or the *Gordon* [1989] model were evaluated by calculating the percent root-mean-square (RMS) difference between their results:

$$RMS = \sqrt{\frac{1}{n}\sum(\frac{PZ06\_E_d}{Hydrolight} - 1)^2} \times 100\% \quad (3.15)$$

3.3.2. Field observations

Bio-optical observations made in the southern Chesapeake Bay on May 18th, 2005 (CLT-T cruise, Table 2.1 and Fig. 2.1) were used to validate the prediction of PZ06_E_d. The bio-optical characteristics of this region are described in Chapter 2. The selected stations were located near Cape Henry (Station 2; 75.88° W, 36.91° N) and ~ 6.5 km east of the Chesapeake Light Tower (Station 6; 75.64° W, 36.92° N). Profiles of $E_d(z)$ were collected with a HyperPro II hyperspectral radiometric system (Satlantic, Inc.) at 5 nm intervals from 350 to 800 nm. Vertical profiles of absorption (a) and beam attenuation (c) were measured with an *ac*-9 spectrophotometer (WET Labs, Inc.). Backscattering (b_b) profiles were measured with a Hydroscat-6 (HOBI Labs, Inc.). All measurements were averaged to 0.5 m depth bins except the HyperPro radiometer for which the records at the exact depth points were used. To remove uncertain boundary effects caused by high turbidity close to the sea floor or by touching the sea floor with some instruments, all measurements used in this chapter were at least 3 m above the sea floor. All data below the euphotic zone, where $E_d(z)/E_d(0^-) < 1$, were excluded. Both stations were optically

deep as < 10% of $E_d(0^-)$ reached the sea floor, even though their geometric bottom depths were 10 m and 21 m for Stations 2 and 6, respectively. Station 2 was more estuarine in character (surface salinity ≈ 22 psu, Fig. 3.2a) and more turbid ([Chl] = 4.5 and 1.6 mg m^{-3} at surface and bottom; $c(440)$ up to 3 m^{-1}, Fig. 3.2b). Station 6 was more marine in character (surface salinity ≈ 28 psu, Fig. 3.3a) and less turbid ([Chl] = 0.8, 0.5, and 0.9 mg m^{-3} at surface, middle, and bottom; $c(440)$ < 1.2 m^{-1}, Fig. 3.3b). The solar zenith angles (θ_s) of Stations 2 and 6 calculated from *Hydrolight*® simulations based on local date, time, longitude, and latitude were 40.9° and 23.1°, respectively. Five common wavelengths (440, 488, 510, 555, and 676 nm) measured by the *ac*-9 and Hydroscat-6 spanning almost the entire range of photosynthetically active radiation (PAR = 400 to 700 nm) were selected for analysis. As before, model performance was evaluated by the percent root-mean-square (RMS) error.

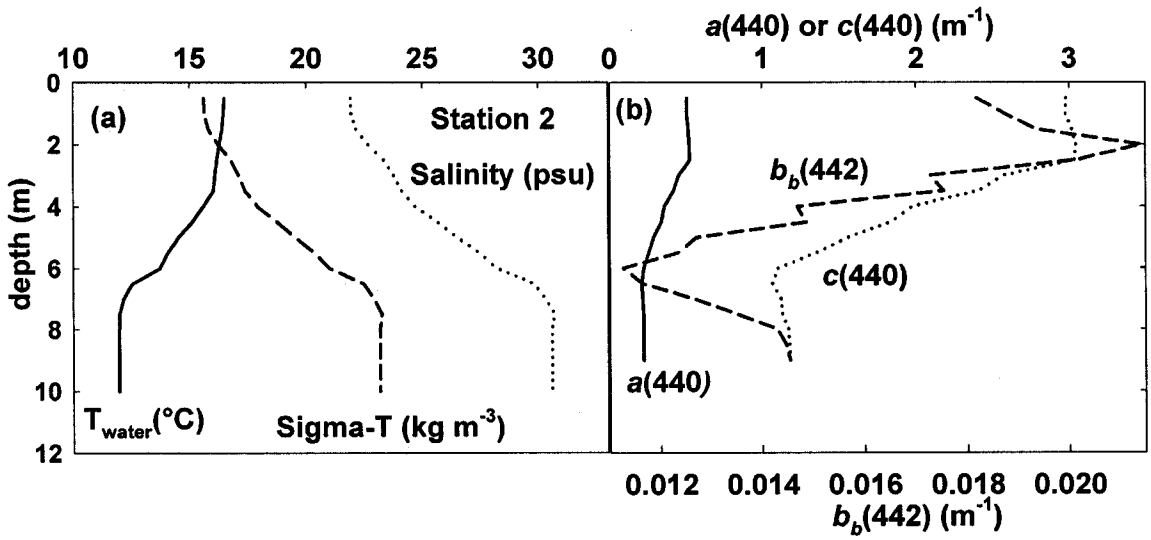

Figure 3.2. Vertical conditions of Station 2. (a) Hydrographic properties. (b) IOPs.

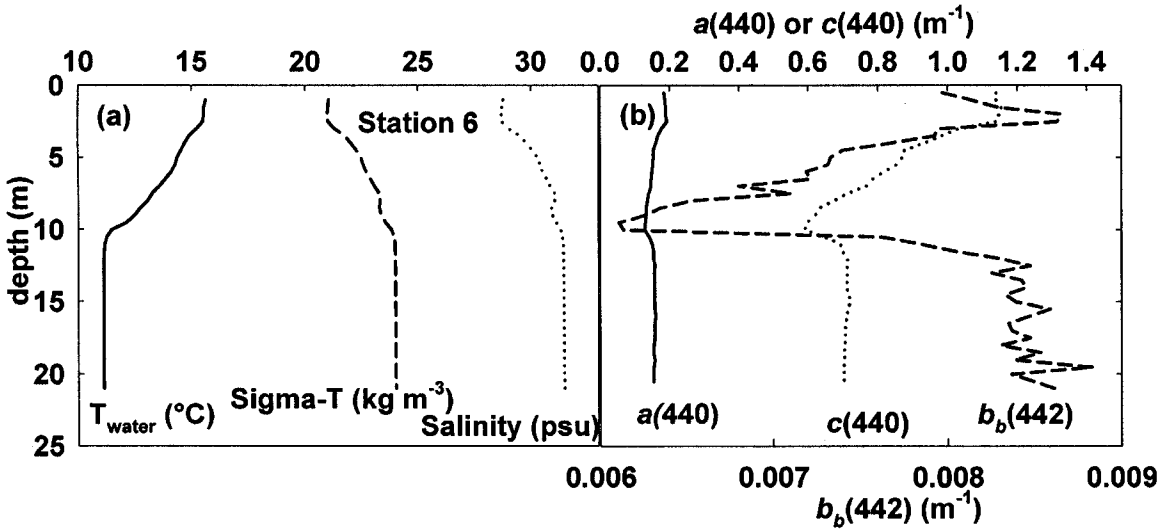

Figure 3.3. Vertical conditions of Station 6. (a) Hydrographic properties. (b) IOPs.

3.3.3. SeaWiFS imagery

SeaWiFS products retrieved from the modified GSM01 semi-analytic inverse model (GSM01-CLT), including the absorption of CDOM plus non-pigmented particles (a_{dg}), particulate backscattering (b_{bp}), and chlorophyll *a* concentration ([Chl]) and therefore phytoplankton absorption (a_{ph}), were used to calculate IOPs of absorption (a) and backscattering (b_b). Particulate scattering (b_p) was estimated from b_{bp} by adopting a constant particulate backscattering ratio (b_{bp}/b_p) of 0.0184 (Chapter 2). Again, the selected date was June 2nd, 2003, a relatively clear day. PZ06_E_d was used to calculate the average K_d(490) from the surface to one beam optical depth ($\xi = cz$), which provides most of the water-leaving radiance (L_w) to the remote sensing detector [*Kirk*, 1994; *Mobley*, 1994]. The diffuse attenuation coefficient at 490 (K_{490}_Muller) from the derived empirical equation based on the ratio of three bands of L_w [*Mueller*, 2000] was processed from the SeaWiFS Data Analysis System (SeaDAS v4.7) software. Solar zenith angle (θ_s) information was derived from the SeaDAS processing, too. The digital elevation map for

the lower Middle Atlantic Bight (one minute grid resolution) was obtained from National Oceanic and Atmospheric Administration (NOAA) General Bathymetric Chart of the Oceans (GEBCO) (http://www.ngdc.noaa.gov/mgg/gebco). The fraction of $E_d(0^-)$ reaching the sea floor was then calculated by PZ06_E_d.

3.4. Results

3.4.1 The derived coefficients

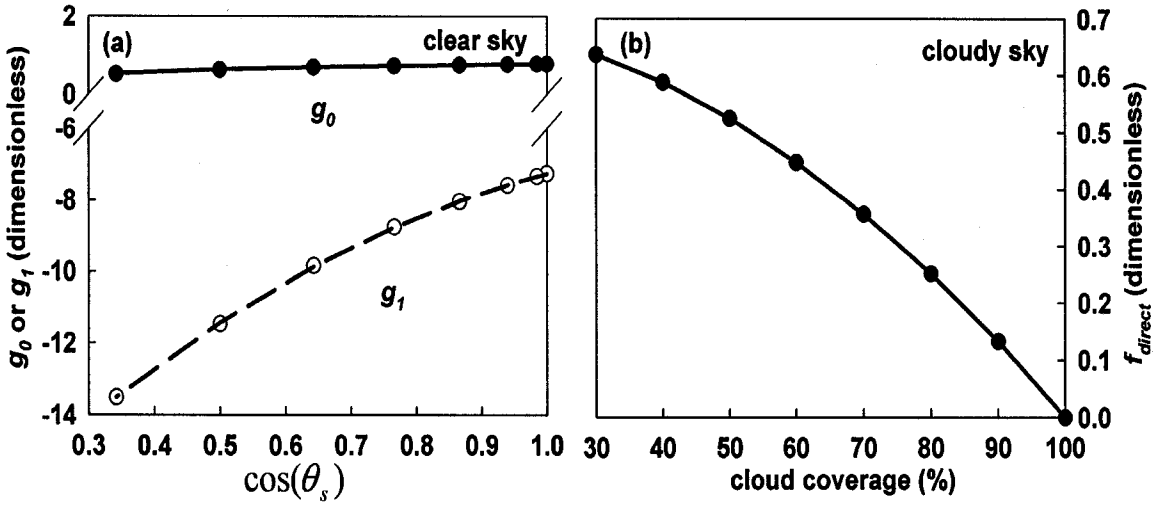

Figure 3.4. Variation of the fraction of direct solar irradiance. (a) The relationships between the derived coefficients (g_0 and g_1) and solar zenith angle (θ_s) at clear sky condition. (b) The fraction of direct solar beam, f_{direct}, as a function of cloud coverage. Data points are connected by regression lines.

The fraction of direct solar irradiance, f_{direct}—For clear sky conditions (e.g. cloud coverage < 30%), f_{direct} was described by an exponential function ($r^2 > 0.99$):

$$f_{direct}(\lambda; clear) = g_0 + g_1 \exp(-0.01\lambda) \quad (3.16)$$

where g_0 and g_1 were significantly ($r^2 > 0.99$) related to the solar zenith angle (θ_s) (Fig. 3.4a):

$$g_0 = 1.147 - 0.363(\cos\theta_s)^{-0.5} \tag{3.17}$$

$$g_1 = -19.25(1-\cos\theta_s) - 7.26(\cos\theta_s)^2 \tag{3.18}$$

When cloud coverage was over 30%, f_{direct} became independent of wavelength (λ) and θ_s, but was significantly ($r^2 > 0.99$) related to the cloud coverage (Fig. 3.4b):

$$f_{direct}(cloudy) = 0.7 \times (1 - \%cloud^2) \tag{3.19}$$

The asymptotic diffuse attenuation coefficient, $K_d(\infty)$—$K_d(\infty)$ was described by a polynomial function ($r^2 > 0.99$ except when $b_b/b > 0.3$ in which $r^2 > 0.97$):

$$K_d(\infty) = (1 - D_0\omega_0 - D_1{\omega_0}^2) \times c \tag{3.20}$$

where D_0 and D_1 were significantly ($r^2 > 0.99$) related to the backscattering ratio (b_b/b) (Fig. 3.5):

$$D_0 = 0.959 - 2.346\sqrt{\frac{b_b}{b}} + 0.747\frac{b_b}{b} \tag{3.21}$$

$$D_1 = 0.046 + 1.807\sqrt{\frac{b_b}{b}} - 0.888\frac{b_b}{b} \tag{3.22}$$

The diffuse attenuation coefficient of the diffuse incident beam, $K_{diffuse}$—Similar to $K_d(\infty)$, $K_{diffuse}$ was described by another polynomial function ($r^2 > 0.99$):

$$K_{diffuse} = (1.317 - A_0\omega_0 - A_1{\omega_0}^2) \times c \tag{3.23}$$

where A_0 and A_1 were significantly ($r^2 > 0.99$, $P < 0.001$) related to the backscattering ratio (b_b/b) (Fig. 3.6):

$$A_0 = 1.399 - 1.012\sqrt{\frac{b_b}{b}} - 0.939\frac{b_b}{b} \tag{3.24}$$

$$A_1 = -0.047 + 0.244\sqrt{\frac{b_b}{b}} + 1.120\frac{b_b}{b} \tag{3.25}$$

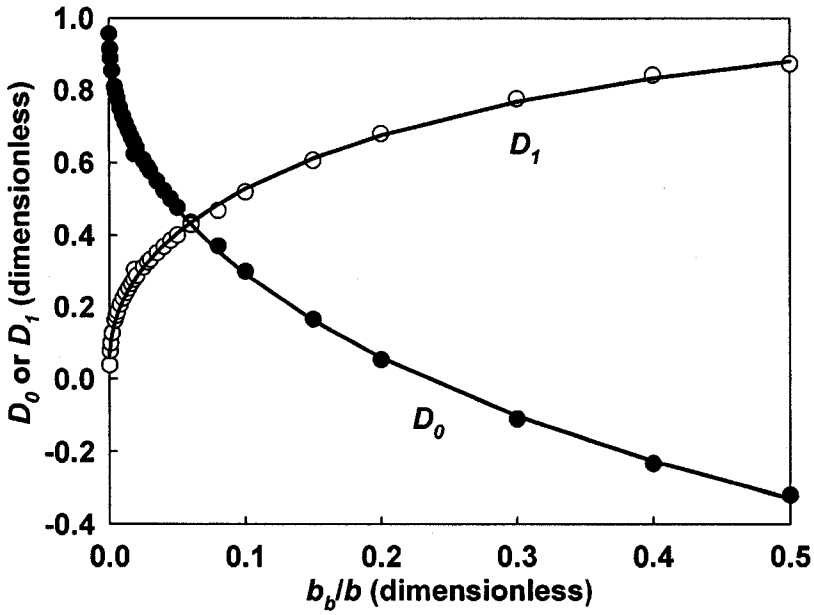

Figure 3.5. Variation of the derived coefficients (D_0 and D_1). D_0 and D_1 described the asymptotic diffuse attenuation coefficient [$K_d(\infty)$] as functions of the backscattering ratio (b_b/b). Data points are connected by regression lines.

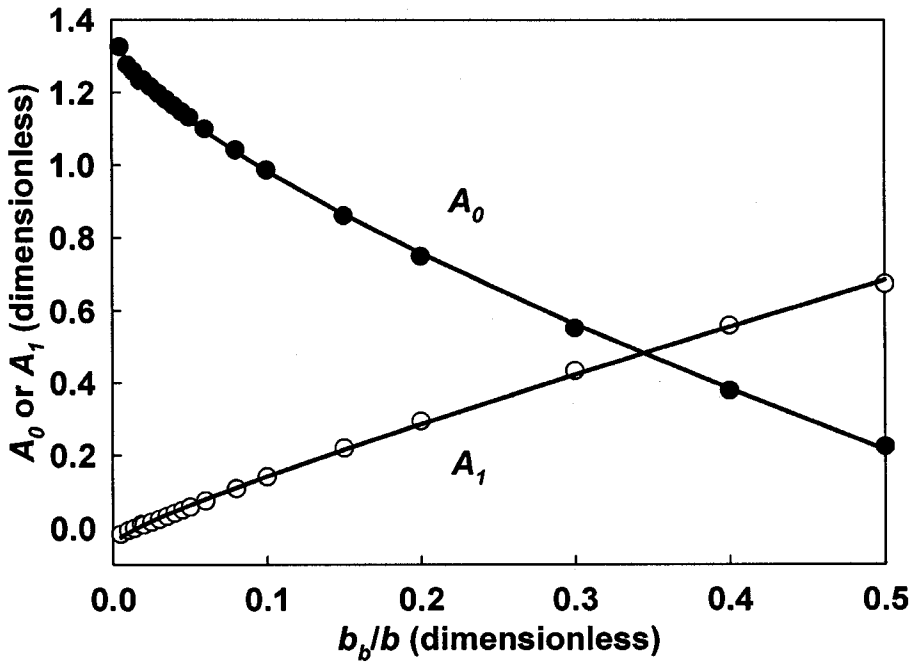

Figure 3.6. Variation of the derived coefficients (A_0 and A_1). A_0 and A_1 described the diffuse attenuation coefficient for sky diffuse downwelling plane irradiance ($K_{diffuse}$) as functions of the backscattering ratio (b_b/b). Data points are connected by regression lines.

The exponential slope (P) of K_d for the direct solar beam—The exponential slope (P) describing the vertical variation of $K_d(\theta_w=0°, z)$ was significantly ($r^2 > 0.95$, $P < 0.001$) related to the backscattering ratio (b_b/b):

$$P = B_0 + B_1 \times \sqrt{\frac{b_b}{b}} \tag{3.26}$$

where the coefficients B_0 and B_1 were significantly ($r^2 > 0.99$, $P < 0.001$) related to the single scattering albedo (ω_0) (Fig. 3.7):

$$B_0 = 0.817 - 0.877\sqrt{\omega_0} \tag{3.27}$$

$$B_1 = 0.193 + 0.421\omega_0 + 0.741\omega_0^2 \tag{3.28}$$

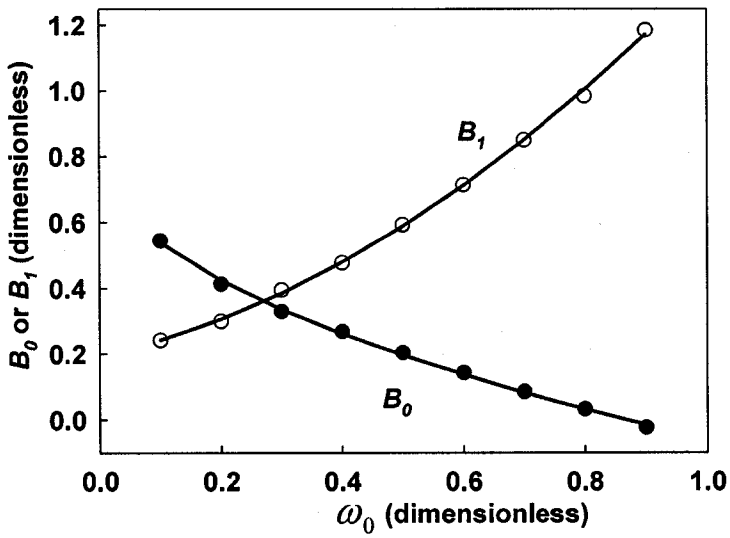

Figure 3.7. Variation of the derived coefficients (B_0 and B_1). B_0 and B_1 described the P coefficient as functions of the single scattering albedo (ω_0). Data points are connected by regression lines.

3.4.2. Verification against *Hydrolight*® simulations

The parameter values derived from *Hydrolight*® simulations were applied to Eq. (3.14) to calculate $E_d(z)/E_d(0^-)$. In general, PZ06_E_d yielded estimates that were with 2 to

4% RMS errors of the *Hydrolight*® simulations for a wide range of [Chl] and solar zenith angles (θ_s) (Fig. 3.8a). Model accuracy decreased as the water column optical density increased (e.g. more particles and [Chl]) (Fig. 3.8a). There was no consistent relationship with solar zenith angle (Fig. 3.8a). The *Gordon* [1989] model predicted $E_d(z)/E_d(0^-)$ with an RMS accuracy just below 10% for clearer waters (e.g. [Chl] < 1 mg m^{-3}), and rose to nearly 80% as optical density increased (e.g. [Chl] = 10 mg m^{-3}) (Fig. 3.8b). Under particle-rich conditions, the *Gordon* [1989] model performed better at higher solar zenith angle (Fig. 3.8b) because increasing θ_s increased the fraction of the diffuse incident solar beam whose diffuse attenuation coefficient ($K_{diffuse}$) was less sensitive to the depth, as assumed by the simple *Gordon* [1989] model.

3.4.3. Validation against field observations

Field observations of the vertical distributions of $E_d(z)/E_d(0^-)$ measured by the HyperPro radiometer were used to validate PZ06_E_d (Figs. 3.9 and 3.10). Both *Hydrolight*® and PZ06_E_d reproduced the field observations better than the *Gordon* [1989] model, based on RMS calculations at both Station 2 (Figs. 3.9a-b) and Station 6 (Figs. 3.10a-b). After considering the relative difference between the HyperPro profiles (e.g. 5% and 6% of standard deviation at 676 nm for 3 profiles in Stations 2 and 4 profiles in Station 6), and the relative error caused by the sampling processes (e.g. HyperPro was at least 20 m away from the ship while *ac*-9 and HS-6 were profiled just beside the ship), the RMS error of 10 to 15% may be reasonable. RMS errors between PZ06_E_d and *Hydrolight*® simulations were 6.4% and 2.8% for Station 2 and Station 6, respectively (Fig. 3.9d and Fig. 3.10d). The RMS errors from the *Gordon* [1989] model were 33.4% at Station 2 (Fig. 3.9c) and 40.3% at Station 6 (Fig. 3.10c).

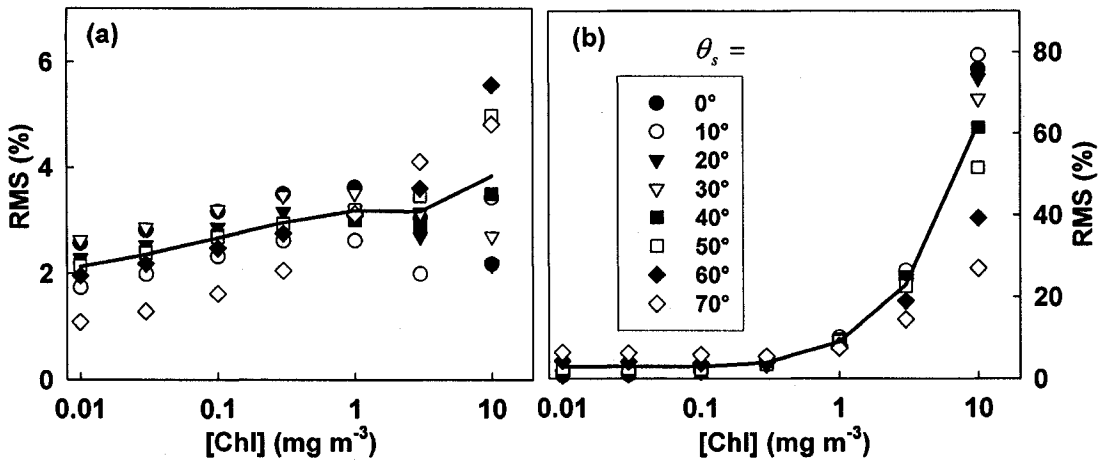

Figure 3.8. The percent root-mean-square (RMS) error of $E_d(z)/E_d(0^-)$ against *Hydrolight*® simulations. (a) PZ06_E_d. (b) The *Gordon* [1989] model. Solar zenith angle (θ_s): 0 to 70°. Water IOPs were Case 1 with [Chl] = 0 to 10 mg m^{-3} for a 10 m water column. Wavelength: 350 to 650 nm in 5 nm intervals. Solid lines: average RMS error for all solar zenith angles and all wavelengths.

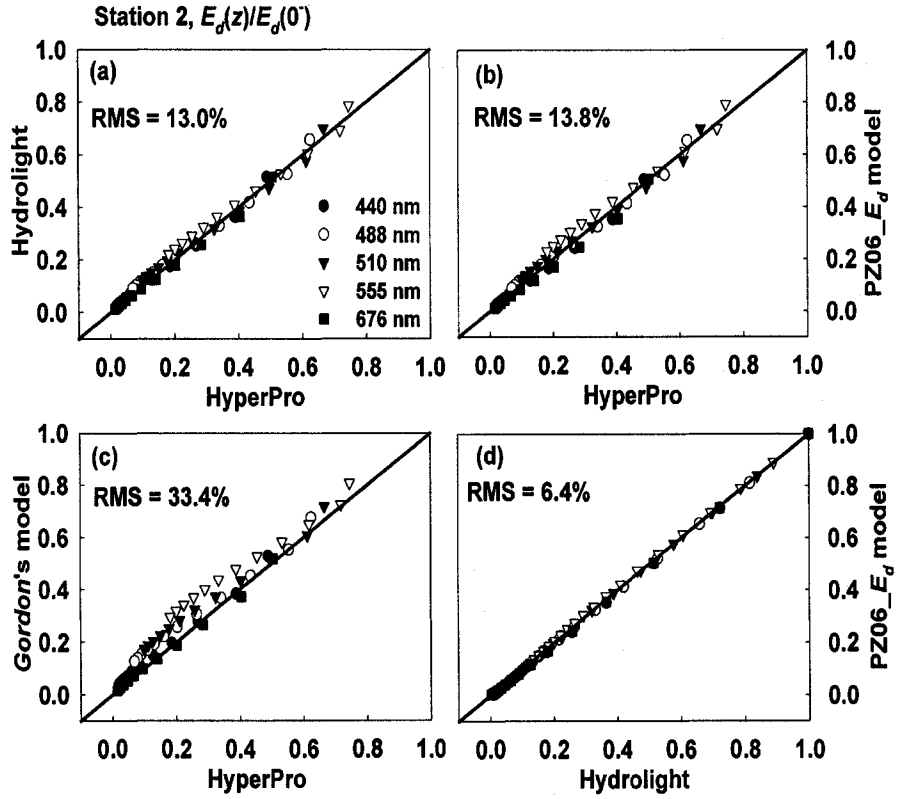

Figure 3.9. Comparisons of $E_d(z)/E_d(0^-)$ for Station 2. Plots (a) – (c) were HyperPro observation compared with (a) *Hydrolight*®, (b) PZ06_E_d, and (c) the *Gordon* [1989] model. (d) Comparison between *Hydrolight*® simulations and PZ06_E_d.

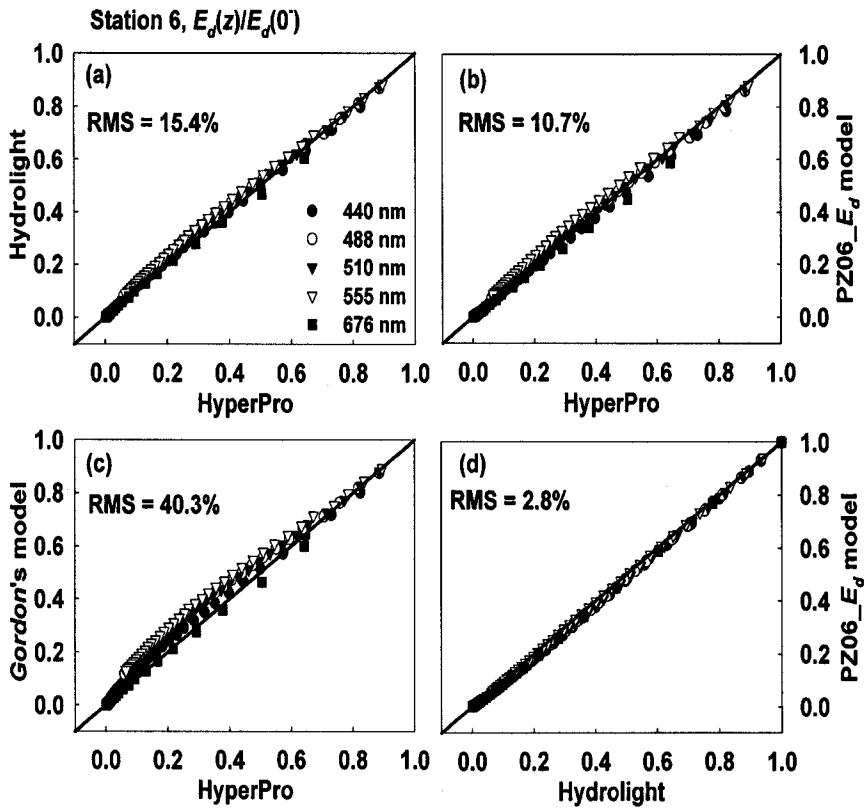

Figure 3.10. Comparisons of $E_d(z)/E_d(0^-)$ for Station 6. Plots (a) – (c) were HyperPro observation compared with (a) *Hydrolight*®, (b) PZ06_E_d, and (c) the *Gordon* [1989] model. (d) Comparison between *Hydrolight*® simulations and PZ06_E_d.

3.4.4. The spatial distribution of K_d derived from SeaWiFS imagery

Figure 3.11a shows an example of SeaWiFS image of $K_d(490)$ calculated from PZ06_E_d based on the retrieved IOP products by GSM01-CLT (Chapter 2). This map shows $K_d(490)$ to decrease from the Chesapeake Bay mouth out toward the Atlantic Ocean (Fig. 3.11a). Due to the Coriolis effect, the southern area outside of the Chesapeake Bay mouth is more turbid than the northern area (Fig. 3.11a). The primary frontal zone along Virginia/Carolina coast [*Sletten et al.*, 1999] and the mixing of clear Gulf Stream waters with relatively turbid local waters are also clearly shown (Fig. 3.11a). The derived values $K_d(490)$ for this image are also reasonable, except for the inside area

of the Chesapeake Bay where GSM01-CLT failed to accurately retrieve the IOPs (Chapter 2). The field measurements conducted on a similar season (May 18th, 2005) showed surface $K_d(490)$ decreasing from ~ 0.5 m^{-1} at near Cape Henry to ~ 0.15 m^{-1} at the east of the Chesapeake Bay, similar to the values displayed in Fig. 3.11a. The values calculated from the water-leaving (L_w) band ratio by an empirical equation [*Mueller*, 2000] overestimated K_{490} (e.g. > 0.1 m^{-1} for the open seas), and could not clearly define the frontal zone (Fig. 3.11b). The significant overestimation (e.g. 20 – 30%) of K_{490} by the *Mueller* [2000] empirical equation for clear water has been observed previously (http://oceancolor.gsfc.nasa.gov/REPROCESSING/SeaWiFS/R5.1/k490_update.html). Meanwhile, the empirical equation does not perform well in water masses where K_{490} > 0.25 m^{-1} [*Mueller*, 2000], which limits its application in coastal waters.

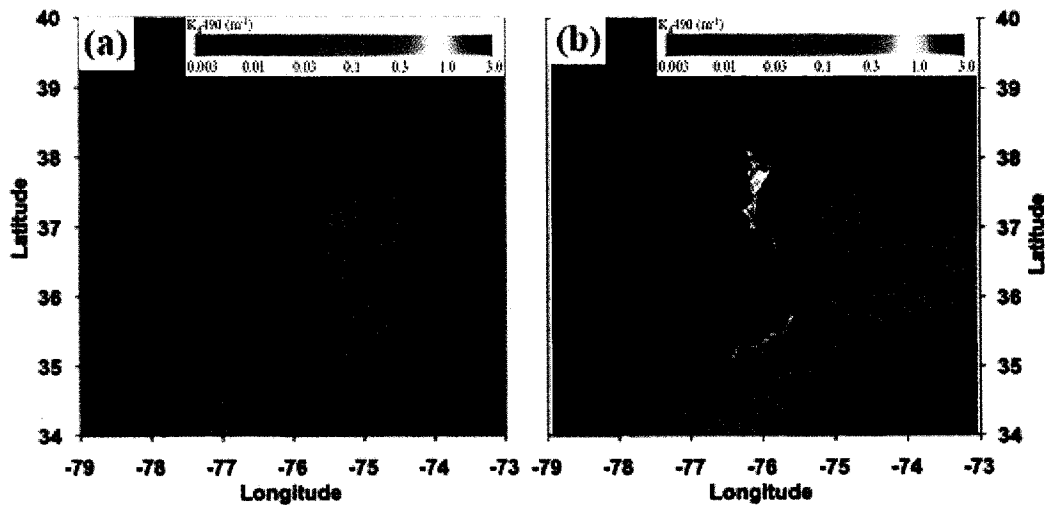

Figure 3.11. SeaWiFS spatial distribution of $K_d(490)$. The data were derived from (a) PZ06_E_d, and (b) the *Mueller* [2000] model, for lower Middle Atlantic Bight. The selected clear date was June 2nd, 2003. Circle symbol: the Chesapeake Light Tower (CLT).

Since K_d determines the depth distribution of light, it can be used to assess whether or not the coastal region is optically shallow. Many sites in the southern Chesapeake Bay are shallower than 20 m (Fig. 3.12a). When the water column is relatively clear (e.g. K_d < 0.1 m^{-1}), about 10 – 30% of $E_d(0^-)$ is expected to reach the bottom (Fig. 3.12b). For this selected image, it is estimated that > 60% of estuarine area (e.g. the maximum depth < 200 m) is defined as optically shallow at 490 nm (Fig. 3.12b). The water leaving radiance (L_w) in these areas are likely to be significantly affected by bottom reflectance (Chapter 4).

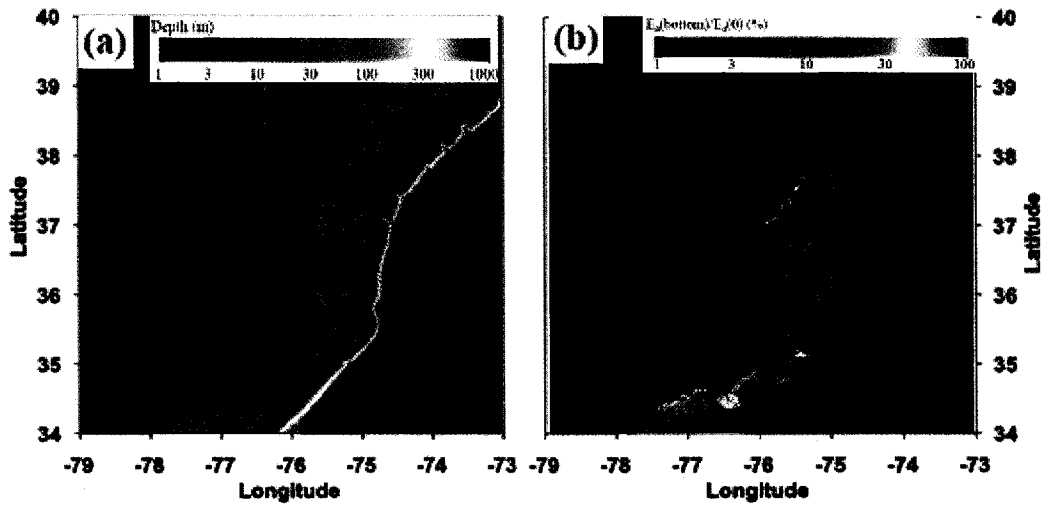

Figure 3.12. Bathymetric condition and light penetration through water column. (a) The bathymetric condition of lower Middle Atlantic Bight. (b) The SeaWiFS spatial distribution of the fraction of downwelling irradiance at 490 nm reaching the sea floor [$E_d(490)/E_d(0^-)$] calculated from PZ06_E_d. Circle symbol: the Chesapeake Light Tower (CLT).

3.5. Discussion

The Monte Carlo approach, an exact radiative transfer method (RTM), computes the radiometric quantities (e.g. L_w and R_{rs}) by statistically assessing the individual simulation from large numbers of randomly oriented photons [*Mobley*, 1994]. Monte

Carlo models suffer from statistical noise, and the radiometric quantities are not computed in equal accuracy (e.g. more statistical noise for radiance than irradiance since simulated photons must be partitioned into more directions in calculating radiance quantity) [*Mobley*, 1994]. *Hydrolight*®, based on the invariant imbedding theory by using Riccati Matrix equations, computes all radiometric quantities in equal accuracy without statistical noise in the results [*Mobley*, 1994]. Both of the exact RTMs provide good enough results in simulating above or in-water radiometric quantities by providing the knowledge like medium characteristics (e.g. IOPs). However, the complex processes in simulating the radiometric quantities limit the ability of these exact RTMs to be inverted for solution of IOPs and biogeochemical properties (e.g. [Chl]).

PZ06_E_d, based on the division of the incident solar beam into direct solar beam and the diffuse sky beam and the separate analyses of their vertical characteristics along with the water depth, appears very successful in reproducing both results of *Hydrolight*® simulations and field observations in describing the vertical distribution of downwelling plane irradiance [$E_d(z)$]. However, an accurate estimate of the amount of diffuse sky irradiance scattered by the atmospheric aerosol is required for this approach. Parameterization of PZ06_E_d was totally based on the simulation results of *Hydrolight*®, from which a globally tuned sky model [*Gregg and Carder*, 1990] was applied. The aerosol of coastal areas, however, is more complicated than that in open seas. In general, it is reasonable to think that aerosol concentration in coastal areas is higher than that predicted by *Hydrolight*® simulations for defaulted marine airmass type. In the other words, the "real" f_{direct} value in coastal areas is typically lower than that simulated here by *Hydrolight*®. Since the average cosine ($\overline{\mu}_d$) of the direct solar beam is typically (e.g. for

$\theta_s < 70°$) larger than that of the diffuse sky irradiance (Fig. 3.1), which generally means lower diffuse attenuation coefficient (K_d) for the former, the vertical distribution of $[E_d(z)]_{direct}$ decays more slowly than $[E_d(z)]_{diffuse}$. Therefore, *Hydrolight*® simulations or PZ06_E_d based on the analysis of *Hydrolight*® simulations probably slightly overestimate the vertical distribution of $E_d(z)/E_d(0^-)$ in coastal waters (Figs 3.9a-b and 3.10a-b).

PZ06_E_d presented in this chapter assumes the water is optically deep. When the water column is optically shallow, the upwelling irradiance (E_u) originating from bottom reflectance and its second-order contribution to $E_d(z)$ need to be assessed. Although such a contribution is relatively small (usually < 1% based on *Hydrolight*® simulations), it is not negligible in some extreme conditions (e.g. very bright floor and very strong backscattering coefficient of the Bahamas Banks; Fig. 1.1) in which > 10% may be contributed from bottom reflectance, especially near the sea floor. In the southern Chesapeake Bay coastal waters, in which the bottom reflectance is relatively low (e.g. in general $R_b < 0.1$), the second-order contribution from the bottom reflectance on $E_d(z)$ is reasonably ignored. Thus, PZ06_E_d can be applied to photosynthetic models for estimating water-column primary productivity [*Behrenfeld et al.*, 2005] and benthic optical environment from which seagrass primary productivity and distribution can be estimated [*Dierssen et al.*, 2003; *Zimmerman*, 2006].

CHAPTER 4

FORWARD MODELING OF REMOTE SENSING REFLECTANCE AND ITS INVERSION TO RETRIEVE THE INHERENT OPTICAL PROPERTIES

4.1. Background

Ocean color images, provided from space (e.g. SeaWiFS and MODIS), are useful for investigating the spatial and seasonal distribution of water quantity and biogeochemical process in the ocean (e.g. phytoplankton biomass, primary production, colored dissolved organic matter, and sediment concentration) [*Garver & Siegel*, 1997; *IOCCG*, 1999, 2000; *Kirk*, 1994; *Maritorena et al.*, 2002; *Mobley*, 1994; *O'Reilly et al.*, 1998, 2000]. The spectral characteristics of ocean color images are often expressed by the remote sensing reflectance (R_{rs}), which is defined as the ratio of water-leaving radiance (L_w) at the viewing zenith angle (θ_v) and azimuth angle (ϕ) to downwelling plane irradiance (E_d) just above the sea surface ($z = 0^+$) [*Mobley*, 1994]:

$$R_{rs}(\theta,\phi,\lambda) = \frac{L_w(\theta_v,\phi,\lambda)}{E_d(z=0^+,\lambda)} \tag{4.1}$$

Algorithms for retrieving chlorophyll *a* concentration ([Chl]) from satellite ocean color data in oceanic Case 1 waters routinely produce images with accuracy within the NASA mission target of ±35% of the *in situ* observation [*Garver & Siegel*, 1997; *O'Reilly et al.*, 1998, 2000]. Since phytoplankton often dominate the bio-optical characteristics in open oceans (Case 1 waters), R_{rs} can be related to [Chl] through empirical algorithms based on band ratios (e.g. OC4V4 and OC3M) [*Garver & Siegel*, 1997; *Kirk*, 1994; *Maritorena et al.*, 2002; *Mobley*, 1994; *O'Reilly et al.*, 1998, 2000].

Coastal Case 2 waters, however, have been shown to be much more complicated in terms of retrieving [Chl] from R_{rs}, since CDOM and suspended particles do not co-vary robustly with [Chl] [*Albert and Gege*, 2006; *Chang et al.*, 2003; *Harding et al.*, 2005; *Lee et al.*, 1998, 1999]. In addition, many coastal sites (e.g. Bahamas Banks and the southern Chesapeake Bay coastal waters) are shallow enough that light reflection from the sea floor contributes significantly to the water-leaving radiance (L_w) and remote sensing reflectance (R_{rs}) [*Dierssen et al.*, 2003; *Maritorena et al.*, 1994; *Werdell and Roesler*, 2003; *Wittlinger*, 2002; *Zaneveld and Boss*, 2003; *Zimmerman*, 2003, 2006].

Provided with the in-water IOPs and above-water atmospheric and solar conditions, exact radiative transfer models (RTMs) such as *Hydrolight*® provide state-of-the-art estimates of the photon distribution above and beneath the water, which results in the water-leaving radiance (L_w) and remote sensing reflectance (R_{rs}). However, exact-solution RTMs cannot be inverted to calculate the water IOPs from R_{rs}. Consequently, *Mobley et al.* [2005] developed a spectrum-matching look-up-table (LUT) to retrieve IOPs for ocean color images of R_{rs} spectra. This method required the complete evaluation of various water conditions. However, the limited spectra of bottom reflectance and regionally specific IOP characteristics in coastal waters often limit the LUT approach. Moreover, it can be different, if not impossible, to eliminate multiple non-unique matches to specific R_{rs} spectra.

Rather than a single regression of band ratios against biogeochemical properties (e.g. [Chl]; *O'Reilly et al.*, 1998, 2000), the inverse semi-analytic (SA) model (e.g. GSM01 model) assumes that R_{rs} can be directly related to inherent optical properties (IOPs) of backscattering (b_b) and absorption (a) in optically deep water that is readily

amendable to inversion and solution for the IOPs [*Gordon et al.*, 1988; *Garver & Siegel*, 1997; *Maritorena et al.*, 2002]:

$$(R_{rs})_{deep} \approx T \times \sum_{i=1}^{2} l_i \left(\frac{b_b}{b_b + a}\right)^2 \tag{4.2}$$

Here, T accounts for the upward transmittance of radiance (L_u) across the sea-air interface, and is relatively constant (0.54) for natural waters [*Mobley*, 1999]. *Gordon et al.* [1988] derived the coefficients $l_1 = 0.0949$ and $l_2 = 0.0794$ from the analyses for oceanic Case 1 water with relatively low particle loads. We do not know, however, if the coefficients (l_1 and l_2) derived by *Gordon et al.* [1988] are valid for high particle conditions typified by Case 2 coastal and inland waters. We also do not know how Eq. (4.2) varies with the solar position as R_{rs} is an AOP which depends on light structure in addition to IOPs. Furthermore, Eq. (4.2) excludes the contribution of bottom reflectance to L_w in optically shallow waters, which occurs commonly in coastal environments.

In this study, a semi-analytical model (PZ06_R_{rs}) based on the analysis of *Hydrolight*® simulation results was developed to link the remote sensing reflectance (R_{rs}) and IOPs, that would be valid for various water conditions from low to high particulate load, and for various topography conditions from optically deep to optically shallow waters. The purpose of this chapter was to assess the validity of such an inverse approach in retrieving three important biogeochemical parameters, [Chl], absorption by CDOM plus detritus (a_{dg}), and particulate backscattering (b_{bp}), from remote sensing reflectance (R_{rs}) within a reasonable order of accuracy (e.g. $\leq$ 35% of the mean *in situ* observation) for the coastal waters of the southern Chesapeake Bay.

4.2. Theory of PZ06_R_{rs} radiometric model

The downwelling plane irradiance just above the water surface [$E_d(0^+)$] can be easily measured in the field or calculated from radiative transfer models, and is assumed to obey a constant transmission factor through the air-sea interface [*Harding et al.*, 2005] as: $E_d(0^-) \approx 0.98E_d(0^+)$, without considering the effects from waves and cloud coverage on air-sea transmission. The constitution (e.g. IOPs and [Chl]) in the water column from the surface to maximum depth at $z = H$ is considered as vertically homogeneous for the purpose of equation simplicity. Under optically deep conditions, Eq. (4.2) applies, but the coefficients (l_1 and l_2) require re-analysis for various water and solar conditions. When the water column is optically shallow, the upwelling radiance (L_u) includes the contribution from bottom reflectance [$(L_u)_B$] in addition to that from water column [$(L_u)_C$]:

$$L_u = (L_u)_C + (L_u)_B \tag{4.3}$$

Defining the diffuse attenuation coefficient of upward radiance at the corresponding sensor's underwater zenith angle (θ_v'; which obey Snell's Law with θ_v) as $K_{Lu}(\theta_v')$ and assuming the sea floor is a Lambertian reflector with the bidirectional reflectance distribution function (Q_{ub}) of upwelling irradiance reflectance by the floor (E_{ub}) equal to π in all direction (θ, ϕ), $(L_u)_B$ can be expressed as [*Voss et al.*, 2003]:

$$(L_u)_B \approx (\frac{R_b}{\pi})E_d(H)\exp[-K_{Lu}(\theta_v')\times H] \tag{4.4}$$

$K_{Lu}(\theta_v')$ in optically shallow layer is reasonable to be expressed as [*Mobley*, 1994; *Voss et al.*, 2003]:

$$K_{Lu}(\theta_v') \approx \frac{a+b_b}{\cos(\theta_v')} \tag{4.5}$$

Thus, the contribution to remote sensing reflectance from the bottom reflectance, $(R_{rs})_B$, can be expressed as:

$$(R_{rs})_B = \frac{TL_u(0^-)}{E_d(0^+)} \approx T(\frac{R_b}{\pi})\frac{E_d(H)}{E_d(0^-)/0.98}\exp[-\frac{a+b_b}{\cos(\theta_v')}\times H] \tag{4.7}$$

Following *Maritorena et al.* [1994], the water column contribution to R_{rs} is derived and expressed as:

$$(R_{rs})_C \approx (R_{rs})_{deep}[1-\frac{E_d(H)}{E_d(0^-)}\exp(-K_{Lu}(\theta_v')\times H)] \tag{4.8}$$

In Eqs. (4.7) and (4.8), the calculation of the fraction of downwelling irradiance reaching the bottom $[E_d(H)/E_d(0^-)]$ was based on the method described in Chapter 3.

R_{rs} can then be expressed by the sum of Eqs. (4.7) and (4.8):

$$R_{rs} \approx (R_{rs})_{deep}\{1-\frac{E_d(H)}{E_d(0^-)}\exp[-\frac{a+b_b}{\cos(\theta_v')}H]\}+T(\frac{R_b}{\pi})\frac{E_d(H)}{E_d(0^-)/0.98}\exp[-\frac{a+b_b}{\cos(\theta_v')}H] \tag{4.9}$$

4.3. Applications

4.3.1. *Hydrolight*® simulations

This study employed the radiative transfer model, *Hydrolight*® v4.2, to provide exact solutions of radiance distribution above and below the surface. The set of inputs used to create the simulated above-water and in-water environment were described in Table 3.1. The coefficients (l_1 and l_2) were then determined by analysis of the R_{rs} outputs in the optically deep waters conditions with the same inputs described in Section 3.3.1.

Such derived l_1 and l_2 coefficients were compared with the *Hydrolight*® simulations for water condition with classical Case 1 IOPs as described in Table 3.1.

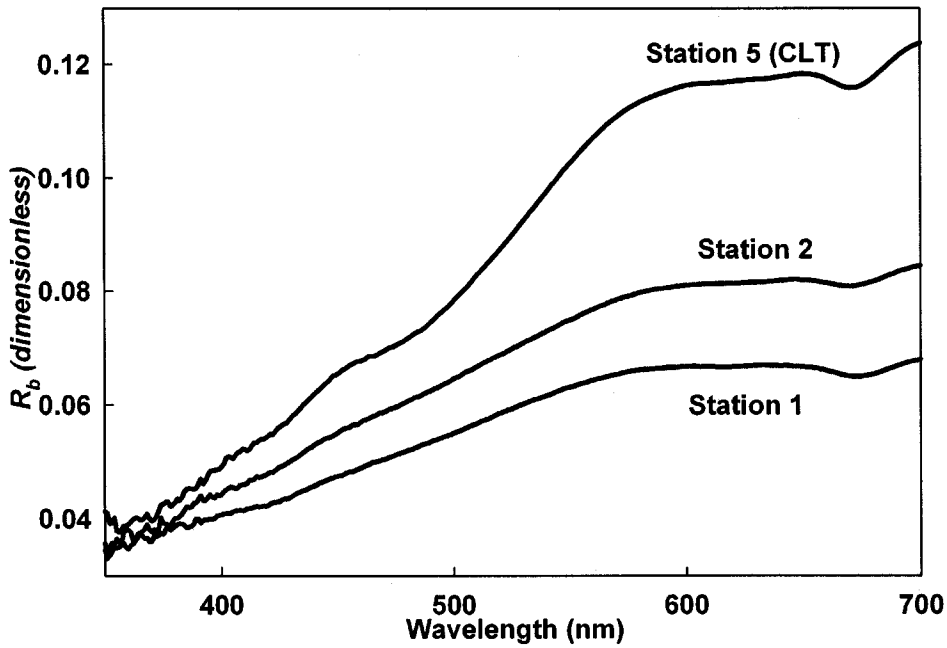

Figure 4.1. Variation of the bottom reflectance (R_b). The selected stations varied from relatively dark sediment at near Bay mouth station (Station 1; 36.91° N, 75.97° W), to brighter sediment at Station 2 (36.90° N, 75.87° W), and offshore brightest sediment at Station 5 (CLT; 36.91° N, 75.71° W).

In this study, the bottom reflectance (R_b) spectra were measured from box corer samples using a FieldSpec® spectrophotometer (Analytical Spectra Devices, Inc.) during CLT-Transect cruise (Fig. 2.1 and Table 2.1) on May 18th, 2005. R_b of lower Chesapeake Bay sediments increased away from the mouth. R_b was relatively dark at Station 1 (36.91° N, 75.97° W), brighter at Station 2 (36.90° N, 75.87° W), and brightest at Station 5 (the Chesapeake Light Tower; 36.91° N, 75.71° W) (Fig. 4.1). Restricted to the available data set of bottom reflectance for this lower Chesapeake Bay coastal region, Stations 1 and 5 were assume to represent the lower and upper limits, respectively, of bottom reflectance for optically shallow waters in this study region. The R_{rs} results

calculated from PZ06_R_{rs} for the optically shallow water conditions (*Hydrolight*® default classic Case 1 IOP conditions as shown in Table 3.1, and sea floor at 11 m; including three bottom reflectance from Fig. 4.1) were compared to the results generated by *Hydrolight*® using the percent root-mean-square (RMS) error as described before.

Since knowledge of spectral R_b and the water column depth (H) is required to include optically shallow effects, the unknown parameters in Eq. (4.9) are [Chl], $a_{dg}(443)$, and $b_{bp}(443)$ after applying IOP relationships as described in Chapter 2 and the selected parameters shown in Table 4.1 [*Garver and Seigel*, 1997; *Maritorena et al.*, 2002]. At least three R_{rs} values were required to solve three unknown parameters from the inverse modeling. In this study, six wavebands at 412, 443, 490, 532, 555, and 665 nm corresponding to the visible bands of SeaWiFS/MODIS sensor were selected. The retrievals of [Chl], $a_{dg}(442)$, and $b_{bp}(442)$ were computed by *Excel*® Solver by minimizing the mean square difference (MSD) between R_{rs} calculations from this PZ06_R_{rs} model and *Hydrolight*® simulation [*Maritorena et al.*, 2002]:

$$MSD = \frac{1}{n-1}\sum[R_{rs}(\lambda_i)_{model} - R_{rs}(\lambda_i)_{observed}]^2 \qquad (4.10)$$

The initial guesses of [Chl], $a_{dg}(442)$, and $b_{bp}(442)$ were set to 0.01, 0.002, and 0.002, respectively, while the lower limits of them were all set to 0.00001.

Table 4.1. The inputs and outputs for inverse modeling

Parameter	Value	Unit
$a_{ph}(443)$	$0.053[Chl]^{0.707}$	m^{-1}
$a_{ph}(412)/a_{ph}(443)$	0.876	dimensionless
$a_{ph}(490)/a_{ph}(443)$	0.560	dimensionless
$a_{ph}(532)/a_{ph}(443)$	0.336	dimensionless
$a_{ph}(555)/a_{ph}(443)$	0.229	dimensionless
$a_{ph}(665)/a_{ph}(443)$	0.414	dimensionless
S_{dg}	0.0151	nm^{-1}

b_{bp}/b_p	0.0184	dimensionless
b_{bp}_y	0.929	dimensionless

4.3.2. Field observations

R_{rs} spectra were measured using a series of SAS III multi-spectral sensors (Satlantic, Inc.) mounted on the Chesapeake Light Tower (CLT; 36.91° N, 75.71° W) about 38 m above the sea surface. The SAS sensors measured the downwelling plane irradiance above the water [$E_d(0^+)$; exactly, 38 m above the water], the downwelling sky radiance (L_{sky}), and the total upwelling radiance above the water surface (L_t) at ~ 90° azimuth angle and 40° nadir/zenith angle (the corresponding sensor zenith angle under water θ_v' was about 28.67°) at 13 wavelengths (380, 400, 412, 443, 490, 510, 532, 555, 665, 683, 700, 780, and 865 nm). The raw remote sensing reflectance [$(R_{rs})_{raw}$] was calculated as [*Mobley*, 1994, 1999]:

$$[R_{rs}(\lambda)]_{raw} = \frac{L_t(\lambda) - \rho L_{sky}(\lambda)}{E_d(\lambda)} \tag{4.11}$$

The ρ value corresponding to the downwelling sky radiance reflected back into the upwelling radiance from the surface of the water was calculated from *Hydrolight*® simulations based on wind speed, cloud cover, and local time (to compute solar zenith angle) [*Mobley*, 1994, 1999]. Wind speed was recorded from about 43.3 m above the surface of the water at the CLT by NOAA National Data Buoy Center (NDBC) (http://www.ndbc.noaa.gov/station_history.php?station=chlv2), and was approximately 1.16 times its value at 10 m above the water [*Su et al.*, 2002]. Atmospheric correction of R_{rs} was made by assuming that all photons at 865 nm entering the L_t sensor were scattered by the atmosphere between the water surface and the sensor position and propagated through the other visible bands [*Mueller et al.*, 2002]:

$$R_{rs}(\lambda) = [R_{rs}(\lambda)]_{raw} - [R_{rs}(865)]_{raw} \quad (4.12)$$

In addition, R_{rs} was calculated from an under-water free falling HyperPro II hyperspectral radiometric system (Satlantic, Inc.), during the CLT-Transect cruises (Chapter 2). The HyperPro recorded the downwelling irradiance above the water surface [$E_d(0^+)$], as well as the in-water downwelling irradiance [$E_d(z)$] and the upwelling radiance throughout the water column [$L_u(z)$]. R_{rs} was calculated from the ProSoft v7.6 software (Satlantic, Inc.) by propagating L_u to the surface from profile estimates of K_{Lu}. The values of [Chl] and IOPs of absorption (a), scattering (b), and backscattering (b_b) were also measured at the CLT, as described in Chapter 2.

The R_{rs} spectra calculated from this modeling approach (PZ06_R_{rs}) based on water and atmospheric conditions were compared to field measurements. The inversely retrieving [Chl], $a_{dg}(443)$, and $b_{bp}(443)$ obeyed the same method in Section 4.3.1 except using the derived IOP relationships described in Chapter 2.

In addition, the field measurements of [Chl] were compared to those estimated from the OC3M algorithm [*O'Reilly et al.*, 2000] and from an empirical log-transformed linear equation:

$$\log(Chl) \propto \log\frac{R_{rs}(\max)}{R_{rs}(555)} \quad (4.13)$$

where R_{rs}(max) represents the maximum R_{rs} among 442, 490, and 510 nm.

4.4. Results

4.4.1. The derived l_1 and l_2 coefficients

The coefficient l_1 was found to be relatively independent of θ_s, while l_2 varied significantly ($r^2 = 0.99$) with θ_s, especially when $\theta_s > 30°$ (Fig. 4.2):

$$l_1 \approx 0.0833 \tag{4.14}$$

$$l_2 \approx 0.0659 + 0.0541\cos\theta_s + 0.1464(\cos\theta_s)^2 - 0.2727(\cos\theta_s)^3 + 0.1172(\cos\theta_s)^4 \tag{4.15}$$

The first term in Eq. (4.2) might be explained by assuming that the incident photons were scattered once, from which the two-flow theory resulted in the relatively constant coefficient (l_1). The second term in Eq. (4.2) accounted for the second scattering event, which thus depended on the incident solar angle.

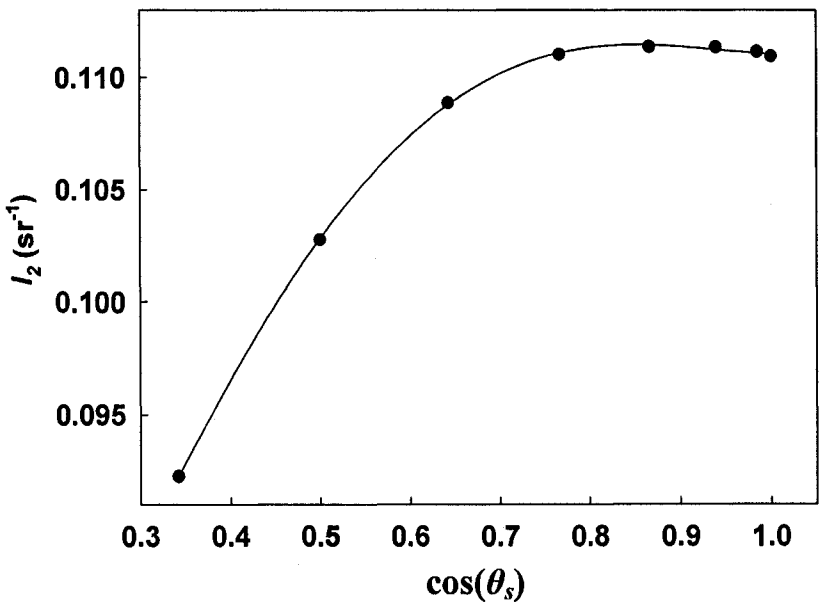

Figure 4.2. Variation of the derived l_2 coefficients with the solar zenith angle (θ_s). Data points are connected by regression line (solid) of Eq. (4.15).

4.4.2. Verification against *Hydrolight*® simulations

Forward modeling—In optically deep water conditions, both l_1 and l_2 coefficients derived from the *Gordon et al.* [1988] model and from this study performed similarly

(RMS = 9.1% and 5.2%, respectively) in predicting R_{rs} from IOPs (Figs. 4.3a-b), except that the *Gordon et al.* [1988] model agreed better in clearer waters but worse in particle-rich waters than PZ06_R_{rs} (Fig. 4.3f). Since the coastal waters are usually rich in particles from sedimentary resuspension and riverine outflow, the new l_1 and l_2 coefficients are expected to work better in coastal waters than those derived from the *Gordon et al.* [1988] model.

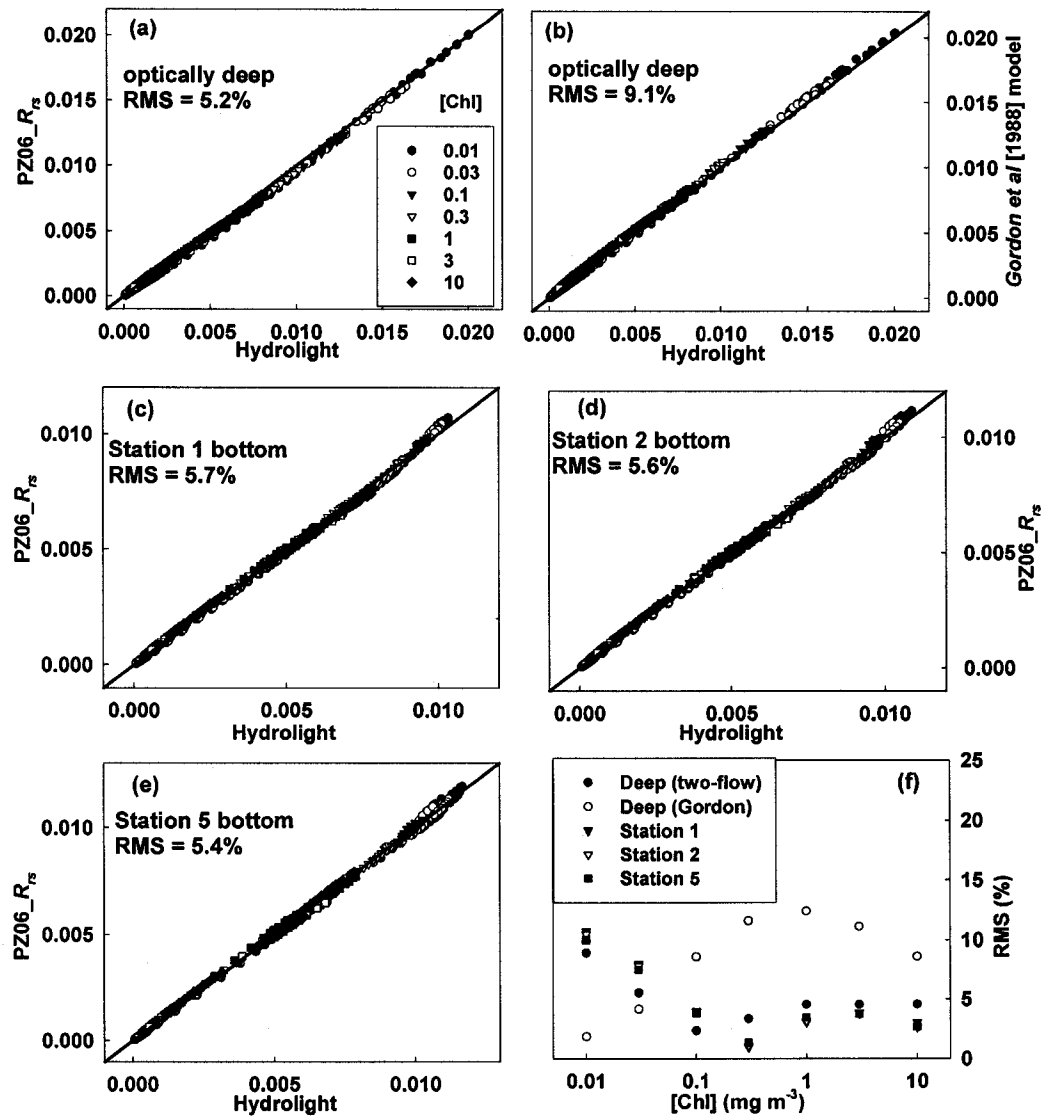

Figure 4.3. Comparison of R_{rs} spectrum. The *Hydrolight*® simulations were compared to the results from (a) PZ06_R_{rs}, (b) the *Gordon et al.* [1988] model in optically deep waters, and PZ06_R_{rs} in optically shallow waters with the bottom conditions as (c) Station 1, (d) Station 2, and (e) Station 5 (CLT). (f) Root-mean-square (RMS) errors for each [Chl] condition.

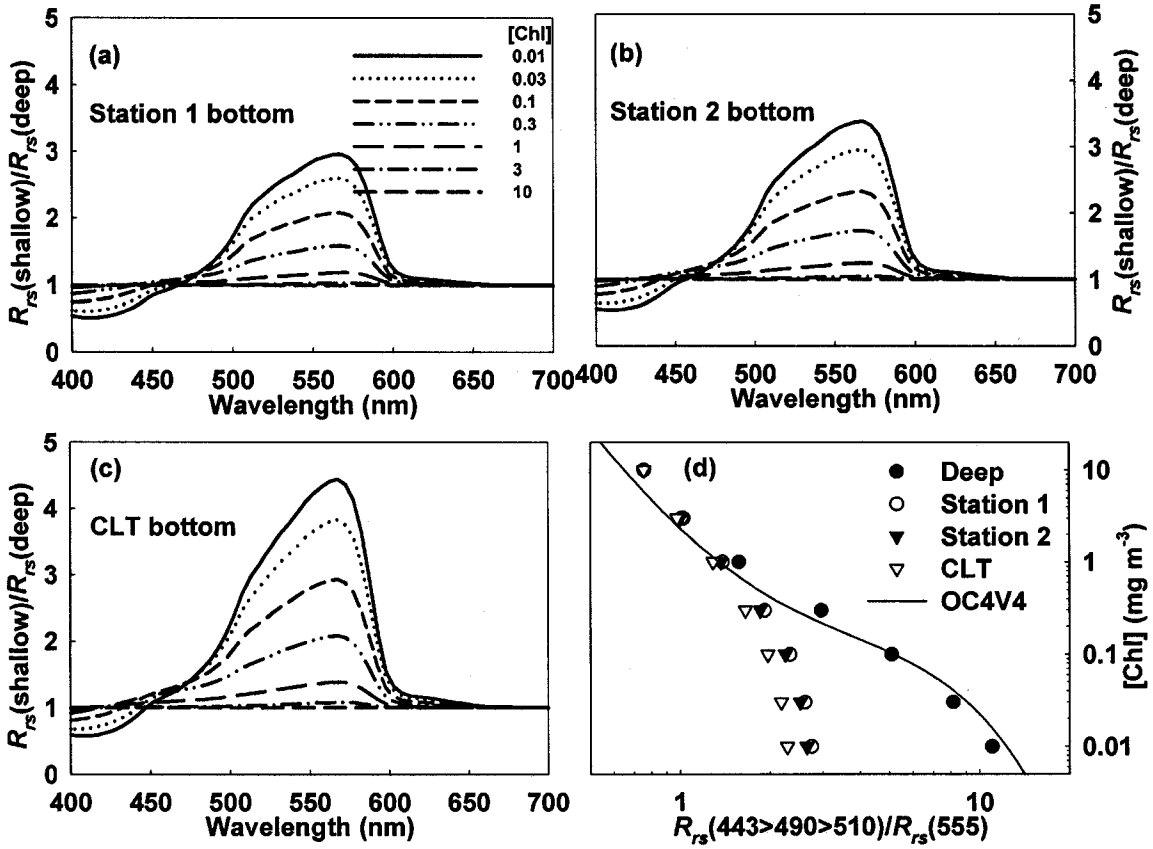

Figure 4.4. R_{rs} of optically shallow waters normalized to those in optically deep waters. The bottom conditions were those at (a) Station 1, (b) Station 2, and Station 5 (CLT). (d) The R_{rs} band ratio to R_{rs}(555) from the maximum value at 443, 490, and 510 nm, compared to the OC4V4 algorithm.

PZ06_R_{rs} also agreed with *Hydrolight*® simulated R_{rs} spectra in optically shallow waters with the RMS error < 6% for all three selected bottom conditions in various water conditions ([Chl] = 0.01 to 10.0 mg m^{-3}) (Figs. 4.3c-e). The RMS errors for optically shallow waters (e.g. ~ 4% for [Chl] = 0.1 mg m^{-3}) were consistent with those in optically deep waters (e.g. 2.3% for [Chl] = 0.1 mg m^{-3}) (Fig. 4.3f), indicating that little extra error

was introduced from the bottom reflectance compared to the quadratic equation for optically deep waters. The bottom reflectance significantly increased R_{rs} compared to optically deep waters, particularly between 500 and 600 nm (Figs. 4.4a-c). Since ocean color algorithms (e.g. OC4V4 and OC3M) usually calculate [Chl] from the maximum band ratio R_{rs} at 440 to 510 nm vs. $R_{rs}(555)$, [Chl] is often significantly overestimated in optically shallow waters unless the bottom effects are removed (Fig. 4.4d). For example, the [Chl] distribution from SeaWiFS OC4V4 retrievals in Bahamas Banks where the waters are relatively clear and the sea floor is relatively bright often appears as a dense phytoplankton bloom (Fig. 1.1).

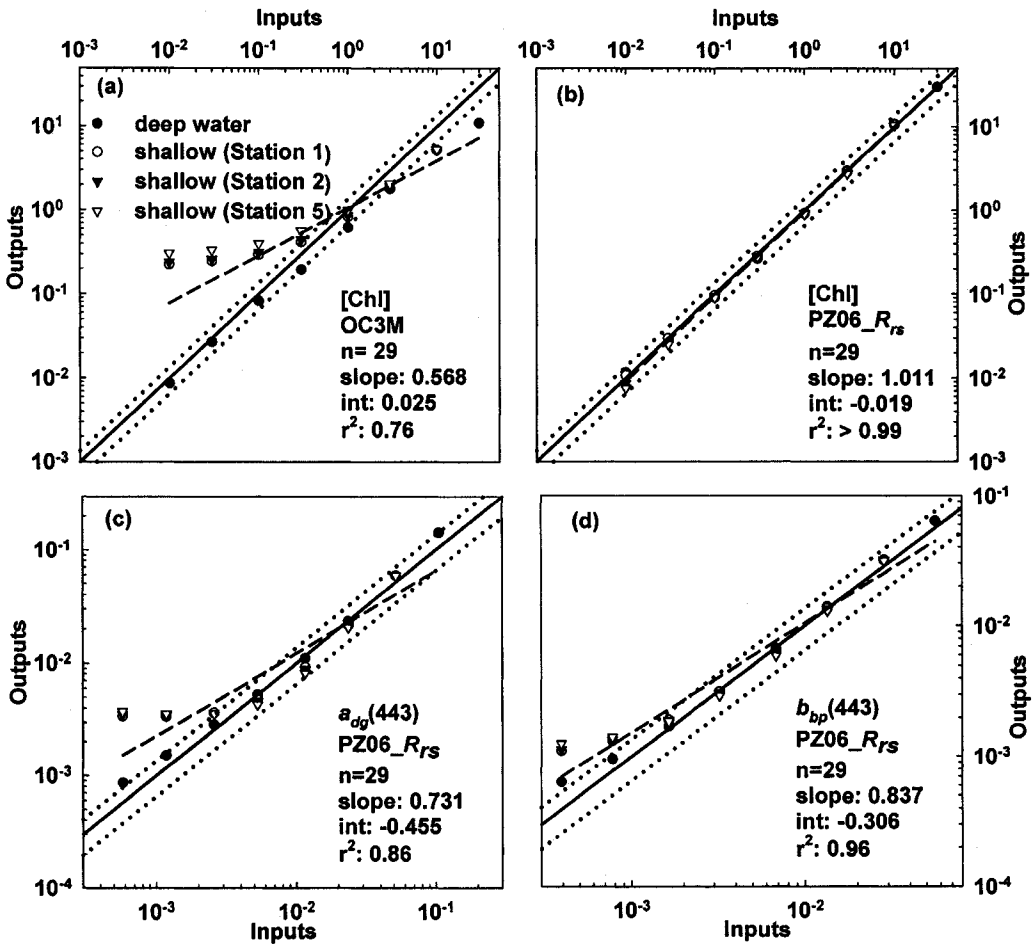

Figure 4.5. Analyses of the inversion from *Hydrolight*® simulations. (a) [Chl] from OC3M algorithm. The retrieved products from PZ06_R_{rs} were shown on (b) [Chl], (c) $a_{dg}(443)$, and (d) $b_{bp}(443)$. Solid lines: 1:1; dotted lines: 65% to 135% accuracy target; dashed lines: log-transformed linear regression.

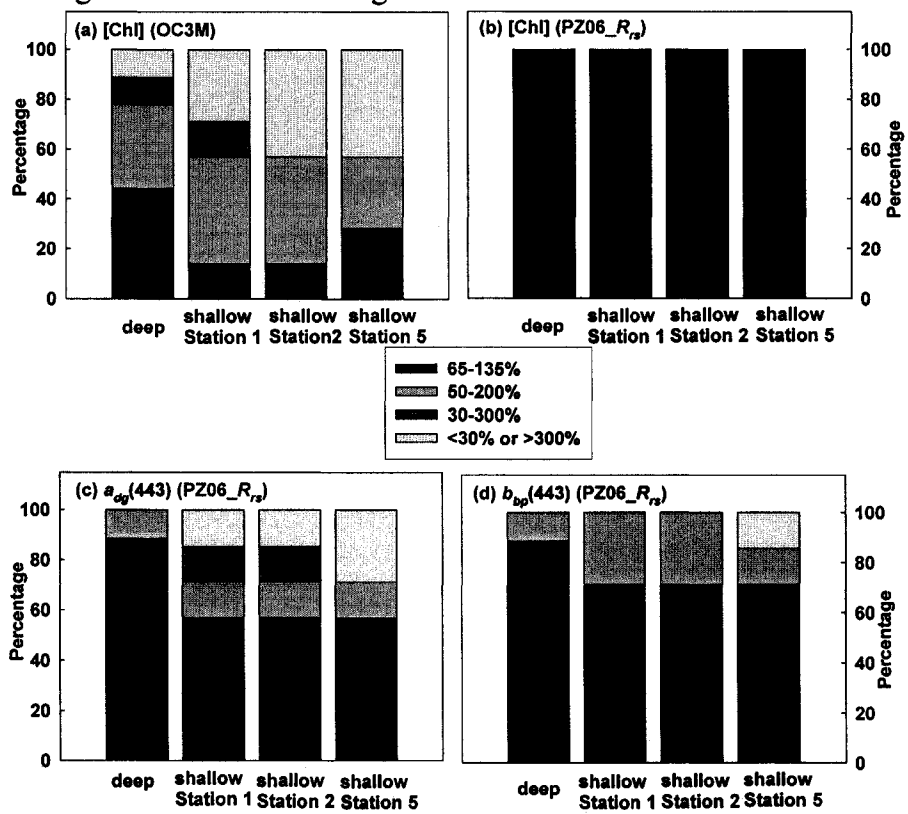

Figure 4.6. Accuracy analysis of the inversion from *Hydrolight*® simulations. The percentages of the retrieved products of (a) [Chl] from OC3M, and (b) [Chl], (c) $a_{dg}(443)$, and (d) $b_{bp}(443)$ from PZ06_R_{rs}, were counted within the accuracy of 65% to 135%, 50% to 200%, and 30% to 300% of the true values.

Inverse modeling—OC3M retrieved [Chl] < 3 mg m^{-3} relatively accurately for optically deep Case 1 waters, but tended to be underestimated [Chl] at higher concentrations (Fig. 4.5a). However, OC3M did not retrieve [Chl] accurately in the optically shallow conditions, especially when the waters were relatively clear (e.g. [Chl] < 0.3 mg m^{-3}) (Fig. 4.5a). About 40%, 80%, and 90% of [Chl] were predicted by OC3M within the accuracy of 65% to 135%, 50% to 200%, and 30% to 300%, for the optically deep waters, respectively (Fig. 4.6a). The agreements decreased significantly for the

optically shallow waters where only 20% to 30% of [Chl] could be retrieved within the accuracy of 65% to 135%, while < 60% and <70% within the accuracy of 50% to 200% and 30% to 300%, respectively (Fig. 4.6a).

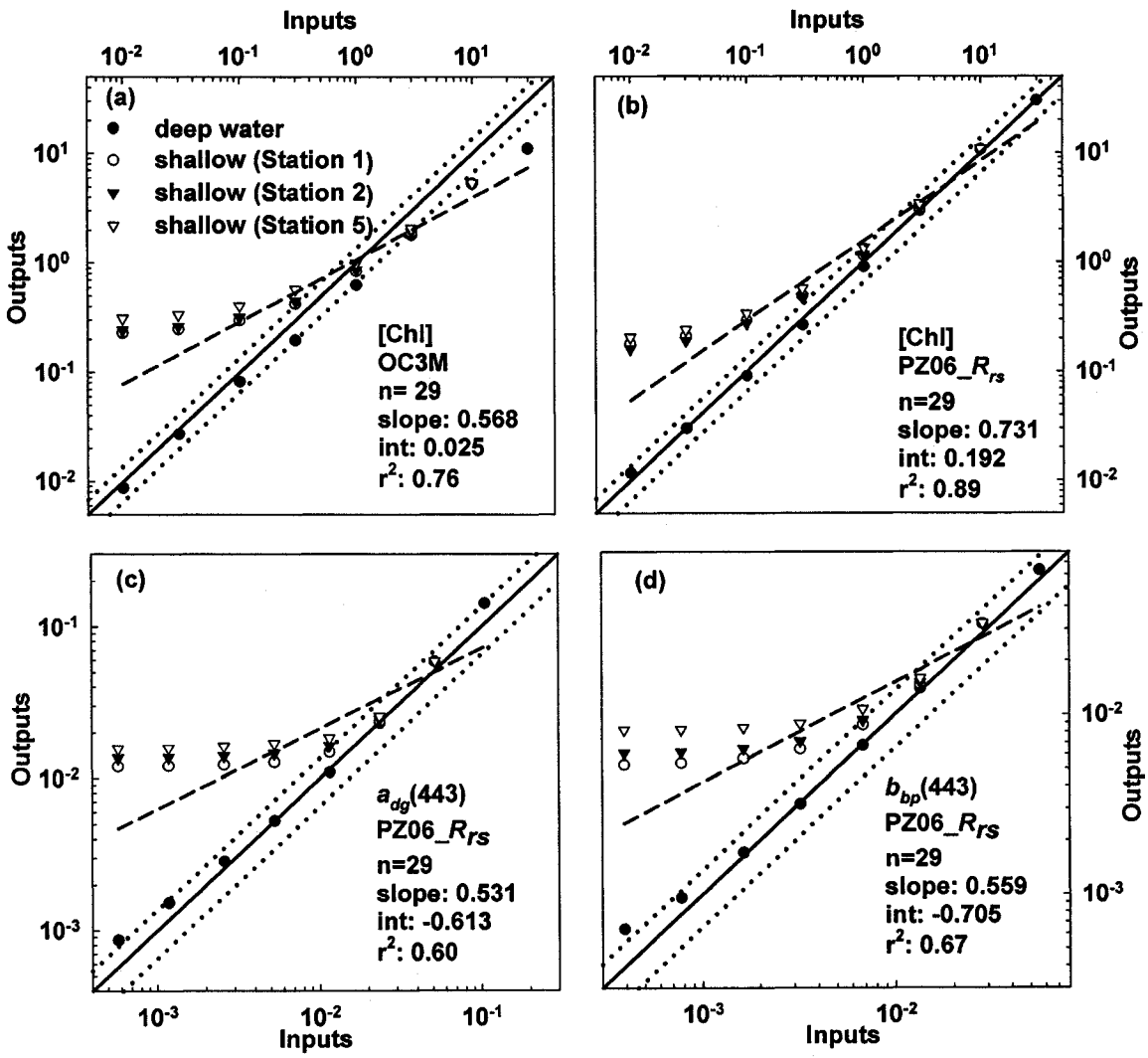

Figure 4.7. Analyses of the inversion from *Hydrolight*® simulations without considering bottom effects. (a) [Chl] from OC3M algorithm. The retrieved products from PZ06_R_{rs} were shown on (b) [Chl], (c) $a_{dg}(443)$, and (d) $b_{bp}(443)$. Solid lines: 1:1; dotted lines: 65% to 135% accuracy target; dashed lines: log-transformed linear regression.

The inversion of PZ06_R_{rs} produced better retrievals of [Chl] than OC3M (Fig. 4.5b). All of [Chl] were predicted within the accuracy of 65% to 135%, regardless optically deep or optically shallow conditions (Fig. 4.6b). In addition, PZ06_R_{rs} also retrieved $a_{dg}(443)$, and $b_{bp}(443)$ accurately, except in clear, optically shallow conditions (e.g. [Chl] < 0.1 mg m^{-3}) when the bottom reflectance effect overwhelmed backscattering from the water column (Figs. 4.5c-d). More than 90% of $a_{dg}(443)$ and $b_{bp}(443)$ were predicted within the accuracy of 65% to 135% for optically deep water conditions, and ~60% of $a_{dg}(443)$ and ~70% of $b_{bp}(443)$ were predicted within this accuracy for optically shallow water conditions (Figs. 4.6c-d).

If the bottom effect was ignored in optically shallow waters, the SA models would overestimate the retrieved products of [Chl], $a_{dg}(443)$ and $b_{bp}(443)$ as the bottom reflectance was treated as the "extra" contribution from the constitutes of the water column (Fig. 4.7). In relatively clear waters (e.g. [Chl] < 0.3 mg m^{-1}), the SA models retrieved [Chl], $a_{dg}(443)$ and $b_{bp}(443)$ with about the same accuracy as OC3M (Fig. 4.7).

4.4.3. Validation against the field observations

Figure 4.8 showed total R_{rs} spectra measured at the CLT when water IOPs were also available. The R_{rs} spectra usually had a peak at 490 – 532 nm and in some cases the R_{rs} at green wavelengths was relatively high implying relatively rich particulate matter (Fig. 4.8).

Forward modeling—Three samples of R_{rs} from SAS at the CLT representing relatively clear water ([Chl] = 0.36 mg m^{-3}; 16 July 2001), moderately turbid water ([Chl] = 1.38 mg m^{-3}; 17 July 2001), and highly turbid ([Chl] = 3.40 mg m^{-3}; 25 July 2001), were selected for comparisons. Even in the relatively turbid sample (25 July 2001), the

bottom reflectance contributed ~ 20% to R_{rs}(555), and about 70% in the relatively clear sample (16 July 2001) (Fig. 4.9a-c). The RMS errors between the *Hydrolight*® simulations and field observations were 8.5%, 12.9%, and 8.5% for the clear, moderately turbid, and highly turbid stations, respectively, while PZ06_R_{rs} introduced RMS errors of 10.0%, 13.0%, 7.0% for these three samples (Fig. 4.9). PZ06_R_{rs} agreed better (RMS errors of 3.8%, 2.9%, and 4.2% for the clear, moderately turbid, and highly turbid samples, respectively) with *Hydrolight*® simulations with the same inputs of IOPs as measured just from the surface water. Since both *Hydrolight*® and PZ06_R_{rs} required complete knowledge of the vertical distribution of IOPs, which was often lacking, the application of the IOPs from the surface to represent the whole column would cause R_{rs} predicted from models to deviate from the field measurements.

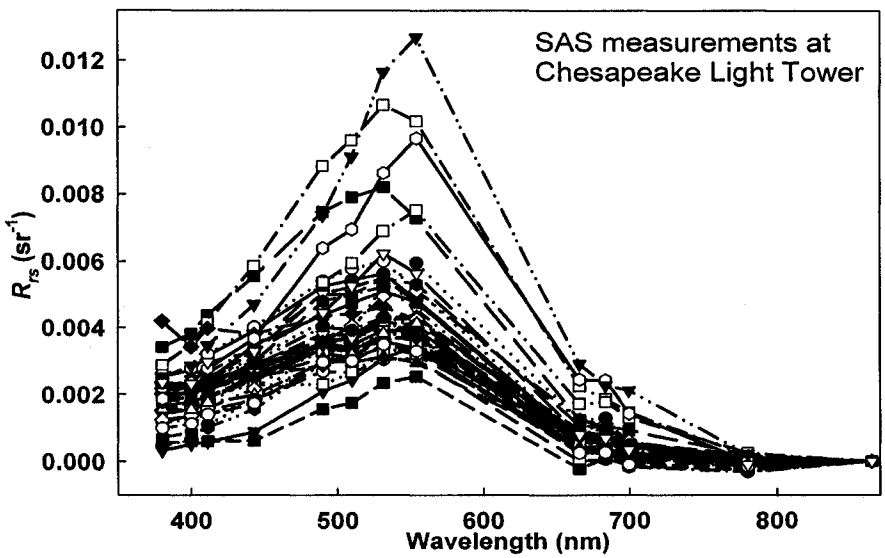

Figure 4.8. Remote sensing reflectance (R_{rs}) measured at the Chesapeake Light Tower (CLT). Stations were those from which IOPs were also available.

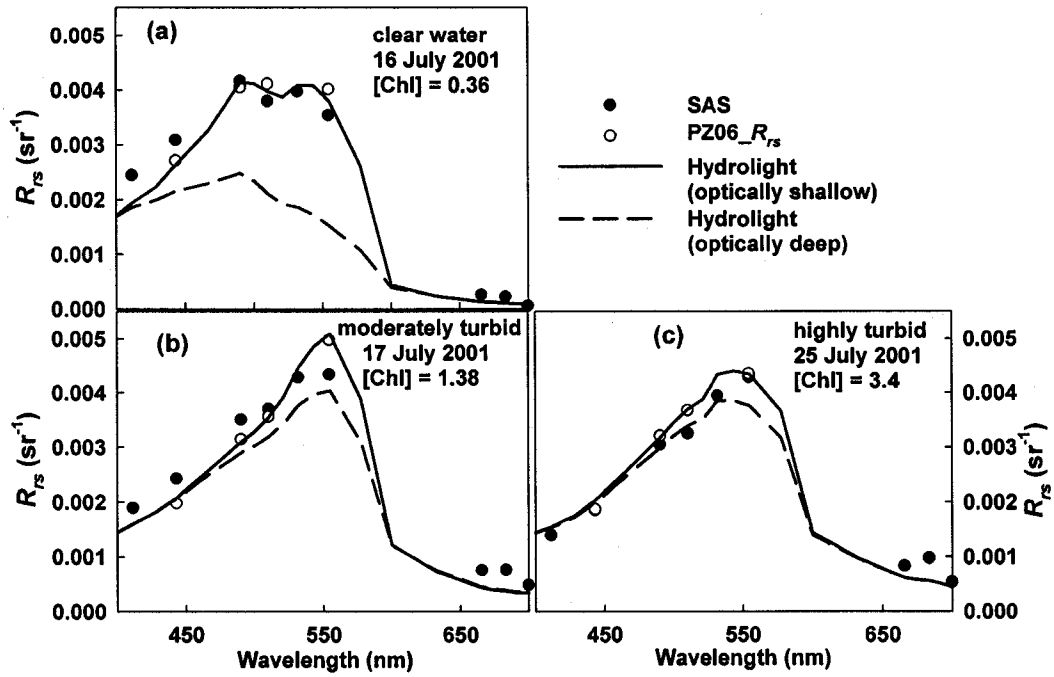

Figure 4.9. Comparisons of spectral R_{rs} from simulations and measurements. The radiative transfer models included *Hydrolight*® and PZ06_R_{rs}. Three selected samples were (a) relatively clear, (b) moderately turbid, and (c) highly turbid water conditions at the Chesapeake Light Tower (CLT).

Inverse modeling—Similar to the results of the sensitivity tests in Section 4.4.2, [Chl] retrieved from OC3M algorithm was significantly overestimated, especially at lower [Chl] (Fig. 4.10a). Less than 5% and < 20% of [Chl] was able to be predicted from OC3M within the accuracy of 65% to 135% and 50% to 200% of the observations, respectively (Figs. 4.10a and 4.11). Instead, the relationship between [Chl] and R_{rs} in this data set was better expressed by an empirical regression (n = 44, r^2 = 0.70) (Fig. 4.12):

$$\log[Chl] = -0.1045 - 4.2869 \log[\frac{R_{rs}(\max)}{R_{rs}(555)}] \quad (4.16)$$

About 30% and 90% of [Chl] was predicted from the above equation within the accuracy of 65% to 135% and 50% to 200% of the observations, respectively.

The retrieved products of [Chl], $a_{dg}(443)$, and $b_{bp}(443)$ from PZ06_R_{rs} were more scattered (r^2 = 0.16, 0.37, and 0.74, respectively) due to the sensitivity of semi-analytic (SA) inverse models on the accurate estimation of R_{rs} spectrum (Figs. 4.10b-c). Compared to the field observations, however, PZ06_R_{rs} predicted about 30%, 55%, and 70% of the retrieved products of [Chl], $a_{dg}(443)$, and $b_{bp}(443)$ within the accuracy of 65% to 135%, while about 60%, 90%, and 90% within the accuracy of 50% - 200% (Fig. 4.11).

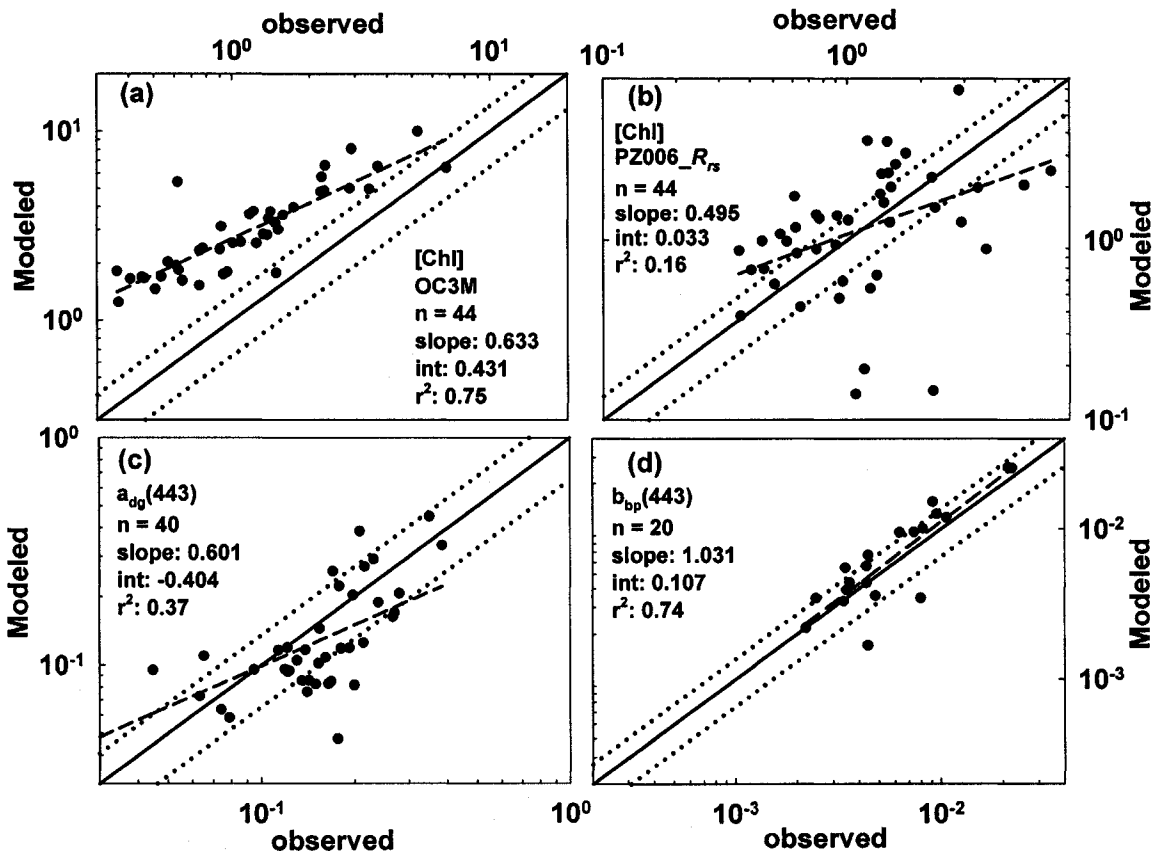

Figure 4.10. Analyses of the inversion from field measurements. (a) [Chl] from OC3M algorithm. The retrieved products from PZ06_R_{rs} were shown on (b) [Chl], (c) $a_{dg}(443)$, and (d) $b_{bp}(443)$. Solid lines: 1:1; dotted lines: 65% to 135% accuracy target; dashed lines: log-transformed linear regression.

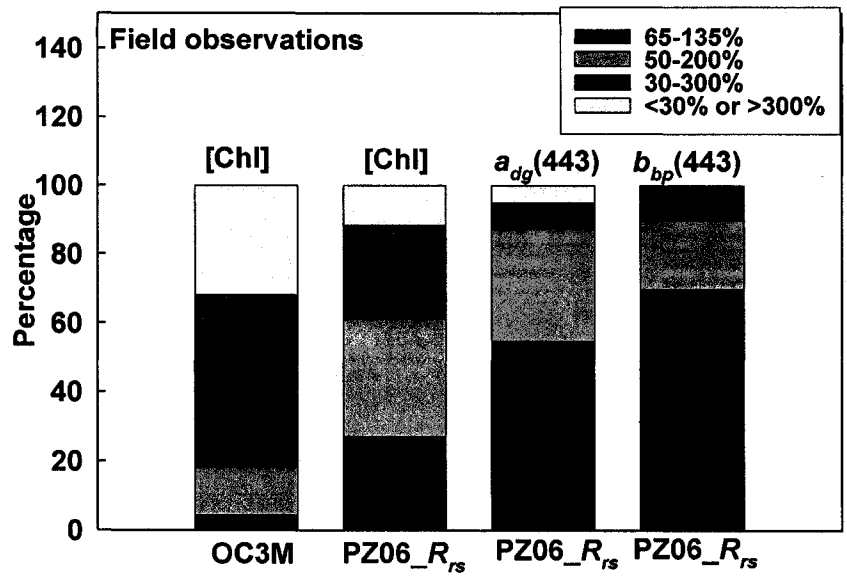

Figure 4.11. Accuracy analysis of the inversion from field measurements. The percentages of the retrieved products of (a) [Chl] from OC3M, and (b) [Chl], (c) $a_{dg}(443)$, and (d) $b_{bp}(443)$ from PZ06_R_{rs}, were counted within the accuracy of 65% to 135%, 50% to 200%, and 30% to 300% of the true values.

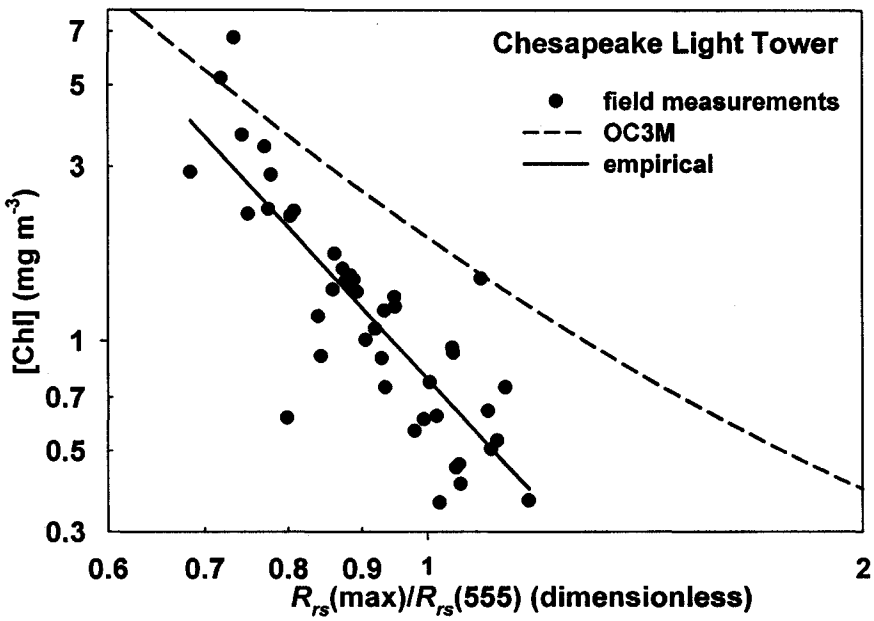

Figure 4.12. The empirical regression of [Chl] from R_{rs} band ratio. The data from the measurements at the Chesapeake Light Tower (CLT) were log-transformed. The OC3M equation is also shown for comparison.

If the bottom effect was ignored, the SA models were less effective (e.g. ~ 14% of total data set) in retrieving [Chl] than in retrieving $a_{dg}(443)$ and $b_{bp}(443)$ (Fig. 4.13b) since the latter two constitutes were generally the major contributions to absorption and backscattering in this coastal region (Chapter 2). Similar to the results of the sensitivity tests in Section 4.4.2, [Chl] and $b_{bp}(443)$ were significantly overestimated but the overestimation of $a_{dg}(443)$ retrieval was not obvious (Figs. 4.13b-d).

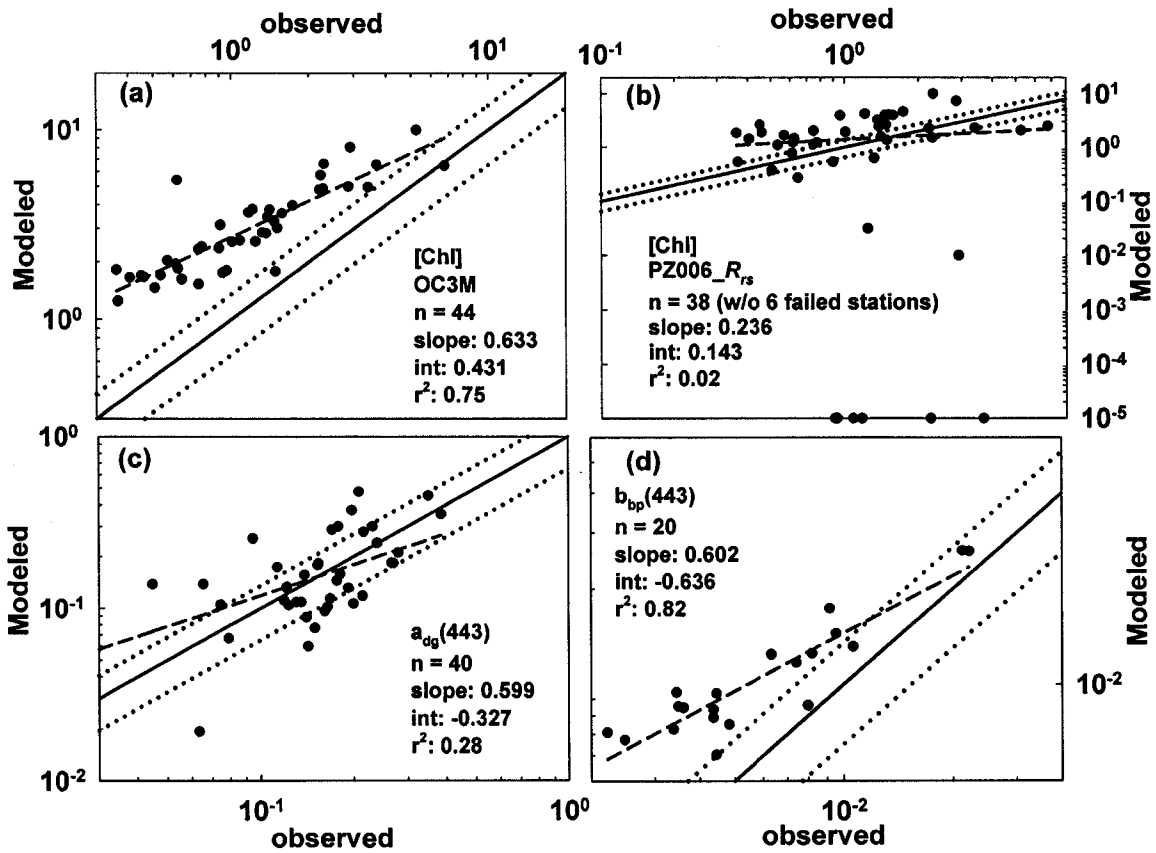

Figure 4.13. Analyses of the inversion from field measurements without considering the bottom effects. (a) [Chl] from OC3M algorithm. The retrieved products from PZ06_R_{rs} were shown on (b) [Chl], (c) $a_{dg}(443)$, and (d) $b_{bp}(443)$. Solid lines: 1:1; dotted lines: 65% to 135% accuracy target; dashed lines: log-transformed linear regression.

4.5. Discussion

Compared to the empirical ocean color equations (e.g. OC3M and the log-transformed linear regression) based on the R_{rs} band ratio to calculate [Chl], the semi-analytic models (e.g. GSM01, GSM01-CLT, and PZ06_R_{rs} models) have at least two advantages. First, more products, including [Chl], a_{dg}, and b_{bp}, were retrieved. Based on the empirical relationships, such as the power function between b_{bp} and a_d, CDOM absorption (a_g) could also be estimated, which provides further retrieval of salinity gradient for the riverine coastal region (Chapter 2). Such products provide potential and promising methods to monitor the water quality (e.g. CDOM concentration), to study the biogeochemical process (e.g. freshwater outflow track by the salinity distribution), to investigate the benthic optical environment (e.g. K_d to be represented as the water turbidity degree), and to study the ecosystem level processes (e.g. primary productivity and carbon cycling) from space-borne remote sensing. Second, SA modeling with its basic IOP characters is less influenced by the selected data set concerned with the sampling seasons. Empirical ocean color equations derived for the winter-spring bloom season could be very different from that in summer season due to the possible shift of particle size from dominant large-cell phytoplankton in spring to the mixture of small-cell phytoplankton and mineral in summer in this coastal region. If the water column is optically shallow, the empirically derived ocean color equations will be totally different from those derived in the seasons characterized by optically deep water conditions.

Although the mean water column was 11 m and the bottom reflectance (R_b) was as low as 0.04 to 0.12 between 400 and 700 nm in CLT, the bottom effect on R_{rs} should not be ignored, especially for low [Chl] clear conditions. The contribution to R_{rs} from the

bottom reflectance might be higher than that from the water column. Since the lower Chesapeake Bay coastal waters often include optically shallow conditions, especially in summer when the freshwater outflow is limited (Chapter 3), the inclusion of bottom reflectance effect in the semi-analytic inverse retrievals from remote sensing is necessary, or the optical properties from particles (e.g. b_{bp}) will be significantly overestimated (Figs. 4.7 and 4.13). In fact, the retrieved products such as [Chl] and $b_{bp}(443)$ from the SeaWiFS image (Figs. 2.9 and 2.10) seemed to be overestimated in some degree for the waters nearby the CLT by applying GSM01-CLT without considering the bottom effect. However, the knowledge of bottom conditions including the measurements of bottom reflectance is limited [*Ackleson*, 2003]. In processing with remote sensing imagery, it may be practically applicable to assume that R_b increases linearly or quadratic along with the wavelengths from 400 to 600 nm, while it is less variable between 600 and 700 nm (e.g. Fig. 4.1). Such an assumption will add two more variable parameters [$R_b(400)$ and $R_b(600)$] to PZ06_R_{rs} but make it more amendable even without detailed knowledge of the bottom condition.

PZ06_R_{rs} assumes the bottom is a flat Lambertian reflector from which the radiation is scattered equally in all directions. Compared to a sloped floor (less than 20°) and non-Lambertian bottom, radiative transfer simulations showed the effects of non-isotopic bidirectional reflectance distribution function (BRDF) on the upwelling radiance and water-leaving radiance typically caused errors less than 10% [*Mobley and Sundman*, 2003; *Mobley et al.*, 2003]. However, due to the sensitivity of SA modeling, such an order of error may also introduce significant deviation in inversely retrieving the products like [Chl], a_{dg}, and b_{bp}.

PZ06_R_{rs} is based on the assumption that IOPs of the water column is vertically homogeneous, and can be applied to the stratified waters. The oceanic open seas may have their mixed layer relatively constant of IOPs and make it possible to use the surface condition to represent the whole water column. In coastal waters, however, the geometrically shallow condition often causes more error to represent the whole column condition with the surface condition. The bottom substrates have been found to have effects on the vertical distribution of IOPs and radiative transfer modeling [*Boss and Zaneveld*, 2003]. The retrieved products from above-water remote sensing are in fact the integrated values for the whole column, not only from the surface layer.

CHAPTER 5

CONCLUSION AND FUTURE WORK

5.1. Conclusion

In this dissertation, a substantial investigation of bio-optical properties for the coastal waters of the southern Chesapeake Bay was conducted. The relationships of the inherent optical properties (IOPs) in this coastal region were found to be regionally specific relative to the Case 1 waters and other coastal waters. Such regionally specific relationships appears to be necessary for remote sensing analysis of the coastal waters of the southern Chesapeake Bay, in which riverine outflow often plays a critical role in controlling the biogeochemical processes and the spatial and temporal distributions of salinity, [Chl], CDOM, and sedimentary concentration. The SeaWiFS products, such as [Chl], $a_{dg}(443)$, $b_{bp}(443)$, $a_g(443)$, and salinity, retrieved from GSM01-CLT by applying the regionally specific IOP relationships, produce reasonable images for the lower Middle Atlantic Bight (MAB), from which riverine outflow and the Gulf Stream mixing are relatively clear.

PZ06_E_d was relatively successful in describing the vertical distribution of E_d and K_d from IOPs and sky conditions and significantly improved from the simple *Gordon* [1989] model. The application of PZ06_E_d to SeaWiFS imagery for monitoring the water turbidity [e.g $K_d(490)$] for the lower MAB is also reasonable and significantly improved relative to the empirical equation based on L_w band ratio [*Mueller*, 2000].

PZ06_R_{rs} successfully described the relationship between remote sensing reflectance (R_{rs}) and IOPs for both optically deep and optically shallow waters relatively

successful. Its application in inverse modeling can produce more data points within the reasonable accuracy of 65% to 135% of the "true" values. In contrast, the global ocean color algorithms (e.g. OC3M) or the semi-analytic models (e.g. GSM01 and GSM01-CLT) without considering the bottom effects introduced extra errors in inversely retrieving in coastal waters.

Above all, the processing and results shown in this paper proved that water quality and biogeochemical parameters can be retrieved from remote sensing of coastal regions, providing accurate regional algorithms are available to analyze the image data. This study provided a set of coherent data from which such regional algorithms were constructed for the lower Chesapeake Bay.

5.2. Future work

The relationships between IOPs and biogeochemical parameters (e.g. [Chl], CDOM concentration, and sedimentary concentration) will continue to be investigated. More focus should be paid to the variation of wavelength-depended exponential slope of the CDOM spectra: Does it vary along with the distance leaving from the Bay mouth? How does it co-vary with CDOM absorption, [Chl], or particulate backscattering? How does the S_g variation affect the water-leaving signal? The community structure of phytoplankton, its seasonal and spatial variation, and its variation to the net primary production, on the other hand, may be of interest in the future [*Hoge*, 2006; *Hoge et al.*, 1999; *Trees et al.*, 2000].

PZ06_E_d and PZ06_R_{rs} in predicting E_d and R_{rs} will require further development after analyzing the effects from a more complete environment (including water column,

bottom reflectance, atmosphere, and solar positions at least). For example, the approaches in this study were based on the simulations under the oceanic airmass environment, which might consist of lower particulate concentrations in the air compared to the real coastal zones. The inversion of satellite remote sensing and its application to study the short-term and long-term environment change, e.g. phytoplankton blooming and carbon cycle in the coastal regions, will be the focus in the future.

REFERENCES

Acker, J. G., L. W. Harding, G. Leptoukh, T. Zhu, and S. Shen (2005), Remotely-sensed chl *a* at the Chesapeake Bay mouth is correlated with annual freshwater flow to the Chesapeake Bay, *Geophys. Res. Lett.*, 32, L05061, doi: 10.1029/2004GL 021852.

Ackleson, S. G. (2003), Light in shallow waters: a brief research review, *Limnol. Oceangr.* 48 (1, part 2), 323 – 328.

Albert, A., and P. Gege (2006), Inversion of irradiance and remote sensing reflectance in shallow water between 400 and 800 nm for calculations of water and bottom properties, *Appl. Opt.*, 45, 2331 – 2343.

Arnone, R. A., and P. C. Gallacher (1996), Cruise report of the Weatherbird II during the Chesapeake Bay Outfall Plume Experiment (COPE 1, Sept 25 – 27, 1996), Naval Research Lab, Stennis Space Center, MS.

Austin, J. (2002), Estimating the mean ocean-bay exchange rate of the Chesapeake Bay, *J. Geophys. Res., 107*(C11), 3192, doi: 10.1029/2001JC001246.

Babin, M., A. Morel, V. Fournier-Sicre, F. Fell, and D. Stramski (2003a), Light scattering properties of marine particles in coastal and open ocean waters as related to the particle mass concentration, *Limnol. Oceanogr., 48*(2), 843 – 859.

Babin, M., D. Stramski, G. M. Ferrari, H. Claustre, A. Bricaud, G. Obolensky, and N. Hoepffner (2003b), Variations in the light absorption coefficients of phytoplankton, nonalgal particles, and dissolved organic matter in coastal waters around Europe, *J. Geophys. Res., 108*(C7), 3211, doi: 10.1029/2001JC000882.

Bannister, T. T. (1992), Model of the mean cosine of underwater radiance and estimation of underwater scalar irradiance, *Limnol. Oceangr.*, 37, 773 – 780.

Barnard, A. H., W. S. Pegau, and J. R. V. Zaneveld (1998), Global relationships of the inherent optical properties of the oceans, *J. Geophys. Res., 103*(C11), 24955 – 24968.

Berwald, J., D. Stramski, C. D. Mobley, and D. A. Kiefer (1995), Influences of absorption and scattering on vertical changes in the average cosine of the underwater light field, *Limnol. Oceangr.*, 40 1347 – 1357.

Behrenfeld M. J., E. Boss, D. A. Siegel, and D. M. Shea (2005), Carbon-based ocean productivity and phytoplankton physiology from space, *Global Biogeochem. Cycles*, 19, GB1006, doi:10.1029/2004GB002299.

Binding, C. E., and D. G. Bowers (2003), Measuring the salinity of the Clyde Sea from remotely sensed ocean colour, *Estuar. Coast. Shelf Sci.*, 57, 605 – 611.

Boss, E., W. S. Pegau, J. R. V. Zaneveld, and A. H. Barnard (2001a), Spatial and temporal variability of absorption by dissolved material at a continental shelf, *J. Geophys. Res.*, *106*(C5), 9499 – 9507.

Boss, E., M. S. Twardowski, and S. Herring (2001b), Shape of the particulate beam attenuation spectrum and its inversion to obtain the shape of the particulate size distribution, *Appl. Opt.* 40, 4885 – 4893.

Boss, E., W. S. Pegau, M. Lee, M. Twardowski, E. Shybanov, G. Korotaev, and F. Baratange (2004), Particulate backscattering ratio at LEO 15 and its use to study particle composition and distribution, *J. Geophys. Res.*, *109*(C01014), doi: 10.1029/2002JC001514.

Boss, E., and R. V. Zaneveld (2003), The effect of bottom substrate on inherent optical properties: Evidence of biogeochemical processes, *Liminol. Oceanogr.*, 48(1, part 2), 346 – 354.

Boucourt, W. C. (1981), Circulation in the Chesapeake Bay entrance region, in *Chesapeake Bay Plume Study - Superflux 1980*, edited by J. W. Campbell and J. P. Thomas, pp. 61-78, NASA Langley Research Center, Hampton, Virginia.

Bricaud, A., M. Babin, A. Morel, and H. Claustre (1995), Variability in the chlorophyll-specific absorption coefficients in natural phytoplankton: analysis and parameterization, *J. Geophys. Res.*, *100*(C7), 13321 – 13332.

Bricaud, A., A. Morel, M. Babin, K. Allali, and H. Claustre (1998), Variations of light absorption by suspended particles with chlorophyll a concentration in oceanic (case 1) waters: analysis and implications for bio-optical models, *J. Geophys. Res.*, *103*(C13), 31033 – 31044.

Bush, M. B. (2000), *Ecology of a changing planet* (2nd edition), Prentice Hall (Upper Saddle River, New Jersey).

Carder, K. L., R. G. Steward, G. R. Harvey, and P. B. Ortner (1989), Marine humic and fulvic acids: Their effect on remote sensing of ocean chlorophyll, *Limnol. Oceanogr.*, 34(1), 68 – 81.

Chang, G. C., and T. D. Dickey (2001), Optical and physical variability on timescales from minutes to the seasonal cycle on the New England shelf: July 1996 to June 1997, *J. Geophys. Res.*, *106*(C5), 9435 – 9453.

Chang, G. C., T. D. Dickey, O. M. Schofield, A. D. Weidemann, E. Boss, W. S. Pegau, M. A. Moline, and S. M. Glenn (2002), Nearshore physical processes and bio-optical properties in the New York Bight, *J. Geophys. Res., 107*(C9), 3133, doi: 10.1029/2001JC001018.

Chang, G. C., T. D. Dickey, C. D. Mobley, E. Boss, and W. S. Pegau (2003), Toward closure of upwelling radiance in coastal waters , *Appl. Opt.* **42**, 1574 – 1582.

DeGrandpre, M. D., A. Vodacek, R. K. Nelson, E. J. Bruce, and N. V. Blough (1996), Seasonal seawater optical properties of the U. S. Middle Atlantic Bight, *J. Geophys. Res., 101*(C10), 22727 – 22736.

Dierssen, H. M., R. C. Zimmerman, R. A. Leathers, T. V. Downes, and C. O. Davis (2003), Ocean color remote sensing of seagrass and bathymetry in the Bahamas Banks by high-resolution airborne imagery, *Limnol. Oceangr.* 48 (1, part 2), 444 – 455.

Duysens, L. N. M. (1956), The flattening of the absorption spectrum of suspensions as compared to that of solutions, *Biochim. Biophys. Acta*, 19, 1 – 12.

Garver, S. A., and D. A. Siegel (1997), Inherent optical property inversion of ocean color spectra and its biogeochemical interpretation: 1. Time series from the Sargasso Sea, *J. Geophys. Res., 102*(C8), 18607 – 18625.

Gordon, H. R. (1989), Can the Lamert-Beer law be applied to the diffuse attenuation coefficient of ocean water? *Limnol. Oceangr.* 34, 1389 – 1409.

Gordon, H. R. (1997), Atmospheric correction of ocean color imagery in the Earth Observing System era, *J. Geophys. Res., 102*(D14), 17081 – 17106.

Gordon, H. R. (1999), Contribution of Raman scattering to water-leaving radiance: a reexamination, *Appl. Opt.*, 38, 3166 – 3174.

Gordon, H. R. (2003), Pitfalls in atmospheric correction of ocean color imagery: how should aerosol optical properties be computed?: Comment, *Appl. Opt.*, 42, 542 – 544.

Gordon, H. R. (2005), Normalized water-leaving radiance: revisiting the influence of surface roughness, *Appl. Opt.*, 44, 241 – 248.

Gordon, H. R., O. B. Brown, R. H. Evans, J. W. Brown, R. C. Smith, K. S. Baker, and D. K. Clark (1988), A semianalytic radiance model of ocean color, *J. Geophys. Res., 93*(D9), 10909 – 10924.

Gordon, H. R., and A. Morel (1983), *Remote assessment of ocean color for interpretation of satellite visible imagery*, 114 pp., Springer-Verlag, New York.

Gordon, H. R., and M. Wang (1994a), Retrieval of water-leaving radiance and aerosol optical thickness over the oceans with SeaWiFS: a preliminary algorithm, *Appl. Opt.*, 33, 443 – 452.

Gordon, H. R., and M. Wang (1994b), Influence of oceanic whitecaps on atmospheric correction of ocean-color sensors, *Appl. Opt.*, 33, 7754 – 7763.

Gould R. W., R. A. Arnone, and P. M. Martinolich (1999), Spectral dependence of the scattering coefficient in case 1 and case 2 waters, *Appl. Opt., 38,* 2377 – 2383.

Gregg, W. W., and K. L. Carder (1990), A simple spectral solar irradiance model for cloudless marine atmospheres, *Limnol. Oceangr.* 35, 1657 – 1675.

Harding, L. W. (1994), Long-term trends in the distribution of phytoplankton in Chesapeake Bay: roles of light, nutrients and streamflow, *Mar. Ecol. Prog. Ser.* 104, 267 – 291.

Harding, L. W., A. Magnuson, M. E. Mallonee (2005), SeaWiFS retrievals of chlorophyll in Chesapeake Bay and the mid-Atlantic bight, *Estuar. Coast. Shelf Sci.,* 62, 75 – 94.

Harrison, A. W., and C. A. Coombes (1988), An opaque cloud cover model of sky short wavelength radiance, *Solar Energy*, 41(4), 387 – 392.

Hoge, F. E. (2006), Beam attenuation coefficient retrieval by inversion of airborne lidar-induced chromophoric dissolved organic matter fluorescence: I. Theory, *Appl. Opt.* 45, 2344 – 2351.

Hoge, F. E., C. W. Wright, P. E. Lyon, R. N. Swift, and J. K. Yungel (1999), Satellite retrieval of the absorption coefficient of phytoplankton phycoerythrin pigment: theory and feasibility status, *Appl. Opt.* 38, 7431 – 7441.

IOCCG (1999), Status and plans for satellite ocean-colour missions: considerations for complementary missions, in *Reports of the International Ocean-Color Coordinating Group*, no. 2, edited by J. Yoder, 43 pp., Dartmouth, Nova Scotia.

IOCCG (2000), Remote sensing of ocean color in coastal, and optically-complex waters, in *Reports of the International Ocean-Color Coordinating Group*, no. 3, edited by S. Sathyendranath, 140 pp., Dartmouth, Nova Scotia.

Johnson, D. R., A. Weidemann, R. Arnone, and C. O. Davis (2001), Chesapeake Bay outflow plume and coastal upwelling events: physical and optical properties, *J. Geophys. Res., 106*(C6), 11613 – 11622.

Kirk, J. T. O. (1991), Volume scattering function, average cosines, and the underwater light field, *Limnol. Oceangr.* 36, 455 – 467.

Kirk, J. T. O. (1994), *Light and phytosynthesis in aquatic ecosystems, 2nd ed.*, Cambridge University Press, New York.

Kishino, M., N. Takahashi, N. Okami, and S. Ichimura (1985), Estimation of the spectral absorption coefficient of phytoplankton in the sea, *Bull. Mar. Sci.*, 37, 634 – 642.

Kowalczuk, P. (1999), Seasonal variability of yellow substance absorption in the surface layer of the Baltic Sea, *J. Geophys. Res., 104*(C12), 30047 – 30058.

Lee, Z., K. Carder, C. Mobley, R. Steward, and J. Patch (1998), Hyperspectral remote sensing for shallow waters: 1. A semianalytical model, *Appl. Opt., 37*, 6329 – 6338.

Lee, Z., K. Carder, C. Mobley, R. Steward, and J. Patch (1999), Hyperspectral remote sensing for shallow waters: 2. Deriving bottom depths and water properties by optimization, *Appl. Opt., 38*, 3831 – 3843.

Lee, Z.-P., K.-P. Du, and R. Arnone (2005), A model for diffuse attenuation coefficient of downwelling irradiance, *J. Geophys. Res.* 110, C02016, doi: 10.1029/2004JC002275.

Liu, C.-C., K. L. Carder, R. L. Miller, and J. E. Ivey (2002), Fast and accurate model of underwater scalar irradiance, *Appl. Opt.* 41, 4962 – 4974.

Loisel, H., and A. Morel (1998), Light scattering and chlorophyll concentration in case 1 waters: a reexamination, *Limnol. Oceanogr., 43*(5): 847 – 858.

Magnuson, A., L. W. Harding, M. E. Mallonee, and J. E. Adolf (2004), Bio-optical model for Chesapeake Bay and the Middle Atlantic Bight, *Estuar. Coast. Shelf Sci.*, 61, 403 – 424.

Mann, K. H., and J. R. N. Lazier (1996), *Dynamics of marine ecosystems: biological-physical interactions in the ocean*, 2nd ed., 394 pp., Blackwell Science Inc., Malden, Massachusetts.

Marotorena, S., A. Morel, and B. Gentili (1994), Diffuse reflectance of oceanic shallow waters: influence of water depth and bottom albedo, *Limnol. Oceangr.* 39(7), 1689 – 1703.

Maritorena, S., D. A. Siegel, and A. R. Peterson (2002), Optimization of a semianalytical ocean color model for global-scale applications, *Appl. Opt., 41*, 2705 – 2714.

Marshall, H. G. (1981), Phytoplankton assemblages within the Chesapeake Bay plume and asjacent waters of the continental shelf, in *Chesapeake Bay Plume Study - Superflux 1980*, edited by J. W. Campbell and J. P. Thomas, pp. 439 – 468, NASA Langley Research Center, Hampton, Virginia.

Martin, S. (2004), *An introduction on ocean remote sensing*, 454 pp., Cambridge University Press, Cambridge, United Kingdom.

McCormick, N. J. (1995), Mathematical models for the mean cosine of irradiance and the diffuse attenuation coefficient, *Limnol. Oceangr.* 40, 1013 – 1018.

Mitchell, B. G., M. Kahru, J. Wieland, and M. Stramska (2002), Determination of spectral absorption coefficients of particles, dissolved material and phytoplankton for distrete water samples, in *Ocean optics protocols for satellite ocean color sensor validation, Revision 3*, Vol. 2, edited by J.L. Mueller and G.S. Fargion, pp. 231 – 257, NASA Goddard Space Flight Center, Greenbelt, Maryland.

Mobley, C. (1994), *Light and Water: Radiative Transfer in Natural Waters*, 592 pp., Academic Press, San Diego, California.

Mobley, C. D. (1999), Estimation of the remote-sensing reflectance from above-surface measurements, *Appl. Opt.* 36: 7442 – 7455.

Mobley, C. D., L. K. Sundman, and E. Boss (2002), Phase function effects on oceanic light fields, *Appl. Opt.* 41, 1035 – 1050.

Mobley, C. D., L. K. Sundman (2003), Effects of optically shallow bottoms on upwelling radiances: Inhomogeneous and sloping bottoms, *Limnol. Oceangr.* 48 (1, part 2), 329 – 336.

Mobley, C. D., H. Zhang, and K. J. Voss (2003), Effects of optically shallow bottoms on upwelling radiances: Bidirectional reflectance distribution function effects, *Limnol. Oceangr.* 48 (1, part 2), 337 – 345.

Mobley, C. D., L. K. Sundman, C. O. Davis, J. H. Bowles, T. V. Downes, R. A. Leathers, M. J. Montes, W. P. Bissett, D. D. R. Kohler, R. P. Reid, E. M. Louchard, and A. Gleason (2005), Interpretation of hyperspectral remote-sensing imagery by spectrum matching and look-up tables, *Appl. Opt.* 44, 3576 – 3592.

Morel, A., D. Antoine, and B. Gentili (2002), Bidirectional reflectance of oceanic waters accounting for Raman emission and varying particle scattering phase function, *Appl. Opt.* 41: 6289 – 6306.

Morel, A., and B. Gentili (1991), Diffuse reflectance of oceanic waters: its dependence on Sun angle as influenced by the molecular scattering contribution, *Appl. Opt.* 30, 4427 – 4438.

Morel, A., and S. Maritorena (2001), Bio-optical properties of oceanic waters: A reappraisal, *J. Geophys. Res., 106*(C4), 7163 – 7180.

Mueller, J.L. (2000), SeaWiFS algorithm for the diffuse attenuation coefficient, K(490), using water-leaving radiances at 490 and 555 nm, in O'Reilly, J.E. and co-authors: *SeaWiFS Postlaunch Calibration and Validation Analyses*, Part 3, edited by S. B. Hooker and E. R. Firestone, NASA/TM-2000-206892, Vol. 11, NASA Goddard Space Flight Center, Greenbelt, Maryland, 24 – 27.

Mueller, J. L., G. S. Fargion, and C. R. McClain (2002), Data requirements for ocean color algorithms and validation, in *Ocean optics protocols for satellite ocean color sensor validation, Revision 3*, Vol. 2, edited by J.L. Mueller and G.S. Fargion, pp. 231 – 257, NASA Goddard Space Flight Center, Greenbelt, Maryland.

O'Reilly, J. E., S. Maritorena, B. G. Mitchell, D. A. Siegel, K. L. Carder, S. A. Garver, M. Kahru, and C. McClain (1998), Ocean color algorithms for SeaWiFS, *J. Geophys. Res., 103*(C11), 24937 – 24953.

O'Reilly, J.E., and C. Zetlin (1998), Seasonal, horizontal, and vertical distribution of phytoplankton chlorophyll a in the northeast U.S. continental shelf ecosystem, *NOAA Technical Report NMFS 139*, 120 pp., U.S. Department of Commerce, Seattle, Washington.

O'Reilly, J. E., and 24 co-authors (2000), SeaWiFS postlaunch calibration and validation analyses, Part 3. *In* S. B. Hooker, and E. R. Firestone [eds.], SeaWiFS postlanch technical report series, Vol. 11. NASA Technical Memorandum 2000 – 206892.

Parsons, T. R., M. Takahashi, and B. Hargrave (1984), *Biological Oceanographic Processes, 3rd ed.*, 323 pp., Pergamon, New York.

Pegau, S., J. R. V. Zaneveld, and J. L. Mueller (2003), Volume absorption coefficients: instruments, characterization, field measurements and data analysis protocols, in *Ocean optics protocols for satellite ocean color sensor validation, Revision 4*, Vol. 4, edited by J.L. Mueller, G.S. Fargion, and C.R. McClain, pp. 27 – 38, NASA Goddard Space Flight Center, Greenbelt, Maryland.

Petzold, T. J. (1972), *Volume scattering functions for selected ocean waters* (Scripps Inst. Oceanogr.).

Pope, R. M., and E. S. Fry (1997), Absorption spectrum (380 – 700nm) of pure water, II, Integrating cavity measurements, *Appl. Opt., 36,* 8710 – 8723.

Prieur, L. and S. Sathyendranath (1981), An optical classification of coastal and oceanic waters based on the specific spectral absorption curves of phytoplankton pigmentes, dissolved organic matter, and other particulate materials, *Limnol. Oceanogr.* 26, 671 – 689.

Rennie, S. E., J. L. Largier and S. J. Lentz (1999), Observation of a pulsed buoyancy current downstream of Chesapeake Bay, *J. Geophys. Res., 104*(C8), 18227 – 18240.

Reynolds, R., D. Stramski, and G. Mitchell (2001), A chlorophyll-dependent semianalytical reflectance model derived from field measurements of absorption and backscattering coefficients within the Southern Ocean, *J. Geophys. Res., 106*(C4), 7125 – 7138.

Robinson, I. S. (2004), *Measuring the oceans from space: The principles and methods of satellite oceanography*, 669 pp., Springer.

Rochelle-Newall, E. J., and T. R. Fisher (2002), Production of chromophoric dissolved organic matter fluorescence in marine and estuarine environments: an investigation into the role of phytoplankton, *Mar. Chem.*, 77, 7 – 21.

Siegel, D. A., M. Wang, S. Maritonera, and W. Robinson (2000), Atmospheric correction of satellite ocean color imagery: the black pixel assumption, *Appl. Optics, 39*(21), 3582 – 3591.

Sletten, M. A., G. O. Marmorino, T. F. Donato, D. J. McLaughlin, and E. Twarog (1999), An airborne, real aperture radar study of the Chesapeake Bay outflow plume, *J. Geophys. Res.*, 104(C1), 1211 – 1222.

Smith, R.C., and K. Baker (1981), Optical properties of the clearest natural waters (200 – 800 nm), *Appl. Optics, 20*(2), 177-184.

Stramski, D., and C. D. Mobley (1997), Effect of microbial particles on oceanic optics, *Limnol. Oceanogr.*, 42, 538 – 549.

Su, W., T. P. Charlock, and K. Rutledge (2002), Observations of reflectance distribution around sunglint from a coastal ocean platform, *Appl. Opt.*, 41, 7369 – 7383.

Trees, C. C., D. K. Clark, R. R. Bidigare, M. E. Ondrusek, and J. L. Mueller (2000), Accessory pigments versus chlorophyll a concentration with the euphotic zone: A ubiquitous relationship, *Limnol. Oceanogr.* 45(5), 1190 – 1143.

Ulloa, O., S. Sathyendranath, and T. Platt (1994), Effect of the particle-size distribution on the backscattering ratio in seawater, *Appl. Opt.*, 33, 7070 – 7077.

Voss, K. J., C. D. Mobley, L. K. Sundman, J. E. Ivey, and C. H. Mazel (2003), The spectral upwelling radiance distribution in optically shallow waters, *Limnol. Oceanogr.* 48 (1, part 2), 364 – 373.

Wang, M. (1999), Atmospheric correction of ocean color sensor: computing atmospheric diffuse transmittance, *Appl. Opt.*, 38, 451 – 455.

Wang, M., and S. W. Bailey (2001), Correction of sun glint contamination on the SeaWiFS ocean and atmosphere products, *Appl. Opt.*, 40(27), 4790 – 4798.

Wang, M., B. A. Franz, R. A. Barnes, and C. R. McClain (2001), Effects of Spectral Bandpass on SeaWiFS-Retrieved Near-Surface Optical Properties of the Ocean, *Appl. Opt.* 40, 343 – 348.

Wang, M. (2006), Effects of ocean surface reflectance variation with solar elevation on normalized water-leaving radiance, *Appl. Opt.* 45, 4122 – 4128.

Werdell, P. J., and C. S. Roesler (2003), Remote assessment of benthic substrate composition in shallow waters using multispectral reflectance, *Limnol. Oceangr.* 48 (1, part 2), 557 – 567.

Wittlinger, S. (2002), *Hyperspectral Remote Sensing of Subtidal Macrophytes in Optically Shallow Water*, M. S. Thesis, Moss Landing Marine Laboratories/San Jose State University, Moss Landing, California.

Zaneveld, J. R. (1989), An asymptotic closure theory for irradiance in the sea and its inversion to obtain the inherent optical properties, *Limnol. Oceangr.* 34 1442 – 1452.

Zaneveld, J. R., and E. Boss (2003), The influence of bottom morphology on reflectance: Theory and two-dimensional geometry model, *Limnol. Oceangr.* 48 (1, part 2), 374 – 379.

Zaneveld, J. R., J. C. Kitchen, and C. Moore (1994), The scattering error correction of reflecting –tube absorption meters, *Ocean Optics XII, Proc. SPIE*, 2258, 44 – 55.

Zaneveld, J. R. V., S. Pegau, and J. L. Mueller (2003), Volume scattering function and backscattering coefficients: instruments, characterization, field measurements and data analysis protocols, in *Ocean optics protocols for satellite ocean color sensor validation, Revision 4*, Vol. 4, edited by J.L. Mueller, G.S. Fargion, and C. R. McClain, pp. 65-76, NASA Goddard Space Flight Center, Greenbelt, Maryland.

Zimmerman, R. C. (2003), A biooptical model of irradiance distribution and photosynthesis in seagrass canopies, *Limnol. Oceangr.* 48 (1, part 2), 568 – 585.

Zimmerman, R. C. (2006), Chapter 13: Light and photosynthesis in seagrass meadows, in *Seagrasses: biology, ecology, and conservation*, edited by A. Larkum, R. Orth, and C. Duarte, pp. 303 – 321, Springer.

VITA

Xiaoju Pan

Department of Ocean, Earth, and Atmospheric Sciences

Old Dominion University

4600 Elkhorn Avenue, Norfolk, VA 23529, USA.

Education

B. S., Biochemistry (1996), Xiamen University, Xiamen, Fujian, P. R. China

M. S., Biological Oceanography (2000), Institute of Oceanography, the Chinese Academy of Sciences, Qingdao, Shangdong, P. R. China

Ph. D., Biological Oceanography (2007), Old Dominion University, Norfolk, Virginia, USA.